Analysis of $+G_z$ Acceleration Induced Stresses in the Human Ventricle Myocardium

by

James Ernest Moore
M.Eng., Carleton University, 1985
B.Eng., Carleton University, 1983

A Dissertation Submitted in Partial Fulfillment of the
Requirements for the Degree of

DOCTOR OF PHILOSOPHY

in the Department of Mechanical Engineering

We accept this dissertation as conforming
to the required standard

Dr. J.B. Haddow, Supervisor (Mechanical Engineering)

Dr. J.W. Provan, Member (Mechanical Engineering)

Dr. G.W. Vickers, Member (Mechanical Engineering)

Dr. R. Illner, Outside Member (Mathematics)

Dr. R.W. Ogden, External Examiner (Mathematics)
University of Glasgow

Name

Dissertation Abstracts International is arranged by broad, general subject categories. Please select the one subject which most nearly describes the content of your dissertation. Enter the corresponding four digit code in the spaces provided.

SUBJECT TERM

SUBJECT CODE

U·M·I

Subject Categories

THE HUMANITIES AND SOCIAL SCIENCES

COMMUNICATIONS AND THE ARTS

Architecture	0729
Art History	0377
Cinema	0900
Dance	0378
Fine Arts	0357
Information Science	0723
Journalism	0391
Library Science	0399
Mass Communications	0708
Music	0413
Speech Communication	0459
Theater	0465

EDUCATION

General	0515
Administration	0514
Adult and Continuing	0516
Agricultural	0517
Art	0273
Bilingual and Multicultural	0282
Business	0688
Community College	0275
Curriculum and Instruction	0727
Early Childhood	0518
Elementary	0524
Finance	0277
Guidance and Counseling	0519
Health	0680
Higher	0745
History of	0520
Home Economics	0278
Industrial	0521
Language and Literature	0279
Mathematics	0280
Music	0522
Philosophy of	0998
Physical	0523

Psychology	0525
Reading	0535
Religious	0527
Sciences	0714
Secondary	0533
Social Sciences	0534
Sociology of	0340
Special	0529
Teacher Training	0530
Technology	0710
Tests and Measurements	0288
Vocational	0747

LANGUAGE, LITERATURE AND LINGUISTICS

Language	
General	0679
Ancient	0289
Linguistics	0290
Modern	0291
Literature	
General	0401
Classical	0294
Comparative	0295
Medieval	0297
Modern	0298
African	0316
American	0591
Asian	0305
Canadian (English)	0352
Canadian (French)	0355
English	0593
Germanic	0311
Latin American	0312
Middle Eastern	0315
Romance	0313
Slavic and East European	0314

PHILOSOPHY, RELIGION AND THEOLOGY

Philosophy	0422
Religion	
General	0318
Biblical Studies	0321
Clergy	0319
History of	0320
Philosophy of	0322
Theology	0469

SOCIAL SCIENCES

American Studies	0323
Anthropology	
Archaeology	0324
Cultural	0326
Physical	0327
Business Administration	
General	0310
Accounting	0272
Banking	0770
Management	0454
Marketing	0338
Canadian Studies	0385
Economics	
General	0501
Agricultural	0503
Commerce-Business	0505
Finance	0508
History	0509
Labor	0510
Theory	0511
Folklore	0358
Geography	0366
Gerontology	0351
History	
General	0578

Ancient	0579
Medieval	0581
Modern	0582
Black	0328
African	0331
Asia, Australia and Oceania	0332
Canadian	0334
European	0335
Latin American	0336
Middle Eastern	0333
United States	0337
History of Science	0585
Law	0398
Political Science	
General	0615
International Law and Relations	0616
Public Administration	0617
Recreation	0814
Social Work	0452
Sociology	
General	0626
Criminology and Penology	0627
Demography	0938
Ethnic and Racial Studies	0631
Individual and Family Studies	0628
Industrial and Labor Relations	0629
Public and Social Welfare	0630
Social Structure and Development	0700
Theory and Methods	0344
Transportation	0709
Urban and Regional Planning	0999
Women's Studies	0453

THE SCIENCES AND ENGINEERING

BIOLOGICAL SCIENCES

Agriculture	
General	0473
Agronomy	0285
Animal Culture and Nutrition	0475
Animal Pathology	0476
Food Science and Technology	0359
Forestry and Wildlife	0478
Plant Culture	0479
Plant Pathology	0480
Plant Physiology	0817
Range Management	0777
Wood Technology	0746
Biology	
General	0306
Anatomy	0287
Biostatistics	0308
Botany	0309
Cell	0379
Ecology	0329
Entomology	0353
Genetics	0369
Limnology	0793
Microbiology	0410
Molecular	0307
Neuroscience	0317
Oceanography	0416
Physiology	0433
Radiation	0821
Veterinary Science	0778
Zoology	0472
Biophysics	
General	0786
Medical	0760

EARTH SCIENCES

Biogeochemistry	0425
Geochemistry	0996

Geodesy	0370
Geology	0372
Geophysics	0373
Hydrology	0388
Mineralogy	0411
Paleobotany	0345
Paleoecology	0426
Paleontology	0418
Paleozoology	0985
Palynology	0427
Physical Geography	0368
Physical Oceanography	0415

HEALTH AND ENVIRONMENTAL SCIENCES

Environmental Sciences	0768
Health Sciences	
General	0566
Audiology	0300
Chemotherapy	0992
Dentistry	0567
Education	0350
Hospital Management	0769
Human Development	0758
Immunology	0982
Medicine and Surgery	0564
Mental Health	0347
Nursing	0569
Nutrition	0570
Obstetrics and Gynecology	0380
Occupational Health and Therapy	0354
Ophthalmology	0381
Pathology	0571
Pharmacology	0419
Pharmacy	0572
Physical Therapy	0382
Public Health	0573
Radiology	0574
Recreation	0575

Speech Pathology	0460
Toxicology	0383
Home Economics	0386

PHYSICAL SCIENCES

Pure Sciences

Chemistry	
General	0485
Agricultural	0749
Analytical	0486
Biochemistry	0487
Inorganic	0488
Nuclear	0738
Organic	0490
Pharmaceutical	0491
Physical	0494
Polymer	0495
Radiation	0754
Mathematics	0405
Physics	
General	0605
Acoustics	0986
Astronomy and Astrophysics	0606
Atmospheric Science	0608
Atomic	0748
Electronics and Electricity	0607
Elementary Particles and High Energy	0798
Fluid and Plasma	0759
Molecular	0609
Nuclear	0610
Optics	0752
Radiation	0756
Solid State	0611
Statistics	0463

Applied Sciences

Applied Mechanics	0346
Computer Science	0984

Engineering	
General	0537
Aerospace	0538
Agricultural	0539
Automotive	0540
Biomedical	0541
Chemical	0542
Civil	0543
Electronics and Electrical	0544
Heat and Thermodynamics	0348
Hydraulic	0545
Industrial	0546
Marine	0547
Materials Science	0794
Mechanical	0548
Metallurgy	0743
Mining	0551
Nuclear	0552
Packaging	0549
Petroleum	0765
Sanitary and Municipal	0554
System Science	0790
Geotechnology	0428
Operations Research	0796
Plastics Technology	0795
Textile Technology	0994

PSYCHOLOGY

General	0621
Behavioral	0384
Clinical	0622
Developmental	0620
Experimental	0623
Industrial	0624
Personality	0625
Physiological	0989
Psychobiology	0349
Psychometrics	0632
Social	0451

Abstract

It is well known that physiological problems occur when pilots are subjected to moderate-to-high $+G_z$ accelerations. The goal of this research is to develop a quantitative model that provides additional insight into the adverse effects of $+G_z$ accelerations on a pilot's cardiovascular system. The method of investigation is in contrast to previous studies, which have mainly relied on experimental techniques.

This work focuses on the development of a three-dimensional finite element model to analyse $+G_z$ induced stresses in the human left and right ventricles. The computational model is based on non-linear continuum theory, where the effects of finite deformation, irregular shape of the heart, and (nearly) incompressible behaviour of myocardium tissue are taken into account. The finite element formulation is developed using the Galerkin weighted residual method with a *penalty* treatment of the incompressibility condition. In this study, an exponential type strain energy function is used to model the cardiac tissue.

This technique provides a new perspective for the mechanical study of $+G_z$ acceleration on the human heart. Results presented demonstrate the ability of the finite element model to provide quantitative data on the effects of gravitational loading on the cardiovascular system. The analysis predicts gross distortion and stress data for the human heart under sustained exposure to inertia loading up to $+5\ G_z$.

Examiners:

Dr. J.B. Haddow, Supervisor (Mechanical Engineering)

Dr. J.W. Provan, Member (Mechanical Engineering)

Dr. G.W. Vickers, Member (Mechanical Engineering)

Dr. R. Illner, Outside Member (Mathematics)

Dr. R.W. Ogden, External Examiner (Mathematics)
University of Glasgow

Acknowledgements

I would like to express my sincere gratitude to my supervisor, Professor J.B. Haddow, for his valuable guidance and assistance in this endeavour.

I also wish to acknowledge Mr. W. Fraser for suggesting the research topic and Mr. Minh Ly for his assistance and technical support.

This research was partially funded by Dr. B. Tabarrok in conjunction with the Defence and Civil Institute for Environmental Medicine (DCIEM) under Grant No. W7711-9-7077/01.

Contents

List of Figures

Chapter 1

Introduction

The ongoing development of high performance aircraft capable of providing substantial positive accelerations ($+G_z$) has created the need for a better understanding of the physiological responses that can affect a pilot's judgment. The term $+G_z$ (positive G) commonly used to denote inertia forces that act along the vertical axis of an upright body. Effectively, these forces cause the heart and other body parts to displace downwards, inducing an elevated stress state.

Experimental investigation has been the principal method used to study the physiological changes associated with a pilot's exposure to moderate to high $+G_z$ accelerations. These experiments are designed in part to simulate in flight acceleration conditions that can occur during aerial combat manoeuvres or emergency situations. From experiments conducted in a *safe* environment using a centrifuge, the average blackout level observed for an *unprotected* individual is between 3.5 to 4.0 G_z . When fitted with an anti-G suit and using straining manoeuvres (muscle tensing with controlled breathing) a pilot can often attain +9 G_z for a short duration [5, 10, 11]. In future, with improved prevention of pathological effects due to $+G_z$ acceleration

and increased performance of newer fighter aircraft, combat manoeuvring in excess of +9 G_z may be attainable without G - OC (loss of consciousness) [7, 59, 97].

Physiological responses to $+G_z$ acceleration range from the less severe temporary loss of peripheral vision to unconsciousness and, in very severe cases, possible damage to heart tissue. For safety reasons, there is particular interest in the effects of $+G_z$ inertia forces on the cardiovascular system (see [6, 17, 55]). Consequently, elevated stress levels in the vascular due to high $+G_z$ loading have attracted the attention of researchers (eg. [54, 55, 87]).

In such research, high $+G_z$ loading has been associated with abnormalities of the electrocardiogram in man [54], as well as sub endocardial haemorrhage and pathological changes of the myocardial tissue in animals [55]. Though most researchers have assumed that ischemia is the cause of tissue damage in animals subject to high $+G_z$ loading conditions [87], detailed pathological examination of swine has indicated tearing of the heart fibres rather than damage consistent with a hypoxic or ischemic insult. It is probable that the observed damage is due to the high stresses and strains resulting from a combination of i) high $+G_z$ loading acting directly on the heart fibres, ii) elevated hydrostatic pressures in the vasculature, and iii) stresses from normal contraction of the heart.

Naturally, these reports of endocardial haemorrhaging and myo fibrillar degradation in swine undergoing high sustained $+G_z$ accelerations raise questions regarding the possibility of cardiac tissue damage in humans subjected to similar $+G_z$ forces. Non-invasive cardiological techniques used during experiments on humans seem too insensitive to provide sufficient data to determine the presence of any localized cardiac damage. Consequently, there is

need for a computational model to predict stress levels in the human heart under high $+G_z$ accelerations. In this study, such a model capable of providing additional insight into the effects of $+G_z$ induced stresses on the human heart is developed. The computational model is based on the finite element method where the effects of finite deformation for an incompressible elastic material are accounted for.

The study details the development of a finite element model to determine the stress/strain state of the human left ventricle (LV) and right ventricle (RV) myocardium during sustained $+G_z$ acceleration. Whereas in previous studies, finite element models of the heart have considered only the passive diastole and active systole cyclic responses of the left ventricle in a normal ($+1\ G_z$) environment (eg. [8, 22, 23, 25, 28, 30, 31, 45, 48, 64, 65, 67, 98, 169]). The flexibility of the finite element method to deal with complicated shapes and account for the effects of material and geometrical non-linearities makes it an ideal technique to study the stress/strain behaviour of the heart. In addition, with the advent of computer-aided tomography and data imaging, an accurate geometric reconstruction of the heart is possible [4, 15, 76].

The heart wall is composed of continuous intertwining myocardial fibres following a helical path through the wall thickness [88]. The arrangement of the myocardial fibres, which form spiraling bands of muscle resulting in an intricate webbed structure across the ventricle wall, is depicted in Figure 1.1. These complex fibre bundles form the left and right ventricles. In essence, the heart wall behaves as a non-linear anisotropic composite material [63]. In the literature some data on the properties of heart tissue is available [56, 69, 72]. In addition, there exists a number of promising constitutive relationships, relating stress to strain, for passive myocardium (see [14, 35, 42, 43, 44,

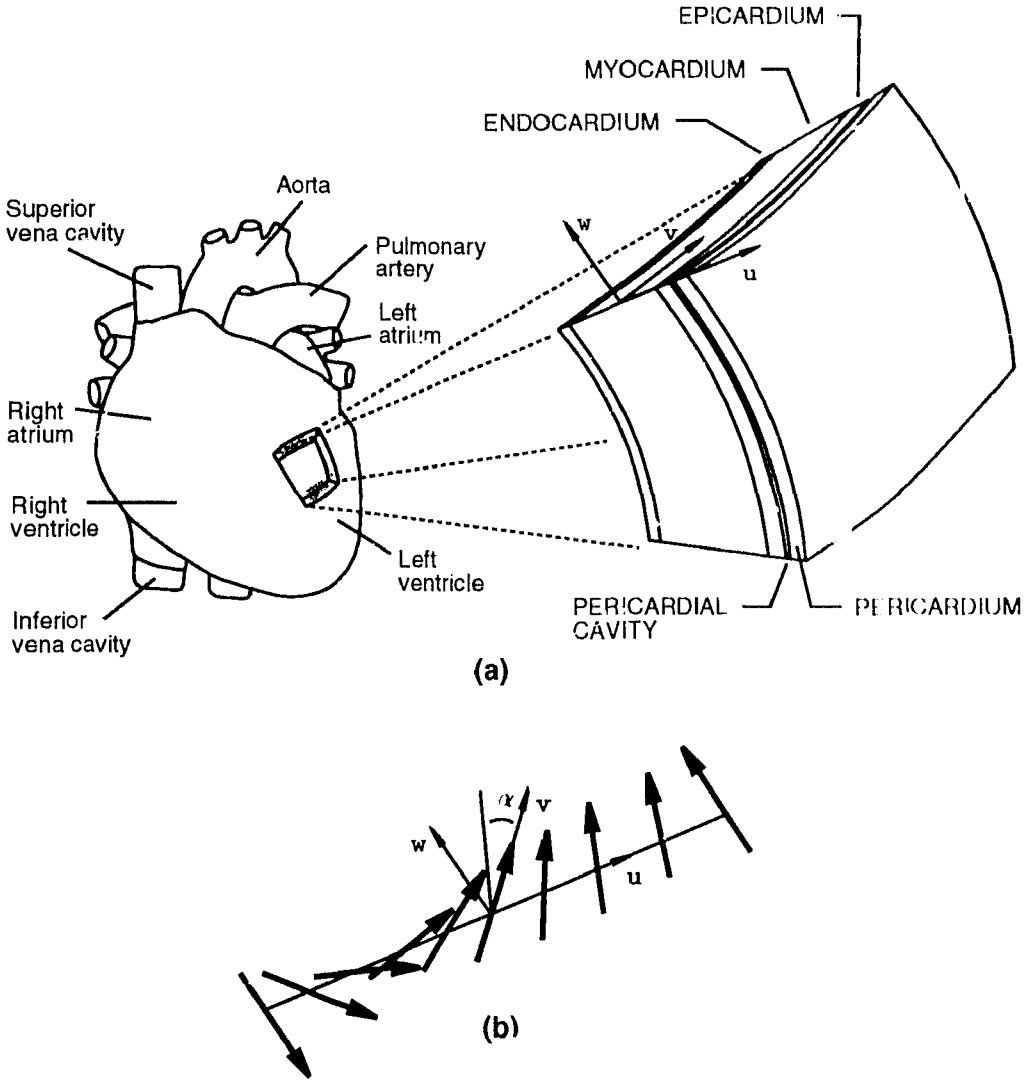

Figure 1.1: A Schematic drawing depicting an excised through thickness section of the human ventricle: (a) Showing the distribution of the endocardium, myocardium, and epicardium of the ventricle wall with supporting pericardial sac. (b) The arrangement of the myocardial fibre bundles, where the angle of orientation, α, gives the smooth transition of the fibre direction and is measured counterclockwise from v in the local axis system (u, v, w).

56, 62]). These relationships are based on a *pseudo-strain* energy function, which represents a *best fit* for experimentally collected material data. It is, therefore, both feasible and desirable to incorporate such a constitutive relation into the finite element model. Further, to ensure a realistic model for the analysis of $+G_z$ induced stresses in the human ventricle myocardium, consideration of the structural interaction of the surrounding anatomy is desirable. Since under severe $+G_z$ loading conditions the ventricles undergo significant deformations, it is expected that load transfer occurs between the heart and supporting pericardial membrane [95].

In Chapter 2, the theoretical foundation on which a computational model for the determination of the stress and strain state in the ventricle myocardium during sustained $+G_z$ acceleration is presented. The model utilizes the finite element technique (Chapter 3) where the effects of finite deformation, non-linear material behaviour, and the irregular shape of the heart are accounted for. Emphasis is placed on the incorporation of a realistic constitutive relation into the finite element formulation. A further description of the geometric reconstruction and modelling considerations of the human heart is given in Chapter 4.

In this work, a special purpose computer program is developed *in house* for the non-linear analysis of the human ventricles subjected to $+G_z$ inertia forces. This approach lends itself to an easier process of model refinement as improved analysis techniques are developed and new material/physiological data becomes available. A discussion of the non-linear finite element software package developed for the analysis of sustained $+G_z$ induced stress in the human LV and RV myocardium is given in Chapter 5. The finite element software package is designed and implemented using **C**, a *structured*

programming language [19]. Also, the convergence characteristics and predictive capabilities of the model are discussed, and computational verification of the software is assessed numerically using a series of *test* problems. These problems contain both linear and non-linear geometric (finite displacements / rotations) and material (incompressible) effects. Comparison of numerically generated results with closed form solutions and/or experimental data of other researchers is included when available. In addition, an interactive three-dimensional (3D) graphical modeller written in C using PHIGS graphic library routines [89] is also discussed in Chapter 5. The graphical modeller with colour capabilities is considered imperative for the visualization of the 3D heart model during construction and, most importantly, for the post processing of the vast quantity of stress and displacement data in a pictorial format.

In the future, it should also be possible to compare numerically generated geometric responses with those measured experimentally using ultra sound imaging techniques in a centrifuge [11]. However, when experiments cannot be justified due to safety considerations, the computational model can provide valuable quantitative (gross distortion and predicted stress) data on the effects of $+G_z$ induced stresses in humans (see Chapter 6).

Though the task of performing a realistic simulation of the cardiac response under sustained $+G_z$ acceleration is an enormously difficult one, progress over the past two decades in both computer and medical technology has reached the stage where a sufficiently accurate computational model of the heart can now be developed. The computational model developed can be used to facilitate the collection and analysis of experimental data, possibly aid in the design of new experiments, and provide useful information

unattainable experimentally. While many questions remain unanswered, the progress indicated will hopefully provide the stimulus for future numerical studies.

Chapter 2

Theoretical Formulation and Development

2.1 Introduction

The non-linear geometric and material behaviour of the human heart deforming under sustained $+G_z$ acceleration requires careful study from both a theoretical and computational standpoint. In this chapter, theoretical aspects of the problem are presented which subsequently provide the foundation for the finite element computational model. Further, a statement of the linearized *weak* or variational form of the governing *balance of momentum* equations is presented. In addition, the rate form of these equations are given for comparison purposes with their linear counterpart. Furthermore, special attention is given to the incorporation of a realistic incompressible hyperelastic constitutive relation into the cardiac material model.

In order to develop an effective solution procedure to solve this complex problem, many state-of-the-art computational techniques are employed. From a theoretical standpoint, it is essential that the following issues are incorporated in the computational model:

(i). It is necessary that any systematic linearization of the *weak* or variational form of the *balance of momentum* equations agrees with the corresponding rate form.

(ii). The use of an *objective* measure of stress-rate and deformation to ensure that certain physical quantities are independent of the choice of *observer* [34, 61].

(iii). A valid method for stress integration of rate equations (ie. incremental updating of stresses) that maintains *incremental* objectivity in the presence of finite stretches and rotations [41, 68].

(iv). Incorporation of a realistic incremental hyperelastic constitutive relation to model the incompressible behaviour of passive myocardium and pericardium.

(v). The ability to handle *non-conservative* or deformation dependent loading. In particular, the blood-volume in the left and right ventricle chambers of the heart exerts a hydrostatic surface pressure on the ventricle endocardium, which is a non-conservative external force.

2.2 Kinematics of Deformation

Consider a simple deformable body, **B**, occupying a region $\mathcal{B}$ in Euclidean space $\mathcal{E}$, where $\mathcal{B} \subset \mathcal{E}$ with a *body particle* given by $X \in \mathbf{B}$. The body is initially unstressed in the natural configuration at time $t = 0$, and is denoted by $\mathcal{B}^o$. Let $\mathcal{B}^r$ represent the referential configuration with $\mathbf{X}$ denoting the position vector of the particle X. After the body undergoes a deformation, it occupies the current configuration denoted by $\mathcal{B}^t$, where the particle X now has a spatial position vector $\mathbf{x}$. One may note that the referential configuration may or may not correspond to the natural configuration of the body at $t = 0$ (see Figure 2.1).

Mathematically, the deformation process can be represented by the one-to-one and onto (invertible) mapping $\boldsymbol{\chi}$: $\mathcal{B}^r \longrightarrow \mathcal{B}^t$, such that

$$\mathbf{x} = \boldsymbol{\chi}(\mathbf{X}, t). \tag{2.1}$$

Assuming the same origin for $\mathbf{X}$ and $\mathbf{x}$, the motion of a particle can be written as

$$\mathbf{x} = \boldsymbol{\chi}(\mathbf{X}, t) = \mathbf{I}\mathbf{X} + \mathbf{u}(\mathbf{X}, t), \tag{2.2}$$

where $\mathbf{u}$ is the vector displacement of the particle and the identity tensor, $\mathbf{I}$, is used to denote a two-point *shifter* relating vectors in two rectangular coordinate systems [18]. Alternatively, in component form

$$x_i = \chi_i(\mathbf{X}, t) = \delta_{i\alpha} X_\alpha + u_i(\mathbf{X}, t), \tag{2.3}$$

where $i, \alpha \in \{1, 2, 3\}$ and $\delta_{i\alpha}$ is the Kronecker delta. The lower case Latin and Greek character indices are used for the Cartesian coordinate system components in the spatial and referential configurations, respectively.

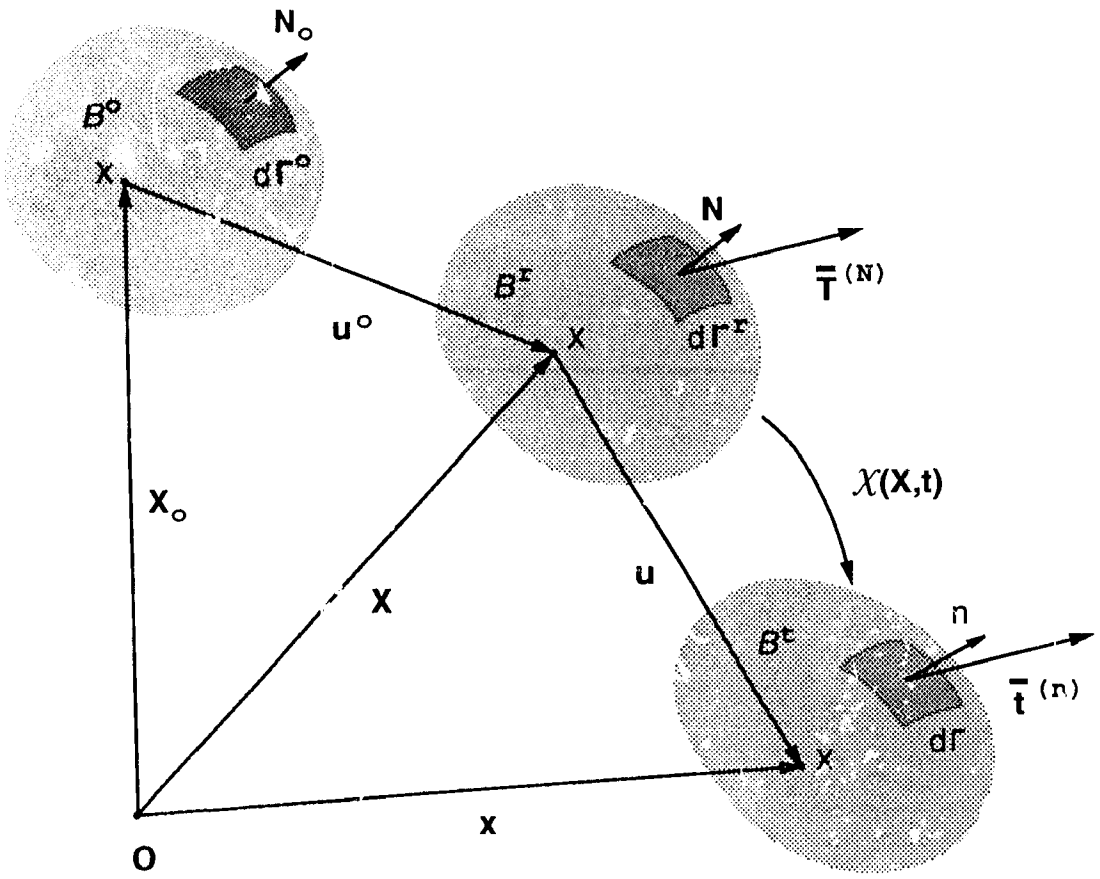

Figure 2.1: A sketch depicting the natural $\mathcal{B}^o$, referential $\mathcal{B}^r$, and spatial $\mathcal{B}^t$ configurations of a body undergoing a deformation. Also, elemental surfaces $d\Gamma^r$ and $d\Gamma$ with surface tractions $\bar{\mathbf{T}}^{(N)} = \mathbf{T}^T\mathbf{N}$ and $\bar{\mathbf{t}}^{(n)} = \sigma^T\mathbf{n}$ are shown in the referential and spatial configurations, respectively. The origin $\mathbf{O}$ is used to define the global frame of reference.

The *deformation gradient* of the body, $\mathcal{B}$, is a second order (two point) tensor given by

$$\mathbf{F} = \nabla_X \otimes \boldsymbol{\chi}, \quad \text{or} \quad F_{i\alpha} = \frac{\partial \chi_i}{\partial X_\alpha} (\boldsymbol{e}_i \otimes \boldsymbol{E}_\alpha), \tag{2.4}$$

where ∇_X denotes the gradient operator with respect to the reference configuration and $\boldsymbol{e}_i$, $\boldsymbol{E}_\alpha$ are base vectors in the spatial and referential configurations, respectively. In addition, the *displacement gradient*, denoted by $\mathbf{D}$, is given by

$$\mathbf{D} = \nabla_X \otimes \mathbf{u} = \mathbf{F} - \mathbf{I}, \tag{2.5}$$

where $\mathbf{I}$ is the unit tensor.

In the analysis, the soft cardiac tissue is modelled as an incompressible solid capable of finite deformation. For an isochoric deformation process the total rate of change (or material derivative) of density is subject to the constraint

$$\frac{D\rho(\mathbf{x}, t)}{Dt} = 0. \tag{2.6}$$

Noting that $\mathbf{F}$ is non-singular, a volume element in the deformed spatial configuration, $d\Omega$, is given by

$$d\Omega = \det \mathbf{F} \, d\Omega^r, \tag{2.7}$$

where $d\Omega^r$ is the element in the reference configuration. Also, from mass conservation

$$\rho^r = \det \mathbf{F} \, \rho, \tag{2.8}$$

where ρ is the density in the spatial configuration, and

$$J \equiv \det \mathbf{F} > 0 \quad \forall \ t \in [0, \infty). \tag{2.9}$$

(The superscript r is used to denote the referential configuration.) For the isochoric behaviour of the soft biological tissue,

$$\det \mathbf{F} = 1. \tag{2.10}$$

In addition, it is convenient to define the velocity, $\mathbf{v}$, and velocity gradient, $\mathbf{L}$, of a particle as

$$\mathbf{v}(\mathbf{x},t) = \frac{\partial \boldsymbol{\chi}}{\partial t}(\mathbf{X},t) = \dot{\boldsymbol{\chi}}(\mathbf{X},t), \qquad \text{and} \qquad \mathbf{L} = \nabla_x \otimes \mathbf{v}, \tag{2.11}$$

where ∇_x denotes the gradient operator with respect to the current configuration. Further, the velocity gradient can be decomposed into a symmetrical and anti-symmetric part, respectively as

$$\mathbf{L} = \boldsymbol{d} + \boldsymbol{\omega}. \tag{2.12}$$

In particular, the symmetric part corresponds to the spatial *rate of deformation* tensor

$$\boldsymbol{d} = \frac{1}{2}(\mathbf{L} + \mathbf{L}^T), \tag{2.13}$$

and the anti symmetric part is the spatial *spin* tensor

$$\boldsymbol{\omega} = \frac{1}{2}(\mathbf{L} - \mathbf{L}^T), \tag{2.14}$$

where superscript T denotes transpose. Also, a useful relation for the time-rate of the deformation gradient, $\dot{\mathbf{F}}$, is given by

$$\dot{\mathbf{F}} = \mathbf{L}\,\mathbf{F}. \tag{2.15}$$

In order to develop a finite element methodology for the problem considered, either a Lagrangian (material / referential) or Eulerian (spatial /

current) approach is adopted. The case where all variables are referred to the unstressed natural configuration at $t = 0$, say $\mathcal{B}^0$, is termed the *Total Lagrangian* method. In this work, the reference configuration is chosen to move with the change of geometry of the body, $\mathcal{B}^t$, and corresponds to the most recently known configuration. This approach has been termed the *Updated Lagrangian* method. Both of these approaches can be shown to be mathematically equivalent; however, either may possess some computational advantages over the other depending on the problem under consideration.

2.3 Strain Measures

The deformation gradient, being invertible, possesses a polar decomposition, which is unique and defined by

$$\mathbf{F} = \mathbf{V}\mathbf{R} = \mathbf{R}\mathbf{U}, \tag{2.16}$$

where $\mathbf{R}$ is a proper orthogonal tensor, and $\mathbf{V}$ ($\mathbf{U}$) are the symmetric positive definite *left* (*right*) *stretch* measures. Alternatively, in component form

$$\mathbf{F} = F_{i\alpha}\boldsymbol{e}_i \otimes \boldsymbol{E}_\alpha = V_{ij}R_{j\alpha}\boldsymbol{e}_i \otimes \boldsymbol{E}_\alpha = R_{i\beta}U_{\beta\alpha}\boldsymbol{e}_i \otimes \boldsymbol{E}_\alpha.$$

It is also useful to represent some common deformation tensors in terms of the deformation gradient, that is, the *left* (*right*) *Cauchy Green* deformation measures $\mathbf{A}$ ($\mathbf{C}$) defined by

$$\mathbf{A} = \mathbf{V}^2 = \mathbf{F}\mathbf{F}^T, \quad \text{and} \quad \mathbf{C} = \mathbf{U}^2 \quad \mathbf{F}^T\mathbf{F}. \tag{2.17}$$

Associated with these tensors are the principal invariants, I_i, for $i \in \{1,2,3\}$.

$$I_1 = tr\,\mathbf{A} = tr\,\mathbf{C},$$

$$I_2 = \frac{1}{2}[(tr\ \mathbf{A})^2 - tr\ \mathbf{A}^2] = \frac{1}{2}[(tr\ \mathbf{C})^2 - tr\ \mathbf{C}^2], \tag{2.18}$$
$$I_3 = \det \mathbf{A} = \det \mathbf{C}, \qquad (Incompressibility : I_3 = 1)$$

where tr denotes the trace.

One can express (Lagrangian) *Green's strain*, $\mathbf{E}$, in terms of the right Cauchy Green deformation measure as

$$\mathbf{E} = \frac{1}{2}(\mathbf{C} - \mathbf{I}). \tag{2.19}$$

Alternatively, the (Eulerian) *Almansi's strain* tensor, $\boldsymbol{\epsilon}$, expressed in terms of the inverse left Cauchy Green deformation measure is defined by

$$\boldsymbol{\epsilon} = \frac{1}{2}(\mathbf{I} - \mathbf{A}^{-1}). \tag{2.20}$$

From equations (2.19) and (2.20) the relationship between the Lagrangian and Eulerian strain tensors is given, respectively, by

$$\mathbf{E} = \mathbf{F}^T \boldsymbol{\epsilon}\, \mathbf{F}, \quad \text{and} \quad \boldsymbol{\epsilon} = \mathbf{F}^{-T} \mathbf{E}\, \mathbf{F}^{-1}. \tag{2.21}$$

2.4 Balance Laws

2.4.1 Conservation of Mass

From the conservation of mass flow

$$\frac{D}{Dt} \int_{\mathcal{B}^t} \rho(\mathbf{x}, t) d\Omega = 0. \tag{2.22}$$

Applying the Reynold's transport theorem and the divergence theorem to equation (2.22) yields

$$\int_{\mathcal{B}^t} \left[\frac{\partial \rho}{\partial t} + \operatorname{div}(\rho \mathbf{v}) \right] d\Omega = 0, \tag{2.23}$$

and since the domain $\mathcal{B}^t$ is arbitrary, the integrand must be zero everywhere. This integrand is often referred to as the continuity equation, and can be rewritten as

$$\frac{\partial \rho}{\partial t} + \mathbf{v}\cdot\nabla_x \rho + \rho\nabla_x\cdot\mathbf{v} = 0, \tag{2.24}$$

or in terms of the material derivative of the density, $D\rho(\mathbf{x},t)/Dt$, as

$$\frac{D\rho}{Dt} + \rho\nabla_x\cdot\mathbf{v} = 0. \tag{2.25}$$

For an incompressible material, as is the case with soft cardiac tissue, equation (2.6) implies that the divergence of the velocity field is zero, ie.

$$\operatorname{div}\mathbf{v} = \nabla_x\cdot\mathbf{v} = 0, \tag{2.26}$$

which effectively becomes the continuity condition for an incompressible material.

2.4.2 Conservation of Momentum

Spatial Form

The balance equation for the linear momentum of a body is equated to the vector sum of the external forces acting on that body

$$\frac{D}{Dt}\int_{\mathcal{B}^t} \rho\mathbf{v}\,d\Omega = \int_{\mathcal{B}} \rho\frac{D\mathbf{v}}{Dt}d\Omega = \int_{\mathcal{B}^t} \rho\mathbf{b}\,d\Omega + \int_{\partial\mathcal{B}_T^t} \mathbf{t}^{(\mathbf{n})}d\Gamma, \tag{2.27}$$

where $\mathbf{b}(\mathbf{x},t)$ is the body force per unit mass, and $\mathbf{t}^{(\mathbf{n})}(\mathbf{x},t)$ is the surface traction on part of the boundary, denoted by $\partial\mathcal{B}_T^t$, such that

$$\boldsymbol{\sigma}^T\mathbf{n} = \mathbf{t}^{(n)}(\mathbf{x},t) \qquad \text{for} \quad \mathbf{x}\in\partial\mathcal{B}_T^t. \tag{2.28}$$

where $\boldsymbol{\sigma}$ is the Cauchy (true) stress tensor. The position, $\mathbf{x}$, can be prescribed on the part of the boundary, denoted by $\partial\mathcal{B}_u^t$, as

$$\mathbf{x} = \mathbf{x} \qquad \text{for} \quad \mathbf{x} \in \partial\mathcal{B}_u^t, \tag{2.29}$$

with the following initial conditions

$$\mathbf{u}(\mathbf{X},0) = \mathbf{u}^0(\mathbf{X}), \quad \text{and} \quad \mathbf{v}(\mathbf{X},0) = \mathbf{v}^0(\mathbf{X}). \tag{2.30}$$

Furthermore,

$$\partial\mathcal{B}_u^t \cup \partial\mathcal{B}_t^t = \partial\mathcal{B}^t, \qquad \text{and} \qquad \partial\mathcal{B}_u^t \cap \partial\mathcal{B}_t^t = \emptyset.$$

By introducing Reynold's transport theorem and applying the divergence theorem to the linear momentum equation, equation (2.27) becomes

$$\int_{\mathcal{B}^t} \left[\rho \frac{D\mathbf{v}}{Dt} - \rho\mathbf{b} - \operatorname{div}\boldsymbol{\sigma} \right] d\omega = 0, \tag{2.31}$$

where $\operatorname{div}\boldsymbol{\sigma} = tr\{\nabla_x \boldsymbol{\sigma}\} = \nabla_x \cdot \boldsymbol{\sigma}$. Noting that the integral must vanish for an arbitrary region of $\mathcal{B}^t$ and, replacing $D\mathbf{v}/Dt$ by $\dot{\mathbf{v}}$, the *Eulerian equation of motion* can be written

$$\operatorname{div}\boldsymbol{\sigma} + \rho\mathbf{b} = \rho\dot{\mathbf{v}}, \qquad \frac{\partial\sigma_{ji}}{\partial x_j} + \rho b_i = \rho\dot{v}_i. \tag{2.32}$$

For the special case of a body at rest or undergoing uniform translational motion, equation (2.32) is referred to as the *equilibrium equation* with the right hand side being zero.

Furthermore, from the law of conservation of angular momentum, the Cauchy stress tensor is symmetric in the absence of body moments, $\boldsymbol{\sigma}^T = \boldsymbol{\sigma}$.

Material Form

Using equation (2.7) and noting the kinematic relationship between a current and reference elemental surfaces

$$\mathbf{n}da = J(\mathbf{F}^{-T})\mathbf{N}dA, \tag{2.33}$$

the material form of the linear momentum equation can be written as

$$\frac{\partial}{\partial t}\int_{\mathcal{B}} \rho^r(\mathbf{X})\dot{\boldsymbol{\chi}}(\mathbf{X},t)d\Omega^r = \int_{\mathcal{B}} \rho^r(\mathbf{X})\mathbf{b}(\mathbf{X},t)d\Omega^r + \int_{\partial\mathcal{B}_t} \mathbf{T}^{(\mathbf{N})}(\mathbf{X},t)dA, \tag{2.34}$$

where $\mathbf{T}$ denotes the (non-symmetric) nominal stress tensor (and its transpose is the *first Piola–Kirchhoff* stress tensor) as

$$\mathbf{T} = J\boldsymbol{\sigma}\mathbf{F}^{-1}. \tag{2.35}$$

Applying the divergence theorem to equation (2.34) and proceeding in a similar fashion to the derivation of the spatial linear momentum equations one obtains the *Lagrangian equation of motion*

$$\mathrm{Div}\,\mathbf{T} + \rho^r\mathbf{b} = \rho^r\dot{\mathbf{V}}, \qquad \frac{\partial T_{ji}}{\partial X_j} + \rho^r b_i = \rho^r \dot{V}_i \tag{2.36}$$

where $\dot{\mathbf{V}}(\mathbf{X},t) = \ddot{\boldsymbol{\chi}}(\mathbf{X},t)$ and Div (with uppercase D) denotes the divergence operator with respect to $\mathbf{X}$ and it is assumed that $\mathbf{b}$ does not depend on the deformation. The boundary conditions in the reference frame are given by

$$\begin{aligned} \mathbf{X} &= \mathbf{X} \qquad \text{for} \quad \mathbf{X} \in \partial\mathcal{B}_u^r, \\ \mathbf{T}^T\mathbf{N} &= \mathbf{T}^{(\mathbf{N})} \qquad \text{for} \quad \mathbf{X} \in \partial\mathcal{B}_t^r. \end{aligned}$$

Alternatively, the material form of the balance equations can be obtained using the appropriate transformations from the spatial to material reference frame.

The *second* (symmetric) *Piola Kirchhoff* stress tensor $\mathbf{S}$ is given by

$$\mathbf{S} = \mathbf{T}(\mathbf{F}^{-1})^T \quad \text{or} \quad \mathbf{T} = \mathbf{S}\mathbf{F}^T, \tag{2.37}$$

and is conjugate to Green's strain rate tensor (ie., the stress power per unit volume in the reference configuration is given by $tr\{\mathbf{S}\dot{\mathbf{E}}\}$). This stress measure does not have a direct physical interpretation, but, its importance will become evident when formulating a finite element methodology. Further, one may note that the second Piola Kirchhoff stress is related to the Cauchy stress tensor by

$$\boldsymbol{\sigma} = J^{-1}\,\mathbf{F}\mathbf{S}\mathbf{F}^T \quad \text{or} \quad \mathbf{S} = J\,\mathbf{F}^{-1}\boldsymbol{\sigma}(\mathbf{F}^{-1})^T. \tag{2.38}$$

2.5 Variational (Weak) Form of Linear Momentum Balance

Consider the *strong* form of the boundary-value problem of momentum balance (where $\boldsymbol{\sigma}^T = \boldsymbol{\sigma}$)

$$\begin{aligned} \operatorname{div}\boldsymbol{\sigma} + \rho\mathbf{b} &= \rho\dot{\mathbf{v}} && \text{in } \mathcal{B}^t, \\ \boldsymbol{\sigma}^T\mathbf{n} &= \mathbf{t}^{(n)} && \text{on } \partial\mathcal{B}^t_T, \\ \mathbf{x} &= \mathbf{x} && \text{on } \partial\mathcal{B}^t_u. \end{aligned}$$

From calculus of variations, an equivalent *weak* or variational form of the boundary value problem of momentum balance can be constructed from

$$\int_{\mathcal{B}^t} (\operatorname{div}\boldsymbol{\sigma} + \rho\mathbf{b} - \rho\dot{\mathbf{v}})\cdot\delta\boldsymbol{\chi}\, d\Omega = 0, \tag{2.39}$$

where $\delta\boldsymbol{\chi}$ is an arbitrary kinematically admissible displacement field. Applying the divergence theorem to equation (2.39), the weak form of the variational equation is given by

$$\mathcal{G}(\mathbf{x}, \delta\boldsymbol{\chi}) = 0, \tag{2.40}$$

where $\mathcal{G}(\mathbf{x}, \delta\boldsymbol{\chi})$ is defined as

$$\int_{\mathcal{B}^t} tr\{\boldsymbol{\sigma}\,(\nabla_x \cdot \delta\boldsymbol{\chi})\}d\Omega + \int_{\mathcal{B}^t} \rho\,(\dot{\mathbf{v}} - \mathbf{b})\cdot\delta\boldsymbol{\chi}\,d\Omega \quad \int_{\partial\mathcal{B}^t_t} \mathbf{t}^{(n)}\cdot\delta\boldsymbol{\chi}\,dA$$

for all

$$\mathcal{U} = \left\{\mathbf{x} \mid \mathbf{x} \in C^0(\mathcal{B}^t),\ \ \mathbf{x} = \mathbf{x} \ \text{ on } \ \partial\mathcal{B}^t_u\right\},$$

and

$$\mathcal{V} = \left\{\delta\boldsymbol{\chi} \mid \delta\boldsymbol{\chi} \in C^0(\mathcal{B}^t),\ \ \delta\boldsymbol{\chi} = 0 \ \text{ on } \ \partial\mathcal{B}^t_u\right\}.$$

The set of *trial* solutions, denoted by $\mathcal{U}$, are kinematically admissible functions of $\boldsymbol{\chi}(\mathbf{X}, t)$ that satisfy the essential boundary conditions. In addition, the set of *variations*, denoted by $\mathcal{V}$, are the homogeneous counterpart of the trial functions.

For the special case where the $\mathcal{V}$ is taken as a *virtual displacement* field, $\delta\mathbf{u}$, ($\delta\mathbf{u} = \delta\boldsymbol{\chi}$) over $\partial\mathcal{B}^t$ and using the property that $\boldsymbol{\sigma}$ is symmetric, one obtains the virtual strain energy balance for a hyperelastic solid as

$$\underbrace{\int_{\mathcal{B}^t} tr\{\boldsymbol{\sigma}\,\delta\boldsymbol{\epsilon}\}d\Omega}_{\delta\text{V. strain energy}} = \underbrace{\int_{\mathcal{B}^t} \rho\,(\mathbf{b} - \dot{\mathbf{v}})\cdot\delta\mathbf{u}\,d\Omega}_{\text{V.W. body and inertial forces}} + \underbrace{\int_{\partial\mathcal{B}^t_t} \mathbf{t}^{(n)}\cdot\delta\mathbf{u}\,dA}_{\text{V.W. surface tractions}} \tag{2.11}$$

where $\delta\boldsymbol{\epsilon}$ is the *virtual strain* tensor [1] and is defined as the symmetric part of the virtual displacement gradient

$$\delta\boldsymbol{\epsilon} = \frac{1}{2}\left[(\nabla_x \cdot \delta\mathbf{u}) + (\nabla_x \cdot \delta\mathbf{u})^T\right]. \tag{2.12}$$

For completeness of the weak form of the boundary value problem an appropriate constitutive relation between $\boldsymbol{\sigma}$ and $\delta\boldsymbol{\epsilon}$ needs to be provided. This is discussed in the following section.

[1] The tensor $\delta\boldsymbol{\epsilon}$ should not be confused with the linear infinitesimal strain tensor, $\delta\boldsymbol{\epsilon}$ is the variational strain tensor conjugate to the Cauchy stress.

2.6 Consistent Linearization of the Balance of Momentum

In order to solve the strong form of the governing boundary-value problem, a linear approximation to an equivalent weak form is sought. The linear approximation which provides a basis for the finite element technique is discussed in some detail in this section. This approach is equivalent to the superimposing of incremental displacements on a finitely deformed body [26]. The term *consistent* is used to indicate that the systematic linearization of the weak form of the variational equations is consistent with the corresponding rate form [40]. Consistent linearization allows for the *optimal* incremental linear approximation to the set of non-linear equations within a small neighbourhood of some known reference state. The incremental (linearized) equations are only a first order approximation, whereas the corresponding rate equations are exact in form. Before commencing linearization of the governing equations, the following terminology is introduced to assist in defining the deformation process.

Consider the original undeformed body occupying $\mathcal{B}^0$ at time $t = 0$, undergoing a deformation and now occupying the reference configuration denoted by $\mathcal{B}^r$. Next, consider a superimposed deformation from the $\mathcal{B}^r$ configuration such that the body occupies the spatial configuration, $\mathcal{B}^t$. Referring to Figure 2.1, the body motion can be expressed as

$$\mathbf{x} = \boldsymbol{\chi}(\mathbf{X}, t) = \mathbf{I}\mathbf{X}(\mathbf{X}_o, t) + \mathbf{u}(\mathbf{X}, t), \tag{2.43}$$

where $\mathbf{u}$ is a superimposed motion from the referential configuration.

To linearize the weak form of the boundary-value problem (2.40), it is

more convenient to work with the material rather than the spatial form of these equations. For the reference configuration the integral domain is independent of body motion, which somewhat simplifies the linearization process. Further, it is assumed that $\mathbf{b}$ and $\mathbf{T}^{(N)}$ are independent of the kinematics. Then, equation (2.40) can be expressed in material form as

$$\mathcal{G}(\boldsymbol{\chi}, \delta\boldsymbol{\chi}) = \int_{\mathcal{B}^r} tr\{\mathbf{T}\,\delta\mathbf{F}\}d\Omega^r + \int_{\mathcal{B}^r} \rho^r\,(\dot{\mathbf{V}} - \mathbf{b})\cdot\delta\boldsymbol{\chi}\,d\Omega^r - \int_{\partial\mathcal{B}^r_T} \mathbf{T}^{(N)}\cdot\delta\boldsymbol{\chi}\,d\Gamma^r = 0, \tag{2.44}$$

where $\delta\mathbf{F} = \nabla_X \otimes \delta\boldsymbol{\chi}$. In order to find a solution to equation (2.44) it is desirable to obtain a local approximation to $\mathcal{G}$ about some reference point, $\hat{X}$. (Henceforth, $\hat{X}$ is replaced by $\hat{\mathbf{X}}$.) One such local approximation is obtained using a *consistent* approach to linearization of the balance of momentum equation [40], and is based on Taylor's Formula (see Appendix A).

A local linear approximation can be obtained by applying a linear operator L (as defined in equation (A.3)) to a tensor field, say $\mathbf{f}$, as follows

$$L[\mathbf{f}, \mathbf{a}]_{\hat{x}} = \mathbf{f}(\hat{x}) + (\nabla_x \mathbf{f}(\hat{x}))\cdot\mathbf{a} = \mathbf{f}(\hat{x}) + G_{\mathbf{a}}[\mathbf{f}(\hat{x})], \tag{2.45}$$

where $G_{\mathbf{a}} \equiv \mathbf{a}\cdot\nabla_x$ defines the *scalar* differential operator for any arbitrary vector $\mathbf{a}$ in Euclidean vector space.

Applying the linear operator L to the weak form of the momentum balance equations $\mathcal{G}(\boldsymbol{\chi}, \delta\boldsymbol{\chi}) = 0$, about some fixed point $\hat{\mathbf{X}} \in \mathcal{B}^r$ yields

$$\begin{aligned} L[\mathcal{G}, \mathbf{u}]_{\hat{\mathbf{X}}} &= \mathcal{G}(\hat{\mathbf{X}}) + (\nabla_X \otimes \mathcal{G}(\hat{\mathbf{X}}))\mathbf{u} \\ &= \mathcal{G}(\hat{\mathbf{X}}) + G_{\mathbf{u}}[\mathcal{G}(\hat{\mathbf{X}})] \\ &= 0. \end{aligned} \tag{2.46}$$

(Henceforth, the superscript $(\hat{\ })$ is omitted.) Now, considering the gradient of $\mathcal{G}(\mathbf{X})$ in the direction $\mathbf{u}$, as defined in equation (A.2), one may write

$$\begin{aligned} G_{\mathbf{X}}[\mathcal{G}(\mathbf{X})] &= \int_{\mathcal{B}^r} G_{\mathbf{X}}[tr\{\mathbf{T}\,\delta\mathbf{F}\}]d\Omega^r + \int_{\mathcal{B}^r} \rho^r G_{\mathbf{X}}[(\dot{\mathbf{V}}-\mathbf{b})]\cdot\delta\boldsymbol{\chi}\,d\Omega^r \\ &\quad - \int_{\partial\mathcal{B}^r_T} G_{\mathbf{X}}[\mathbf{T}^{(N)}]\cdot\delta\boldsymbol{\chi}\,d\Gamma^r, \end{aligned} \tag{2.47}$$

where $\delta\boldsymbol{\chi}$ is an arbitrary kinematically admissible displacement field. Assuming that $\mathbf{b}$ and $\mathbf{T}^{(N)}$ are independent of the deformation, then equation (2.47) reduces to

$$G_{\mathbf{X}}[\mathcal{G}(\mathbf{X})] = \int_{\mathcal{B}^r} tr\{G_{\mathbf{X}}[\mathbf{T}]\,\delta\mathbf{F}\}d\Omega^r + \int_{\mathcal{B}^r} \rho^r\,\ddot{\mathbf{u}}\cdot\delta\boldsymbol{\chi}\,d\Omega^r, \tag{2.48}$$

where $G_{\mathbf{X}}[\dot{\mathbf{V}}] = \ddot{\mathbf{u}}$ from equation (A.2). By substituting the corresponding expressions for $\mathcal{G}(\hat{\mathbf{X}})$ and $G_{\mathbf{X}}[\mathcal{G}(\hat{\mathbf{X}})]$ into (2.46), a local linear approximation to the weak form of the momentum balance equation about some fixed point $\hat{\mathbf{X}}$ is obtained as

$$\begin{aligned} &\int_{\mathcal{B}^r} tr\{G_{\mathbf{X}}[\mathbf{T}]\,\delta\mathbf{F}\}d\Omega^r + \int_{\mathcal{B}^r} \rho^r\,\ddot{\mathbf{u}}\cdot\delta\boldsymbol{\chi}\,d\Omega^r = \\ &\int_{\mathcal{B}^r} tr\{\mathbf{T}\,\delta\mathbf{F}\}d\Omega^r - \int_{\mathcal{B}^r} \rho^r(\dot{\mathbf{V}}-\mathbf{b})\cdot\delta\boldsymbol{\chi}\,d\Omega^r + \int_{\partial\mathcal{B}^r_T} \mathbf{T}^{(N)}\cdot\delta\boldsymbol{\chi}\,d\Gamma^r. \end{aligned} \tag{2.49}$$

Alternatively, the spatial form of (2.49) can be written using the transformation equations (2.7), (2.8), (2.33), and (2.38) as follows

$$\begin{aligned} &\int_{\mathcal{B}^t} J^{-1} tr\{G_{\mathbf{x}}[\mathbf{T}]\,\delta\mathbf{F}\}d\omega + \int_{\mathcal{B}^t} \rho\,\ddot{\mathbf{u}}\cdot\delta\boldsymbol{\chi}\,d\omega = \\ &\int_{\mathcal{B}^t} J^{-1} tr\{\mathbf{T}\,\delta\mathbf{F}\}d\omega - \int_{\mathcal{B}^t} \rho(\dot{\mathbf{v}}-\mathbf{b})\cdot\delta\boldsymbol{\chi}\,d\omega + \int_{\partial\mathcal{B}^t_T} \mathbf{t}^{(n)}\cdot\delta\boldsymbol{\chi}\,d\Gamma. \end{aligned} \tag{2.50}$$

Ultimately, the term $tr\{G_{\mathbf{x}}[\mathbf{T}]\,\delta\mathbf{F}\}$ defined for the referential configuration will require an equivalent spatial form for computational implementation, which is obtained by substitution of the constitutive relation. In this study, a hyperelastic constitutive relation capable of modelling the (nearly) incompressible behaviour of soft myocardial tissue is used.

2.7 A Constitutive Relationship for Cardiac Tissue

In this study, the cardiac tissue is assumed to behave as an incompressible hyperelastic solid [2]. Even though cardiac tissue exhibits anisotropic and viscoelastic behaviour, successful predictions of material response have been reported by researchers when idealizing the cardiac tissue as homogeneous and isotropic [3] [13, 23]. The assumptions of material homogeneity and isotropy are adopted in this thesis. In addition, the tissue is considered to undergo only isothermal deformation processes and to be chemically inert.

For a hyperelastic material there exists a potential energy function, denoted by W, which is taken as the stored energy per unit reference volume for isothermal deformation. Henceforth, W can be expressed as

$$W = \hat{W}(\mathbf{F}). \tag{2.51}$$

In this section, it is implied that the reference state corresponds to the original undeformed configuration where stress and strain vanish. Further, invariance under rigid body motion (ie. objectivity [61]) requires the strain energy function to obey

$$W = \hat{W}(\mathbf{Q}\,\mathbf{F}), \tag{2.52}$$

for all proper orthogonal tensors $\mathbf{Q}$. In particular, if $\mathbf{Q}$ is chosen to be $\mathbf{R}^T$ and using (2.16) one obtains

$$\hat{W}(\mathbf{F}) = \hat{W}(\mathbf{U}). \tag{2.53}$$

[2] A material is described as *Hyperelastic* if a stored energy function exists for isothermal or adiabatic deformation.

[3] A constitutive relation $\mathcal{L}(\mathbf{C})$ is defined as *isotropic* if and only if the property of $\mathcal{L}(\mathbf{Q}\,\mathbf{C}\,\mathbf{Q}^T) = \mathcal{L}(\mathbf{C})$ holds, where $\mathbf{Q}$ is a proper orthogonal tensor.

Since there exists a one-to-one correspondence between the tensors **U** and **C** (ie. $\mathbf{C} = \mathbf{U}^2$), equation (2.53) can be rewritten as

$$W = \hat{W}(\mathbf{C}). \tag{2.54}$$

More conveniently, for an isotropic material (2.54) can be expressed as

$$W = W(I_1, I_2, I_3), \tag{2.55}$$

where (I_1, I_2, I_3) are the principal invariants of **C**, as defined previously.

For a *Green elastic* or hyperelastic material the (nominal) stress - deformation relation is given by

$$\mathbf{T} = \frac{\partial \hat{W}(\mathbf{F})}{\partial \mathbf{F}}, \qquad T_{i\alpha} = \frac{\partial \hat{W}}{\partial F_{i\alpha}}, \tag{2.56}$$

and from equations (2.16) and (2.53) this becomes, for an isotropic material

$$\mathbf{T} = \frac{\partial \hat{W}(\mathbf{U})}{\partial \mathbf{U}} \mathbf{R}^T. \tag{2.57}$$

Using (2.17) and (2.37) the above can be expressed in terms of the second Piola Kirchhoff stress and right Cauchy Green deformation tensors as

$$\mathbf{S} = 2\frac{\partial \hat{W}(\mathbf{C})}{\partial \mathbf{C}}. \tag{2.58}$$

An alternative expression in terms of the invariants of **C** can be obtained by using of the chain rule for differentiation and noting the identities

$$\frac{\partial I_1}{\partial \mathbf{C}} = \mathbf{I}, \qquad \frac{\partial I_2}{\partial \mathbf{C}} = I_1\mathbf{I} - \mathbf{C}, \qquad \text{and} \qquad \frac{\partial I_3}{\partial \mathbf{C}} = I_3\mathbf{C}^{-1}.$$

Therefore,

$$\mathbf{S} = 2\left[-\frac{\partial W}{\partial I_2}\,\mathbf{C} + \left(\frac{\partial W}{\partial I_1} + I_1\frac{\partial W}{\partial I_2}\right)\,\mathbf{I} + I_3\frac{\partial W}{\partial I_3}\,\mathbf{C}^{-1}\right]. \tag{2.59}$$

If the reference configuration coincides with the natural configuration (ie. $\mathbf{C} = \mathbf{I}$), for which the stress vanishes, then

$$\mathbf{S}\Big|_{\mathbf{C}=\mathbf{I}} = \left[\frac{\partial W}{\partial I_1} + 2\frac{\partial W}{\partial I_2} + \frac{\partial W}{\partial I_3}\right]\Bigg|_{\mathbf{C}=\mathbf{I}} = 0. \tag{2.60}$$

In the special case of soft biological materials, such as cardiac tissue, the incompressibility constraint given in equation (2.18) is imposed. This constraint inhibits any stress measure from being solely determined from the deformation. In fact, the deformation determines the Cauchy stress only to some additive hydrostatic value. By introducing an arbitrary Lagrangian multiplier $-\frac{1}{2}p$ and rewriting W in the form

$$W = \hat{W}(\mathbf{C}) - \tfrac{1}{2}\, p\, (\det \mathbf{C} - 1), \tag{2.61}$$

an alternative form of equation (2.51) results. Therefore, for an incompressible material, equation (2.58) becomes

$$\mathbf{S} = 2\frac{\partial \hat{W}(\mathbf{C})}{\partial \mathbf{C}} - p\mathbf{C}^{-1}, \tag{2.62}$$

or in terms of the invariants of $\mathbf{C}$,

$$\mathbf{S} = 2\left[-\frac{\partial W}{\partial I_2}\,\mathbf{C} + \left(\frac{\partial W}{\partial I_1} + I_1\frac{\partial W}{\partial I_2}\right)\,\mathbf{I}\right] - p\mathbf{C}^{-1}. \tag{2.63}$$

Due to the lack of a reliable constitutive relationship to model the anisotropic poro-viscoelastic material behaviour of the human heart, a simpler approach is taken where the cardiac tissue is considered to be a non linear homogeneous isotropic elastic material. In this work, an exponential strain energy function proposed for soft biological materials [21] and subsequently used to model cardiac tissue [14, 99] of the form

$$\hat{W}(I_1) = a[e^{b(I_1-3)} - 1]. \tag{2.64}$$

is used, where a and b are material constants derived from experimental data. The constants a and b represent the *best fit* parameters for passive cardiac tissue data obtained experimentally. Incorporating equation (2.64) into (2.63) yields

$$\mathbf{S} = 2ab\, e^{b(I_1-3)}\, \mathbf{I} - p\mathbf{C}^{-1}. \tag{2.65}$$

For equation (2.60) at $t = 0$ to hold true when the strain energy function is given by equation (2.64), one obtains

$$p\,|_{t=0} = p_0 = 2ab. \tag{2.66}$$

The stress deformation relation given in equation (2.65) gives rise to a *mixed* finite element formulation, that is, both displacement and pressure (u, p) are taken as independent unknowns [37]. However, the elimination of p from the system of equations can be accomplished by relaxing the incompressibility constraint, $I_3 = 1$, using a penalty function. In the penalty formulation of the incompressible problem the constraint given by (2.26) is relaxed using

$$\nabla_x \cdot \mathbf{v} + \frac{\dot{p}}{\lambda} = 0, \tag{2.67}$$

where λ is a penalty parameter. Assuming the pressure to be a function of the dilatation, the solution of (2.67) can be expressed in terms of the invariant I_3 as

$$p = p_o - \frac{\lambda}{2} ln(I_3). \tag{2.68}$$

Effectively, the problem becomes one of modelling a nearly incompressible material, where the property of incompressibility is recovered as λ tends

to infinity. This approach allows the number of system equations to be drastically reduced while maintaining (near) incompressibility. In addition, due to the finite digital accuracy of computation, the magnitude of λ is restricted so that the problem is not ill conditioned [37].

2.8 Stress and Strain Rates

Relationships in terms of stress and strain rates should be independent of an observer transform given by $(\mathbf{x}, t) \longrightarrow (\mathbf{x}^*, t^*)$ with

$$\mathbf{x}^* = \mathbf{c}(t) + \mathbf{Q}(t)\mathbf{x}, \qquad t^* = t - a, \tag{2.69}$$

where $\mathbf{c}$ is a translation and $\mathbf{Q}$ is a proper orthogonal tensor.

The term *objective* is used to describe a tensor which is independent of an observer transform as defined in Ref. [61]. One such frame invariant rate used for the constitutive law in the reference configuration is the rate of the second Piola Kirchhoff stress and Green's strain rate tensors. For equation (2.58) the rate form is simply expressed as

$$\dot{\mathbf{S}} = 2\frac{\partial^2 W}{\partial \mathbf{C}^2} : \dot{\mathbf{C}}, \qquad \dot{S}_{\alpha\beta} = 2\frac{\partial^2 W}{\partial C_{\gamma\delta}\partial C_{\varepsilon\eta}}\dot{C}_{\varepsilon\eta}, \tag{2.70}$$

where the symbol : is used to denote the inner product of a fourth and second order tensor. Alternatively, the rate form of $\mathbf{S}$ given in terms of Green's strain tensor $\mathbf{E}$ for an incompressible material governed by equation (2.62) becomes

$$\dot{\mathbf{S}} = \frac{\partial^2 W(\mathbf{E})}{\partial \mathbf{E}\partial \mathbf{E}} : \dot{\mathbf{E}} - p(\dot{\mathbf{C}^{-1}}) - \dot{p}\mathbf{C}^{-1}. \tag{2.71}$$

However, for the finite element implementation one may consider a more useful form of (2.71), in terms of Green's strain rate, that is

$$\dot{\mathbf{S}} = \mathcal{C} : \dot{\mathbf{E}}, \tag{2.72}$$

where $\mathcal{C}$ is a fourth order material response tensor in the reference configuration. Also, Green's strain rate is related to the rate of deformation tensor by

$$\dot{\mathbf{E}} = \frac{1}{2}\dot{\mathbf{C}} = \mathbf{F}^T \boldsymbol{d} \mathbf{F}. \tag{2.73}$$

An alternative form of (2.71) can be written in component form as

$$\dot{S}_{\alpha\beta} = \left[\frac{\partial^2 W(\mathbf{E})}{\partial E_{\alpha\beta} \partial E_{\gamma\delta}} + p(C^{-1}_{\gamma\alpha} C^{-1}_{\delta\beta} + C^{-1}_{\alpha\delta} C^{-1}_{\beta\gamma}) + \lambda C^{-1}_{\alpha\beta} C^{-1}_{\gamma\delta} \right] \dot{E}_{\gamma\delta}, \tag{2.74}$$

where the term inside the square brackets is equivalent to $\mathcal{C}$ in equation (2.72). Further, the incompressibility constraint (2.26) must also hold from mass conservation.

For the finite element formulation the spatial form of the rate equation (2.72) is required. Adopting the Truesdell stress rate which is a suitable objective stress rate [91], the corresponding rate-type constitutive equation is given by

$$\overset{\circ}{\boldsymbol{\sigma}}^{<T>} = \mathcal{L} : \boldsymbol{d}, \tag{2.75}$$

where $\mathcal{L}$ is the fourth order instantaneous material response tensor, and $\boldsymbol{d}$ is the (spatial) deformation rate tensor defined in equation (2.13). In addition, $\overset{\circ}{\boldsymbol{\sigma}}^{<T>}$ can be related to the rate of change of the second Piola Kirchhoff stress tensor by

$$\overset{\circ}{\boldsymbol{\sigma}}^{<T>} = J^{-1} \mathbf{F} \dot{\mathbf{S}} \mathbf{F}^T. \tag{2.76}$$

Now, taking the time derivative of equation (2.38) and substituting into equation (2.76) for $\dot{\mathbf{S}}$ yields

$$\overset{\circ}{\boldsymbol{\sigma}}^{<T>} = \dot{\boldsymbol{\sigma}} - \mathbf{L}\boldsymbol{\sigma} - \boldsymbol{\sigma}\mathbf{L}^T + \boldsymbol{\sigma} tr\{\boldsymbol{d}\}, \tag{2.77}$$

where $\mathbf{L}$ is the velocity gradient as defined in equation (2.11). Also, the trace of $\boldsymbol{d}$, which is the *dilatational* part of the rate of deformation, is zero for an incompressible material. Substituting (2.77) into (2.75) and decomposing the velocity gradient in terms of the deformation rate and spin tensors yields

$$\dot{\boldsymbol{\sigma}} = \mathcal{L} : \boldsymbol{d} + (\boldsymbol{d} + \boldsymbol{\omega})\boldsymbol{\sigma} + \boldsymbol{\sigma}(\boldsymbol{d} - \boldsymbol{\omega}) - \boldsymbol{\sigma} tr\{\boldsymbol{d}\}. \tag{2.78}$$

Rearranging,

$$\dot{\boldsymbol{\sigma}} = (\mathcal{L} + \hat{\mathcal{L}}) : \boldsymbol{d} + \hat{\mathcal{S}} : \boldsymbol{\omega} \tag{2.79}$$

where $\hat{\mathcal{L}}$ and $\hat{\mathcal{S}}$ are fourth ordered stress dependent tensors defined in component notation as

$$\begin{aligned} \hat{\mathcal{L}}_{ijkl} &= -\sigma_{ij}\delta_{kl} + \frac{1}{2}(\sigma_{il}\delta_{jk} + \sigma_{jk}\delta_{il} + \sigma_{ik}\delta_{jl} + \sigma_{jl}\delta_{ik}) \\ \hat{\mathcal{S}}_{ijkl} &= \frac{1}{2}(\sigma_{il}\delta_{jk} + \sigma_{jl}\delta_{ik} - \sigma_{ik}\delta_{jl} - \sigma_{jk}\delta_{il}), \end{aligned}$$

and δ denotes the Kronecker delta. The first term, $(\mathcal{L} + \hat{\mathcal{L}})$, on the right hand side of equation (2.79) represents the material response due to deformation and typically depends on the deformation gradient, stress, and material parameters. The second term, $\hat{\mathcal{S}}$, which is uniquely specified by objectivity accounts for rotational effects.

Using equations (2.21), (2.74), and (2.75), the instantaneous material response tensor for the current configuration in component form becomes

$$\mathcal{L}_{ijkl} = J^{-1}\left[F^o_{i\alpha}F^o_{j\beta}F^o_{k\gamma}F^o_{l\delta}\frac{\partial^2 W(\mathbf{E}^o)}{\partial E^o_{\alpha\beta}\partial E^o_{\gamma\delta}} + p(\delta_{ki}\delta_{lj} + \delta_{li}\delta_{kj}) + \lambda\delta_{ij}\delta_{kl}\right], \tag{2.80}$$

where the symbol o is used to emphasize that the strain energy density function, W, is referred to the natural (undeformed) configuration. For completeness, the relationship between the instantaneous spatial and material

response tensors, defined in equations (2.75) and (2.72) respectively, can be stated in component form as

$$\mathcal{L}_{ijkl} = J^{-1} F_{ia} F_{jb} F_{kc} F_{ld} \mathcal{C}_{abcd}. \tag{2.81}$$

Now, applying the strain energy function for soft biological tissue, as given in (2.61) with $J = 1$, yields

$$\mathcal{L}_{ijkl} = 4ab^2 e^{b(E_{aa}^2)} F_{ia}^2 F_{ja}^2 F_{ka}^2 F_{la}^2 + p\,(\delta_{ki}\delta_{lj} + \delta_{il}\delta_{jk}) + \lambda \delta_{ij}\delta_{kl}. \tag{2.82}$$

Due to the symmetry of the energy conjugate pairs $(\mathbf{S}, \dot{\mathbf{E}})$ and $(\mathring{\boldsymbol{\sigma}}^{<I>}, \boldsymbol{d})$ the material and spatial response tensors, $\mathcal{C}$ and $\mathcal{L}$ respectively, both have minor symmetries

$$\mathcal{C}_{abcd} = \mathcal{C}_{bacd} = \mathcal{C}_{abdc} = \mathcal{C}_{badc},$$

$$\mathcal{L}_{ijkl} = \mathcal{L}_{jikl} = \mathcal{L}_{ijlk} = \mathcal{L}_{jilk}.$$

2.9 Incremental Constitutive Relation for Cardiac Tissue

In this section, the incremental form of the hyperelastic constitutive relation for soft cardiac tissue is derived. In particular, the objective is to provide a linearized expression for the term $tr\{\mathbf{T}\,\delta\mathbf{F}\}$ appearing in equation (2.44). However, this term expressed as the (symmetric) second Piola Kirchhoff stress tensor is desirable from a computational standpoint. Therefore, using equation (2.37) the incremental form of the virtual strain energy term in (2.49) becomes

$$\int_{\mathcal{B}^r} tr\{\mathrm{Grad}[\mathbf{T}]\,\delta\mathbf{F}\}\,d\Omega^r = \int_{\mathcal{B}^r} tr\left\{\mathrm{Grad}[\mathbf{S}\,\mathbf{F}^T]\,\delta\mathbf{F}\right\}d\Omega^r.$$

Since the scalar differential operator G_X is linear, the integrand can be re writ ten as

$$\begin{aligned} tr\left\{G_X[\mathbf{S}\,\mathbf{F}^T]\,\delta\mathbf{F}\right\} &= tr\left\{\left(G_X[\mathbf{S}]\,\mathbf{F}^T + \mathbf{S}\,G_X[\mathbf{F}^T]\right)\,\delta\mathbf{F}\right\} \\ &= tr\left\{(G_X[\mathbf{S}])\,\delta\mathbf{E}\right\} + tr\left\{(\mathbf{S}\,G_X[\mathbf{F}^T])\,\delta\mathbf{F}\right\}, \end{aligned} \tag{2.83}$$

using the symmetry property of $\mathbf{S}$. Also, the virtual strain tensor is given by

$$\delta\mathbf{E} = \frac{1}{2}\left(\mathbf{F}^T\,\delta\mathbf{F} + \delta\mathbf{F}^T\,\mathbf{F}\right), \tag{2.84}$$

and is correct to first order.

The terms for subsequent linearization in (2.83) are $G_X[\mathbf{F}^T]$ and $G_X[\mathbf{S}]$. The first term $G_X[\mathbf{F}^T]$ is given by

$$G_X[\mathbf{F}^T] = \frac{d}{d\epsilon}\left[\nabla_X(\dot{\mathbf{X}} + \epsilon\mathbf{u})\right]^T\Big|_{\epsilon=0} \qquad \mathbf{D}^T. \tag{2.85}$$

Next, the term $G_X[\mathbf{S}]$ is obtained by substitution of the constitutive relation given in equation (2.62) for an incompressible hyperelastic material. Therefore,

$$\begin{aligned} G_X[\mathbf{S}(\mathbf{C})] &= \frac{d}{d\epsilon}\left[\,2\partial\hat{W}(\mathbf{C})/\partial\mathbf{C} - p\,\mathbf{C}^{-1}\,\right]\Big|_{\epsilon=0} \\ &= 2\frac{d}{d\epsilon}\,\partial\hat{W}(\mathbf{C})/\partial\mathbf{C}\Big|_{\epsilon=0} - p\,\frac{d}{d\epsilon}\,\mathbf{C}^{-1}\Big|_{\epsilon=0} \quad \mathbf{C}^{-1}\,\frac{d}{d\epsilon}\,p\Big|_{\epsilon=0}. \end{aligned} \tag{2.86}$$

Utilizing the chain rule for differentiation, the first term on the right hand side of equation (2.86) becomes

$$2\frac{d}{d\epsilon}\,\frac{\partial\hat{W}(\mathbf{C})}{\partial\mathbf{C}}\Big|_{\epsilon=0} = 2\frac{\partial^2\hat{W}(\mathbf{C})}{\partial\mathbf{C}^2} : \left[\mathbf{D}^T\,\mathbf{F} + \mathbf{F}^T\,\mathbf{D}\right]. \tag{2.87}$$

From (2.17), the second term of (2.86) can be expressed as

$$p\,\frac{d}{d\epsilon}\,\mathbf{C}^{-1}\Big|_{\epsilon=0} = p\frac{d}{d\epsilon}\,(\mathbf{F}^T\mathbf{F})^{-1}\Big|_{\epsilon=0} = -p\,\mathbf{C}^{-1}\left[\mathbf{D}^T\,\mathbf{F} + \mathbf{F}^T\,\mathbf{D}\right]\,\mathbf{C}^{-1}. \tag{2.88}$$

Finally, by utilizing the logarithmic penalty function for $p(\mathbf{C})$ defined in equation (2.68), the third term of (2.86) becomes

$$\mathbf{C}^{-1}\frac{d}{d\epsilon}p\Big|_{\epsilon=0} = -\frac{\lambda}{2}\mathbf{C}^{-1}tr\left\{\left[\mathbf{D}^T\mathbf{F}+\mathbf{F}^T\mathbf{D}\right]\mathbf{C}^{-1}\right\}. \tag{2.89}$$

Now, combining equations (2.87), (2.88), and (2.89) an expression for the derivative of the second Piola–Kirchhoff stress is given by

$$\begin{aligned} &G_X[\mathbf{S}(\mathbf{E})] = \\ &\frac{\partial^2 W(\mathbf{E})}{\partial \mathbf{E}^2} : G_X[\mathbf{E}] + 2p\,\mathbf{C}^{-1}(G_X[\mathbf{E}])\,\mathbf{C}^{-1} + \lambda\mathbf{C}^{-1}tr\left\{(G_X[\mathbf{E}])\,\mathbf{C}^{-1}\right\}. \end{aligned} \tag{2.90}$$

where the derivative of the Lagrangian strain tensor, $G_X[\mathbf{E}]$, is

$$G_X[\mathbf{E}] = \frac{d}{d\epsilon}\,\mathbf{E}(\mathbf{C})\big|_{\epsilon=0} = \frac{1}{2}\left[\mathbf{D}^T\mathbf{F}+\mathbf{F}^T\mathbf{D}\right]. \tag{2.91}$$

In component form, the material form of the incremental second Piola–Kirchhoff stress tensor is

$$\triangle S_{\alpha\beta} = \left[\frac{\partial^2 W(\mathbf{E})}{\partial E_{\alpha\beta}\partial E_{\gamma\delta}} + p(C^{-1}_{\gamma\alpha}C^{-1}_{\delta\beta} + C^{-1}_{\alpha\delta}C^{-1}_{\beta\gamma}) + \lambda C^{-1}_{\alpha\beta}C^{-1}_{\gamma\delta}\right]\triangle E_{\gamma\delta}, \tag{2.92}$$

where

$$\triangle E_{\gamma\delta} = \frac{1}{2}\left[\frac{\partial(\triangle u)_i}{\partial X_\gamma}F_{i\delta} + F_{i\gamma}\frac{\partial(\triangle u)_i}{\partial X_\delta}\right] \tag{2.93}$$

and $\triangle u_i$ is an incremental displacement. Comparing the incremental material response tensor, $\mathcal{C}$, given in (2.92) with its corresponding rate-type form in (2.71), reveals that the terms inside the square brackets are identical.

For the special case when the Lagrangian and Eulerian configurations coincide, $\mathcal{B}^r = \mathcal{B}^t$, the deformation gradient reduces to the identity map ($\mathbf{F} = \mathbf{I}$). Therefore, the stress increment given by (2.93) transforms to the spatial incremental constitutive relation and is given in component form as

$$\triangle\sigma^{(r)}_{ij} = \left[F^o_{i\alpha}F^o_{j\beta}F^o_{k\gamma}F^o_{l\delta}\frac{\partial^2 W(\mathbf{E}^o)}{\partial E^o_{\alpha\beta}\partial E^o_{\gamma\delta}} + p(\delta_{ki}\delta_{lj}+\delta_{il}\delta_{jk}) + \lambda\delta_{ij}\delta_{kl}\right]\triangle\varepsilon_{ij}, \tag{2.94}$$

where equation (2.75) enables the strain increment to be written as

$$\Delta\boldsymbol{\varepsilon} = \frac{1}{2}\left[\frac{\partial(\Delta u)_i}{\partial x_j} + \frac{\partial(\Delta u)_j}{\partial x_i}\right]. \tag{2.95}$$

(The symbol o in equation (2.94) is used to emphasize that the strain energy density function, W, is referred to the natural undeformed configuration.) Similarly, the incremental (2.94) and instantaneous rate type (2.80) constitutive relations are equivalent in form.

In summary, the linearized form of the stress increment can be written, in the reference configuration as

$$\Delta\mathbf{S} = \mathcal{C} : \Delta\mathbf{E}, \tag{2.96}$$

and in the current configuration as

$$\Delta\boldsymbol{\sigma}^{<r>} = \mathcal{L} : \Delta\boldsymbol{\varepsilon}, \tag{2.97}$$

where the incremental incompressible hyperelastic response moduli $\mathcal{C}$ and $\mathcal{L}$ are defined in equations (2.92) and (2.94), respectively.

Finally, the first integral term in equation (2.49) becomes

$$\begin{aligned}\int_{\mathcal{B}^r} tr\{\mathrm{G}_{\mathrm{x}}[\mathbf{T}]\,\delta\mathbf{F}\}d\Omega^r &= \\ \int_{\mathcal{B}^r} tr\left\{[\mathcal{C} : \mathrm{G}_{\mathrm{x}}[\mathbf{E}]]\,\delta\mathbf{E}\right\}d\Omega^r &+ \int_{\mathcal{B}^r} tr\left\{[\mathbf{S}\,\mathrm{G}_{\mathrm{x}}[\mathbf{F}^T]]\,\delta\mathbf{F}\right\}d\Omega^r.\end{aligned} \tag{2.98}$$

The corresponding finite incremental deformation equation is given by

$$\begin{aligned}\int_{\mathcal{B}^r} tr\{\Delta\mathbf{T}\,\delta\mathbf{F}\}d\Omega^r &= \\ \int_{\mathcal{B}^r} tr\left\{[\mathcal{C} : \Delta\mathbf{E}]\,\delta\mathbf{E}\right\}d\Omega^r &+ \int_{\mathcal{B}^r} tr\left\{[\mathbf{S}\,\mathbf{D}^T]\,\delta\mathbf{F}\right\}d\Omega^r.\end{aligned} \tag{2.99}$$

Alternatively, by assuming that the reference and spatial configurations coincide and are fixed in time, $\mathcal{B}^r = \mathcal{B}^t$, the incremental form of (2.99) for

the current configuration can be obtained with the aid of (2.7), (2.8), (2.21), (2.38), and (2.97) as

$$\begin{aligned} \int_{\mathcal{B}^r} tr\{\triangle\mathbf{T}\,\delta\mathbf{F}\}d\Omega^r \;&=\; \\ \int_{\mathcal{B}^t} tr\left\{[\mathcal{L}:\triangle\boldsymbol{\epsilon}]\,\delta\boldsymbol{\epsilon}\right\}d\Omega^t &+ \int_{\mathcal{B}^t} tr\left\{[\boldsymbol{\sigma}\,(\nabla_x\otimes\mathbf{u})^T]\,(\nabla_x\otimes\delta\boldsymbol{\chi})\right\}d\Omega^t, \end{aligned} \tag{2.100}$$

where $\nabla_x = \mathbf{F}^{-1}\nabla_X$.

2.10 Summary of the Incremental Equations

By replacing the first integral term in (2.50) with (2.100), a statement for the linearized governing equations for current configuration fixed at time t can be concluded as

$$\begin{aligned} \int_{\mathcal{B}^t} tr\left\{[\mathcal{L}:\triangle\boldsymbol{\epsilon}]\,\delta\boldsymbol{\epsilon}\right\}d\Omega^t + \int_{\mathcal{B}^t} tr\left\{[\boldsymbol{\sigma}\,(\nabla_x\otimes\mathbf{u})^T]\,(\nabla_x\otimes\delta\boldsymbol{\chi})\right\}d\Omega^t + \int_{\mathcal{B}^t}\rho\;\ddot{\mathbf{u}}\cdot\delta\boldsymbol{\chi}d\Omega^t \;&= \\ \int_{\mathcal{B}^t} tr\left\{\boldsymbol{\sigma}\,(\nabla_x\otimes\delta\boldsymbol{\chi})\right\}d\Omega^t - \int_{\mathcal{B}^t}\rho(\dot{\mathbf{v}}-\mathbf{b})\cdot\delta\boldsymbol{\chi}d\Omega^t + \int_{\partial\mathcal{B}^t_T}\mathbf{t}^{(n)}\cdot\delta\boldsymbol{\chi}d\Gamma^t, & \end{aligned} \tag{2.101}$$

where $\boldsymbol{\sigma} = \mathbf{T}$ and $J = 1$ when the reference and spatial configurations coincide. Further, from the incompressibility condition, $\rho/\rho^r = 1$. This completes the consistent linearization of the weak form of the boundary-value problem presented in section 2.5.

By introducing a more compact symbolic notation and replacing $\delta\boldsymbol{\chi}$ with $\delta\mathbf{u}$, equation (2.101) can be rewritten as

$$\mathcal{K}(\mathbf{u}) + \mathcal{M}(\ddot{\mathbf{u}}) \;=\; -\mathcal{F}^{int} + \mathcal{F}^{ext} - \mathcal{M}(\ddot{\mathbf{x}}), \tag{2.102}$$

where

$$
\begin{aligned}
\mathcal{K}(\mathbf{u}) &= \int_{\mathcal{B}^t} tr\,\{[\mathcal{L} : \Delta\boldsymbol{\varepsilon}]\,\delta\boldsymbol{\epsilon}\}\; d\omega^t + \int_{\mathcal{B}^t} tr\left\{[\boldsymbol{\sigma}\,(\nabla_x \mathbf{u})^T]\,(\nabla_x \delta\mathbf{u})\right\}\; d\omega^t, \\
\mathcal{M}(\ddot{\mathbf{u}}) &= \int_{\mathcal{B}^t} \rho\;\ddot{\mathbf{u}}\cdot\delta\mathbf{u}\, d\omega^t, \\
\mathcal{F}(\mathbf{x})^{int} &= \int_{\mathcal{B}^t} tr\,\{\boldsymbol{\sigma}\,\delta\boldsymbol{\epsilon}\}\; d\omega^t, \\
\mathcal{F}(\mathbf{x})^{ext} &= \int_{\mathcal{B}^t} \rho\mathbf{b}\cdot\delta\mathbf{u}\, d\omega^t + \int_{\partial\mathcal{B}^t_\sigma} \mathbf{t}^{(n)}\cdot\delta\mathbf{u}\, da^t, \\
\mathcal{M}(\ddot{\mathbf{x}}) &= \int_{\mathcal{B}^t} \rho\ddot{\mathbf{x}}\cdot\delta\mathbf{u}\, d\omega^t.
\end{aligned}
$$

Chapter 3

Non–Linear Finite Element Formulation

3.1 Introduction

In this study, the finite element method is used to obtain an approximate solution of a system of partial differential equations subject to known boundary conditions. This computational approach is based on the *weak* form of the *balance of momentum* equations. In general, the weak form may be based on a variational or weighted residual method. In this study, the *Galerkin weighted residual method* is used in conjunction with a *penalty* function to model the near incompressibility of soft cardiac tissue. In addition, a process of consistent linearization enables the non–linear problem to be solved iteratively as a sequence of linear problems. The generated system of linear equations is constructed and solved repeatedly using a Newton–Raphson type solution procedure to obtain a complete time–history response to the boundary–value problem.

In this study, the transient behaviour of the problem is not considered; hence, the inertia terms are neglected. This assumption reduces the complex-

ity of the problem to one of a non linear quasi static deformation. Further, the effects of $+G_z$ acceleration on the human ventricle myocardium are accounted for in the body force term, F^{ext}, of equation (2.102). The body force density, $\mathbf{b}$, simply becomes the gravitational acceleration due to $+G_z$ loading. For further detail on the finite element method for non linear problems the reader may refer to [2, 33, 36, 37, 57, 60].

3.2 Space – Time Discretization

The space domain, Ω, can be divided into subregions or *elements*, Ω^e, which are interconnected by a series of points or *nodes* on the element boundary. The independent field variable, ϕ, is approximated by a set of basis functions, N_I, and nodal field variables, $\hat{\phi}_I^e(t)$, as follows

$$\phi(\Omega^e, t) = \sum_{I=1}^{n_{en}} N_I(\Omega^e)\hat{\phi}_I^e(t), \tag{3.1}$$

for element e over the summation of n_{en} element nodes. The basis functions are continuous across an element interface; however, their derivatives need not be. Generally, these functions are selected as some k^{th} order interpolation polynomials and assumed C^0 continuous throughout the domain. Furthermore, the gradient of the approximated field variable, ϕ, can be obtained through differentiation of (3.1), as follows

$$\frac{\partial \phi(\Omega^e, t)}{\partial \mathbf{x}} = \sum_{I=1}^{n_{en}} \frac{\partial N_I}{\partial \mathbf{x}}(\Omega^e)\hat{\phi}_I^e(t). \tag{3.2}$$

Consider the time interval $\mathcal{I} = [0, T]$ with the time partitions $0 = t_0 < t_1 < t_2 < \cdots < t_N < t_{N+1} = T$. Where the n^{th} time interval is denoted by $\mathcal{I}_n = [t_n, t_{n+1}]$ for $n = 0, 1, 2, \ldots, N$. Further, one may consider the

space time domain of the problem as

$$Q = \sum_{n=0}^{N} Q_n^e = \sum_{n=0}^{N} (\Omega^e \times \mathcal{I}_n) \qquad e = 1, \ldots, n_{el}. \tag{3.3}$$

As mentioned previously, the finite element approach is based on the Galerkin weighted residual method, where the *trial* solutions, $\mathcal{U}^e \subset \mathcal{U}$, and *weighting* functions, $\mathcal{V}^e \subset \mathcal{V}$, for an element can be approximated by the interpolation polynomials, denoted by P^k. Therefore, the finite element space domain is defined as

trial solutions:

$$\mathcal{U}_n^h = \left\{ \mathbf{u}^h \mid \mathbf{u}^h \in C^0, \quad \mathbf{u}_e^h \mid_{Q_n^e} \in P^k, \quad \mathbf{u}^h = \mathbf{u}^h \quad \text{on} \quad \partial(\mathcal{B}_u^t)_n^h \right\},$$

weighting functions:

$$\mathcal{V}_n^h = \left\{ \delta\mathbf{u}^h \mid \delta\mathbf{u}^h \in C^0, \ \delta\mathbf{u}_e^h \mid_{Q_n^e} \in P^k, \quad \delta\mathbf{u}^h = 0 \quad \text{on} \quad \partial(\mathcal{B}_u^t)_n^h \right\}.$$

3.3 Governing Finite Element Equations

In formulating the governing finite element equations, the Galerkin function $\mathcal{G}(\boldsymbol{\chi}, \delta\boldsymbol{\chi})$ is approximated as the total accumulation of each element as

$$\mathcal{G}(\boldsymbol{\chi}, \delta\boldsymbol{\chi}) = \sum_{e=1}^{n_{el}} \mathcal{G}^e(\boldsymbol{\chi}^e, \delta\boldsymbol{\chi}^e). \tag{3.4}$$

where n_{el} is the number of elements. For numerical implementation of the discretized form of the Galerkin function, it is more convenient to consider the matrix representation of the stress and strain terms, as

$$\underset{\sim}{\boldsymbol{\sigma}} = \begin{Bmatrix} \sigma_1 \\ \sigma_2 \\ \sigma_3 \\ \sigma_4 \\ \sigma_5 \\ \sigma_6 \end{Bmatrix} = \begin{Bmatrix} \sigma_{11} \\ \sigma_{22} \\ \sigma_{33} \\ \sigma_{12} \\ \sigma_{23} \\ \sigma_{31} \end{Bmatrix} \qquad \underset{\sim}{\boldsymbol{\epsilon}} = \begin{Bmatrix} \epsilon_1 \\ \epsilon_2 \\ \epsilon_3 \\ \epsilon_4 \\ \epsilon_5 \\ \epsilon_6 \end{Bmatrix} = \begin{Bmatrix} \epsilon_{11} \\ \epsilon_{22} \\ \epsilon_{33} \\ 2\epsilon_{12} \\ 2\epsilon_{23} \\ 2\epsilon_{31} \end{Bmatrix}.$$

In addition, the instantaneous response moduli becomes

$$\underset{\sim}{\mathcal{L}} = \begin{bmatrix} \mathcal{L}_{1111} & \mathcal{L}_{1122} & \mathcal{L}_{1133} & \mathcal{L}_{1112} & \mathcal{L}_{1123} & \mathcal{L}_{1131} \\ & \mathcal{L}_{2222} & \mathcal{L}_{2233} & \mathcal{L}_{2212} & \mathcal{L}_{2223} & \mathcal{L}_{2231} \\ & & \mathcal{L}_{3333} & \mathcal{L}_{3312} & \mathcal{L}_{3323} & \mathcal{L}_{3331} \\ & & & \mathcal{L}_{1212} & \mathcal{L}_{1223} & \mathcal{L}_{1231} \\ & & & & \mathcal{L}_{2323} & \mathcal{L}_{2331} \\ Sym. & & & & & \mathcal{L}_{3131} \end{bmatrix},$$

by taking into account both minor and major symmetries. The underscored symbol, $\underset{\sim}{(\ )}$, is used to distinguish matrix representation from the corresponding tensor form.

Further, from equation (3.1) a description of the elemental geometry in the current configuration in terms of the nodal points, $\hat{\boldsymbol{\chi}}_I$, is given by

$$\boldsymbol{\chi}^e(\Omega^e, t) = \sum_{I=1}^{n_{en}} N_I(\Omega^e)\hat{\boldsymbol{\chi}}_I^e(t). \tag{3.5}$$

Similarly, the incremental displacement field for an element, $\mathbf{u}^e$, can be approximated in terms of the nodal displacements, $\hat{\mathbf{u}}_I^e$, as

$$\mathbf{u}^e(\Omega^e, t) = \sum_{I=1}^{n_{en}} N_I(\Omega^e)\hat{\mathbf{u}}_I^e(t). \tag{3.6}$$

In addition, from equations (2.42) and (2.43) the variational quantities, $\delta\boldsymbol{\epsilon}$ and $\delta\boldsymbol{\chi} = \delta\mathbf{u}$, in tensor notation become

$$\begin{aligned} \delta\boldsymbol{\epsilon}^e &= \frac{1}{2}\sum_{I=1}^{n_{en}} [(\nabla_x \otimes N_I\delta\hat{\mathbf{u}}_I^e) + (\nabla_x \otimes N_I\delta\hat{\mathbf{u}}_I^e)^T], \\ \delta\mathbf{u}^e &= \sum_{I=1}^{n_{en}} [N_I\delta\hat{\mathbf{u}}_I^e]. \end{aligned} \tag{3.7}$$

The corresponding vector representation for (3.7) is denoted by $\delta\underset{\sim}{\boldsymbol{\epsilon}}^e \in \Re^{6\times 1}$ and $\delta\underset{\sim}{\mathbf{u}}^e \in \Re^{n\times 1}$, where n is the number of degrees of freedom at an element node.

Since the inertia terms can be neglected, equation (2.102) reduces to

$$\underset{\sim}{\mathbf{k}}^{e}\ \hat{\underset{\sim}{\mathbf{u}}}^{e} \;=\; -\underset{\sim}{\mathcal{F}}^{e(int)} + \underset{\sim}{\mathcal{F}}^{e(ext)}, \tag{3.8}$$

for the e^{th} element. Using matrix representation, the approximate expressions $\delta\underset{\sim}{\boldsymbol{\epsilon}}^{e}$ and $\delta\underset{\sim}{\mathbf{u}}^{e}$ can be substituted into (2.102) yielding

$$\sum_{a=1}^{n_{en}}\sum_{b=1}^{n_{en}}(\delta\hat{\underset{\sim}{\mathbf{u}}}_{a}^{e})^{T}\left\{\left[\int_{e\mathcal{B}^{t}}\underset{\sim}{\mathbf{B}}_{L}^{a\,T}\,[\underset{\sim}{\mathcal{L}}]\,\underset{\sim}{\mathbf{B}}_{L}^{b}\,d\Omega^{e}+\int_{e\mathcal{B}^{t}}(\underset{\sim}{\mathbf{B}}_{NL}^{a})^{T}[\underset{\sim}{\boldsymbol{\sigma}}](\underset{\sim}{\mathbf{B}}_{NL}^{b})d\Omega^{e}\right]\hat{\underset{\sim}{\mathbf{u}}}_{b}^{e}\right.$$
$$\left.+\int_{e\mathcal{B}^{t}}\underset{\sim}{\mathbf{B}}_{L}^{a\,T}\underset{\sim}{\boldsymbol{\sigma}}\,d\Omega^{e}-\left[\int_{e\mathcal{B}^{t}}\rho\,\underset{\sim}{\mathbf{N}}_{a}^{T}\underset{\sim}{\mathbf{b}}\,d\Omega^{e}+\int_{\partial e\mathcal{B}_{T}^{t}}\underset{\sim}{\mathbf{N}}_{a}^{T}\,\underset{\sim}{\mathbf{t}}^{(n)}d\Gamma^{e}\right]\right\}=0, \tag{3.9}$$

where $\underset{\sim}{\mathbf{B}}_{L}^{a}$ is the linear strain displacement transformation matrix for node a of element e, such that $\delta\underset{\sim}{\boldsymbol{\epsilon}}^{e}=\sum_{I=1}^{n_{en}}\underset{\sim}{\mathbf{B}}_{L}^{a}\,\delta\hat{\underset{\sim}{\mathbf{u}}}_{a}^{e}$. If only translational degrees of freedom are present at each node, $\underset{\sim}{\mathbf{B}}_{L}^{a}$ has the form

$$\underset{\sim}{\mathbf{B}}_{L}^{a}=\begin{bmatrix}N_{a,1}&0&0\\0&N_{a,2}&0\\0&0&N_{a,3}\\N_{a,2}&N_{a,1}&0\\0&N_{a,3}&N_{a,2}\\N_{a,3}&0&N_{a,1}\end{bmatrix}.$$

Further, one may write $\underset{\sim}{\mathbf{B}}_{NL}^{a}$ as

$$\underset{\sim}{\mathbf{B}}_{NL}^{a}=\begin{bmatrix}N_{a,1}\,\underset{\sim}{\mathbf{I}}&|&N_{a,2}\,\underset{\sim}{\mathbf{I}}&|&N_{a,3}\,\underset{\sim}{\mathbf{I}}\end{bmatrix}^{T}.$$

Then, the stress matrix, $[\underset{\sim}{\boldsymbol{\sigma}}]\in\Re^{9\times9}$, appearing in (3.9) takes on the corresponding form

$$[\underset{\sim}{\boldsymbol{\sigma}}]=\begin{bmatrix}\sigma_{11}\,\underset{\sim}{\mathbf{I}}&\sigma_{12}\,\underset{\sim}{\mathbf{I}}&\sigma_{13}\,\underset{\sim}{\mathbf{I}}\\&\sigma_{22}\,\underset{\sim}{\mathbf{I}}&\sigma_{23}\,\underset{\sim}{\mathbf{I}}\\Sym.&&\sigma_{33}\,\underset{\sim}{\mathbf{I}}\end{bmatrix},$$

where $\mathbf{I} \in \Re^{3\times 3}$ is the identity matrix.

In this study, two types of three-dimensional continuum based elements are used to model the human heart undergoing $+G_z$ loading. The first is a 20-node isoparametric solid element [2], which is used to model the left and right ventricles. The second is an 8-node degenerate 3D continuum based shell element [3], used to model the conical fibrous membrane surrounding the heart called the pericardial sac. For the explicit form of $\underset{\sim}{\mathbf{B}}_L$, $\underset{\sim}{\mathbf{B}}_{NL}$, and $\underset{\sim}{\mathbf{N}}$ see Appendix B. Also, for a discussion of the geometric modelling considerations see Chapter 4.

Since $\delta\hat{\underset{\sim}{\mathbf{u}}}_a{}^t$ in equation (3.9) is arbitrary, the linearized equilibrium equation for a single element becomes

$$\left[\underset{\sim}{\mathbf{K}}_l^t + \underset{\sim}{\mathbf{K}}_{nl}^t\right] \hat{\underset{\sim}{\mathbf{u}}}^t = -\underset{\sim}{\mathbf{F}}^{t(int)} + \underset{\sim}{\mathbf{F}}^{t(ext)}. \tag{3.10}$$

Element Tangent Stiffness Matrices

Material stiffness:

$$\underset{\sim}{\mathbf{K}}_l^t = \int_{{}^t\mathcal{B}} \underset{\sim}{\mathbf{B}}_L^T [\underset{\sim}{\mathcal{L}}] \underset{\sim}{\mathbf{B}}_L \, d\Omega^t,$$

where

$$\underset{\sim}{\mathbf{B}}_L = \left[\underset{\sim}{\mathbf{B}}_L^1 \mid \underset{\sim}{\mathbf{B}}_L^2 \mid \cdots \mid \underset{\sim}{\mathbf{B}}_L^{n_{en}} \right].$$

Geometric stiffness:

$$\underset{\sim}{\mathbf{K}}_{nl}^t = \int_{{}^t\mathcal{B}} \underset{\sim}{\mathbf{B}}_{NL}^T [\underset{\sim}{\boldsymbol{\sigma}}] \underset{\sim}{\mathbf{B}}_{NL} \, d\Omega^t,$$

where

$$\underset{\sim}{\mathbf{B}}_{NL} = \left[\underset{\sim}{\mathbf{B}}_{NL}^1 \mid \underset{\sim}{\mathbf{B}}_{NL}^2 \mid \cdots \mid \underset{\sim}{\mathbf{B}}_{NL}^{n_{en}} \right].$$

Element Load Vectors

Internal nodal forces:

$$\underset{\sim}{\mathbf{F}}^{e(int)} = \int_{e\mathcal{B}^t} \underset{\sim}{\mathbf{B}}_L^T \underset{\sim}{\boldsymbol{\sigma}}\, d\Omega^t .$$

External body and surface loads:

$$\underset{\sim}{\mathbf{F}}^{e(ext)} = \underbrace{\int_{e\mathcal{B}^t} \rho\, \underset{\sim}{\mathbf{N}}^T \underset{\sim}{\mathbf{b}}\, d\Omega^t}_{\underset{\sim}{\mathbf{f}}^e_{body}} + \underbrace{\int_{\partial^e \mathcal{B}^t_T} \underset{\sim}{\mathbf{N}}^T\, \underset{\sim}{\mathbf{t}}^{(n)} d\Gamma^t}_{\underset{\sim}{\mathbf{f}}^e_{surf}},$$

where

$$\underset{\sim}{\mathbf{N}} = \left[\; N_1 \underset{\sim}{\mathbf{I}} \;\middle|\; N_2 \underset{\sim}{\mathbf{I}} \;\middle|\; \cdots \;\middle|\; N_{n_{en}} \underset{\sim}{\mathbf{I}} \;\right].$$

Element (Incremental) Displacement Vector

Nodal displacements:

$$\hat{\underset{\sim}{\mathbf{u}}}^e = \left\{(\hat{u}, \hat{v}, \hat{w})_1 \middle| (\hat{u}, \hat{v}, \hat{w})_2 \middle| \ldots \middle| (\hat{u}, \hat{v}, \hat{w})_{n_{en}}\right\}^T,$$

where $(\hat{u}, \hat{v}, \hat{w})_I$ is the incremental nodal displacement in the corresponding (x, y, z) direction at node I.

The elemental contributions of (3.10) can now be assembled to form the *Global* system of discretized equations in terms of the generalized variable $\hat{\mathbf{u}}$ by

$$\begin{aligned} \underset{\sim}{\mathbf{K}}_l &= \mathop{\mathbf{A}}_{e=1}^{n_{el}} \underset{\sim}{\mathbf{K}}^e_l & \underset{\sim}{\mathbf{K}}_{nl} &= \mathop{\mathbf{A}}_{e=1}^{n_{el}} \underset{\sim}{\mathbf{K}}^e_{nl} \\ \underset{\sim}{\mathbf{F}}^{(int)} &= \mathop{\mathbf{A}}_{e=1}^{n_{el}} \underset{\sim}{\mathbf{F}}^{e(int)} & \underset{\sim}{\mathbf{F}}^{(ext)} &= \mathop{\mathbf{A}}_{e=1}^{n_{el}} \underset{\sim}{\mathbf{F}}^{e(ext)} \end{aligned} \tag{3.11}$$

Finally, the global system of linear equations in compact form is given by

$$\left[\underset{\sim}{\mathbf{K}}_l + \underset{\sim}{\mathbf{K}}_{nl}\right] \underset{\sim}{\mathbf{u}} = -\underset{\sim}{\mathbf{F}}^{(int)} + \underset{\sim}{\mathbf{F}}^{(ext)} . \tag{3.12}$$

3.4 An Incremental Solution Procedure

It is apparent from the weak statement of the momentum balance, $\mathcal{G}(\mathbf{x}^*, \delta\boldsymbol{\chi}) = 0$, that the equality sign holds when $\mathbf{x}^*$ is an exact solution. However, for a locally linear approximation to the non-linear equation, equality is no longer guaranteed, and in general $\mathcal{G}(\hat{\mathbf{X}} + \mathbf{u}, \delta\boldsymbol{\chi}) \neq 0$. Assuming that $\mathcal{G}$ is sufficiently smooth within the neighbourhood of $\mathbf{x}^*$, such that $|\mathbf{x}^* - \mathbf{x}| < \epsilon^*$ where ϵ^* is a small quantity, a Newton Raphson iterative solution procedure can be adopted (eg. [50]). The incremental equation used for the numerical scheme is based on the linearized spatial form of equation (2.16), given as $L[\mathcal{G}(\mathbf{x}, \delta\boldsymbol{\chi}), \mathbf{u}]_{\bar{\mathbf{x}}} = 0$. A basic outline of the Newton Raphson algorithm is given as follows

(i)	Evaluate	$\mathbf{P}^i = \mathcal{G}(\mathbf{x}^i, \delta\boldsymbol{\chi}), \qquad \mathbf{K}^i = D\mathcal{G}(\mathbf{x}^i, \delta\boldsymbol{\chi})$
(ii)	Compute	$\mathbf{u}^{i+1} = -(\mathbf{K}^i)^{-1}\,\mathbf{P}^i$
(iii)	Update	$\mathbf{x}^{i+1} = \mathbf{x}^i + \mathbf{u}^{i+1}$
(iv)	Convergence	if $\|\mathbf{P}^i\|_2 < \epsilon^{**}\|\mathbf{P}^0\|_2$, *stop* else *go to* (i).

Convergence occurs when the residual load norm, $\|\mathbf{P}^i\|_2$, in any solution step is relatively *small* compared to the load norm for the increment, $\|\mathbf{P}^0\|_2$, where ϵ^{**} ($\epsilon^{**} \ll 1$) is the tolerance for convergence. For the above algorithm it is assumed that the iteration does converge. In practice, it may be more computationally efficient in mildly non-linear problems to adopt a modified Newton Raphson technique where $\mathbf{K}^i$ is computed once only at the beginning of each increment.

One may note that even though a linearized incremental solution scheme is used, it still includes all non-linear effects due to finite displacements, large strains and material non-linearities. In fact, these incremental equa

tions form the basis for the displacement-based finite element formulation. The system of equations generated by the linearization of the weak form of the balance of momentum, given by (3.12), for the Updated Lagrangian formulation becomes

$$\left[\underset{\sim}{\mathbf{K}}_{l} + \underset{\sim}{\mathbf{K}}_{nl}\right] \underset{\sim}{\mathbf{u}}_{n}^{i} \;=\; -\underset{\sim}{\mathbf{F}}_{n}^{i\,(int)} + \underset{\sim}{\mathbf{F}}_{n}^{i\,(ext)}, \tag{3.13}$$

where the subscript n refers to the increment and superscript i denotes iteration. Now, the element integration in (3.10) is carried out over $\mathcal{B}^t$ and $\mathcal{B}_I^t$ instead of $\mathcal{B}^t$ and $\mathcal{B}_T^t$, respectively, where the superscript bar denotes the most recently *known* configuration is adopted as the reference state for calculation purposes. Also, updating of the configuration and displacements is performed by

$$\mathbf{x}_n^{i+1} \;=\; \mathbf{x}_n^i + \mathbf{u}_n^i, \qquad \mathbf{u}_{o_n}^{i+1} \;=\; \mathbf{u}_{o_n}^i + \mathbf{u}_n^i, \tag{3.14}$$

where the subscript o refers to the original configuration.

Chapter 4

Human Heart: Modelling Aspects

4.1 Stages of Development

The development of the heart model can be divided into four stages. (The following pertains only to the heart model and is independent of the the oretical development, implementation and verification of the finite element software.) These stages are summarized as follows:

(i). Collection of Magnetic Resonance Imaging data for various cross sectional planes from a healthy human heart. From these images a three dimensional surface reconstruction of the heart is performed (section (4.1.1)).

(ii). Next, using the geometric surface data collected, a finite element discretization of the left and right ventricles is carried out (section (4.1.2)).

(iii). To ensure an accurate model for cardiac tissue, a realistic hyperelastic constitutive relationship given by equation (2.61) is incorporated into the FE analysis, with constants a and b determined from available experimental data (section (4.2)).

(iv). The determination and post-processing of $+G_z$ acceleration induced stresses in the left and right ventricles is obtained from a non-linear finite element analysis.

4.1.1 MRI imaging

In this study, the Magnetic Resonance Imaging (MRI) is used as a non-invasive visualization technique for the determination of anatomic size and orientation of the human heart [4, 15]. The MRI images provide quantitative (and qualitative) information from which a three-dimensional computer image of the heart can be constructed (see Figure 4.1). Alternate methods used by investigators for computer reconstruction of the heart include *in vivo* techniques using cine-angiocardiography, echocardiography, [16, 76, 82] and *in vitro* techniques from postmortem examinations [88]. A computer model was reconstructed using a collection of coronal, sagittal and transverse MRI images of the heart obtained during diastole (see Figure 4.2). Then, these images were digitized into a series of two-dimensional sectional contours giving the inner and outermost surface of the ventricles. Once obtained, these contours were assembled to form a three-dimensional silhouette of the left and right ventricles and chambers.

4.1.2 FE Discretization of the Ventricle Myocardium

An accurate description of the human heart requires the use of elements capable of conforming to the irregular geometry. For this particular problem, such elements are best developed based on a 3D continuum formulation. Further, these elements must be able to handle arbitrary large displacements and rotations while maintaining kinematically admissible displacement fields

Figure 4.1: Magnetic Resonance Imaging (MRI) of the human upper torso, outlining the (a) coronal and (b) sagittal profiles of the heart at the end of a diastolic phase [15].

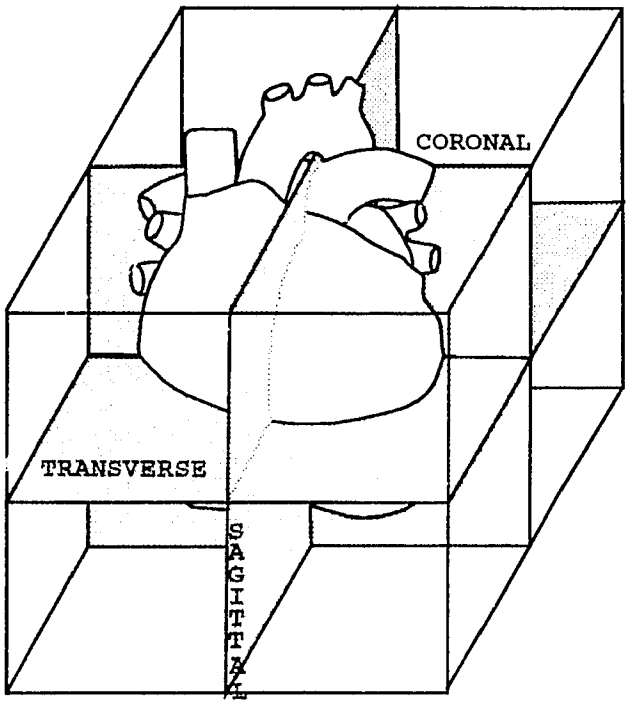

Figure 4.2: A depiction of the coronal, transverse and sagittal imaging planes used to construct a three-dimensional model of the left and right ventricles.

at element interfaces. Two such element types satisfying these conditions were selected for use. (see Figure 4.3).

In this study, the LV and RV are discretized using 20 node isoparametric solid elements [2, 37]. The ability of the element to model curved boundaries, non linear material and geometric behaviour is ideal for the problem at hand (see Figure 4.3). The FE matrices, generated for this element, are detailed in Appendix B.2.

Another element used is a degenerate 3D continuum based shell to model the conical fibrous membrane surrounding the heart and proximal portions of the cardiac vessel, commonly referred to as the pericardial sac. Original development of the 3D degenerate solid element to model a general doubly curved shell for linear analysis is found in [1]. Extension to the non-linear regime, where both geometric [2, 37] and material [79] nonlinearities are accounted for, has generated considerable interest and attention ever since. The shell element used is a non-linear C^0 type shell model that accounts for large membrane deformation. These non-linearities include both material (hyperelastic) and geometric (finite displacements / rotations) effects. The element displacement field is expressed in terms of three global displacements (u, v, w) and two local rotations (θ_1, θ_2) (see Figure 4.3). The FE matrices generated for this element are detailed in Appendix B.3. Further, it is assumed that the heart model has a plane of symmetry corresponding to the center coronal cross-section. By exploiting the property of symmetry, the finite element domain needs only involve half of the heart model.

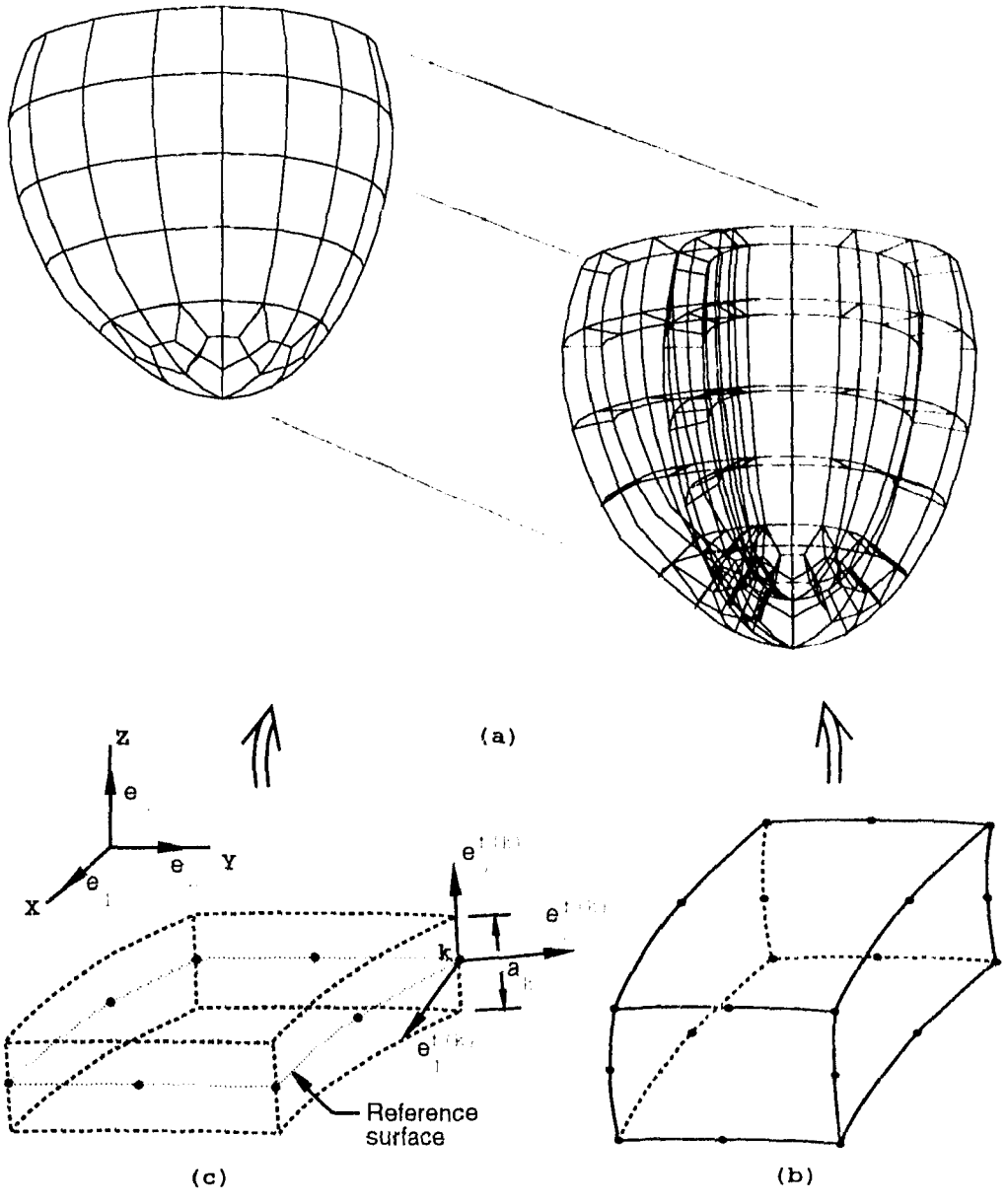

Figure 4.3: Finite element model of (a) the left and right ventricle myocardium with supporting pericardium membrane. The left and right ventricles are discretized using (b) 3D continuum based solid elements and accompanying pericardial sac using (c) shell elements.

4.2 A Constitutive Model for Myocardium and Pericardium

4.2.1 Myocardium

Myocardium of the ventricle is mostly composed of papillary muscles, Purkinje fibres, collagen, coronary arteries and blood fluid [83]. As with most biological tissue, the myocardium is assumed to be an incompressible material [20]. In addition, experiments reveal that the myocardium exhibits some degree of anisotropic, non-homogeneous, poro-viscoelastic behaviour [20, 56, 71, 88]. However, examples of successful models for myocardium tissue that assume isotropic, homogeneous, elastic material behaviour have been given (eg. [13, 23]). Measurement of cardiac properties (such as pressure, geometry, and fluid flow) is difficult and is generally obtained *in vivo*, whereas most of the knowledge associated with the mechanical properties of cardiac muscle is obtained from *in vitro* investigations. The in vitro investigations include several uniaxial and a few biaxial studies of excised cardiac tissue taken from animals [12, 69, 71, 85, 99].

Various constitutive relations have been proposed to model the deformation of soft tissue and cardiac muscle [13, 14, 21, 35, 44, 62, 63]. These stress/strain relationships are phenomenologically formed using experimental data to identify the macroscopic characteristics of the tissue. These relationships are usually exponential in form with *unknown* material parameters determined using a *least squares fit* to available experimental data. However, a general constitutive relation capable of describing all types of deformation behaviour is still not available. Therefore, it is desirable to employ a constitutive relationship that will fit the highly non-linear experimental data over

a wide range of strains.

Recently, a promising anisotropic constitutive relationship for passive cardiac tissue undergoing finite strain has been proposed [12, 13]. Therein, a strain energy function which represents the overall tissue behaviour as the sum of the *pseudo*-strain energies describing the (homogeneous) material *matrix*, $W_m(\mathbf{C})$, and (anisotropic) *fibre*, $W_f(\alpha)$, parts is given as

$$W(\mathbf{C}, \alpha) = W_m(\mathbf{C}) + W_f(\alpha)$$

where α is the stretch ratio associated with muscle fibre direction.

Absence of a reliable constitutive relationship to model the anisotropic viscoelastic material behaviour of the human heart has led to the adoption of a simpler approach, wherein the cardiac tissue is considered to be a homogeneous isotropic non-linear elastic material. In this study, the exponential strain energy function proposed for soft biological materials [21] and subsequently used for cardiac tissue [14, 99] of the form

$$\hat{W}(I_1) = a[e^{b(I_1-3)} - 1],$$

is used. The constants a and b are selected from experimental data given in [44] for uniaxial and biaxial tests on excised myocardium tissue, as $a = 191.4$ Pa (1.951 g/cm^2) and $b = 11.39$.

4.2.2 Pericardium

Structural interaction of the heart with its surrounding anatomy is accounted for in the analysis, by including the protective pericardial membrane surrounding the human heart [95]. Further, it is known that under high $+G_z$

loading conditions the ventricles undergo significant deformation, which results in load transfer between the heart and supporting pericardial membrane. From experimental studies of canine, researchers have found that the pericardium significantly influences the pressure-volume relationship of the heart [24, 32, 66]. This gives evidence to suggest that the pericardium provides a restraining action during diastole, which limits cardiac dilation.

Experimental data from excised human pericardial tissue indicate that it is reasonable to model the pericardium as an incompressible isotropic elastic membrane [51]. Although experiments indicate some degree of anisotropy and viscoelasticity, the human pericardium is nearly isotropic [9, 52, 53, 70]. This may be due to the even distribution of layers of interwoven collagen fibres. Also, measurements of pericardium thickness in five human subjects range from 0.52 to 0.58 mm, with mean 0.55 ± 0.03 mm [51].

Further, the deformation behaviour of human pericardium is capable of developing large strains. Under biaxial loading the pericardium initially extends with little resistance for a stretch ratio λ under 1.09, and then becomes almost inextensible when the tension reaches about 1962 Pa (20 g/cm^2) with $\lambda = 1.12$. Since the hyperelastic constitutive relationship given in [14] can apply to soft biological tissue, it is also used to model the pericardium. The *best fit* material constants for equation (2.64) are determined analytically to be $a = 2.91$ Pa (0.03 g/cm^2) and $b = 40$ using biaxial experimental data for human pericardium [51].

Chapter 5

Analysis Software and Verification

5.1 Software Modules

A special-purpose *in house* software package, which integrates 3 D graphics capabilities with the finite element program, is developed for the analysis of $+G_z$ acceleration induced stress in the ventricles. In essence, the package consists of three modules, namely:

a) DIGIT: MRI Data Digitization and Ventricle Reconstruction.
b) HEART: Non-linear FE Analysis Program.
c) FEGPRO: 3-D FE Graphical Pre/Post-Processor.

The software developed is modular in nature since each application is self contained, with data generated from one stage used as the input for the subsequent stage.

The finite element software package has been implemented using the C programming language [49]. The C language was chosen due to its inherent ability to handle data structures. Also, its "standard" callable dynamic

memory allocation routines facilitate optimal use of computer resources. The C language allows for a set of variables to be treated as a group under a common name using *structures*. These structures provide the means for effective data organization, where *members* within a structure can be of any data-type or even other structures.

A pre/post processor with 3-D colour capability is written to reduce the tedious and often error-prone task of preparing detailed input files and to aid in the interpretation of voluminous output from a finite element analysis. The pre-processor with a graphical interface assists in the construction of the finite element model of the ventricles, whereas the post-processor is used to provide a clearer interpretation of the finite element results.

The graphics processor is interactive with screen-driven menus for ease of use (see Figure 5.1). The highly interactive program allows for real-time control of geometric manipulations by scaling, rotation, translation, clipping, multiple views, *Gourand* shading, and hidden surface removal. Further, the software is written to exploit the graphics library routines supported by PHIGS: *Programmer's Hierarchical Interactive Graphics System* [89].

As mentioned, the major function of the post-processor is to give a clearer understanding of the FE results. This is best done in a pictorial format, in which the vast quantity of output data from the FEA is reduced to a manageable level of information. The FEA results can be displayed visually using displaced shapes and/or colour contours. Displaced shapes are typically vector components such as displacements, which can be emphasized by exaggeration of the deformed mesh. Colour contours are used to display scalars or one component of a vector field (eg. pressure or principal stress). Also, the continuous colour display enables quick location of critical

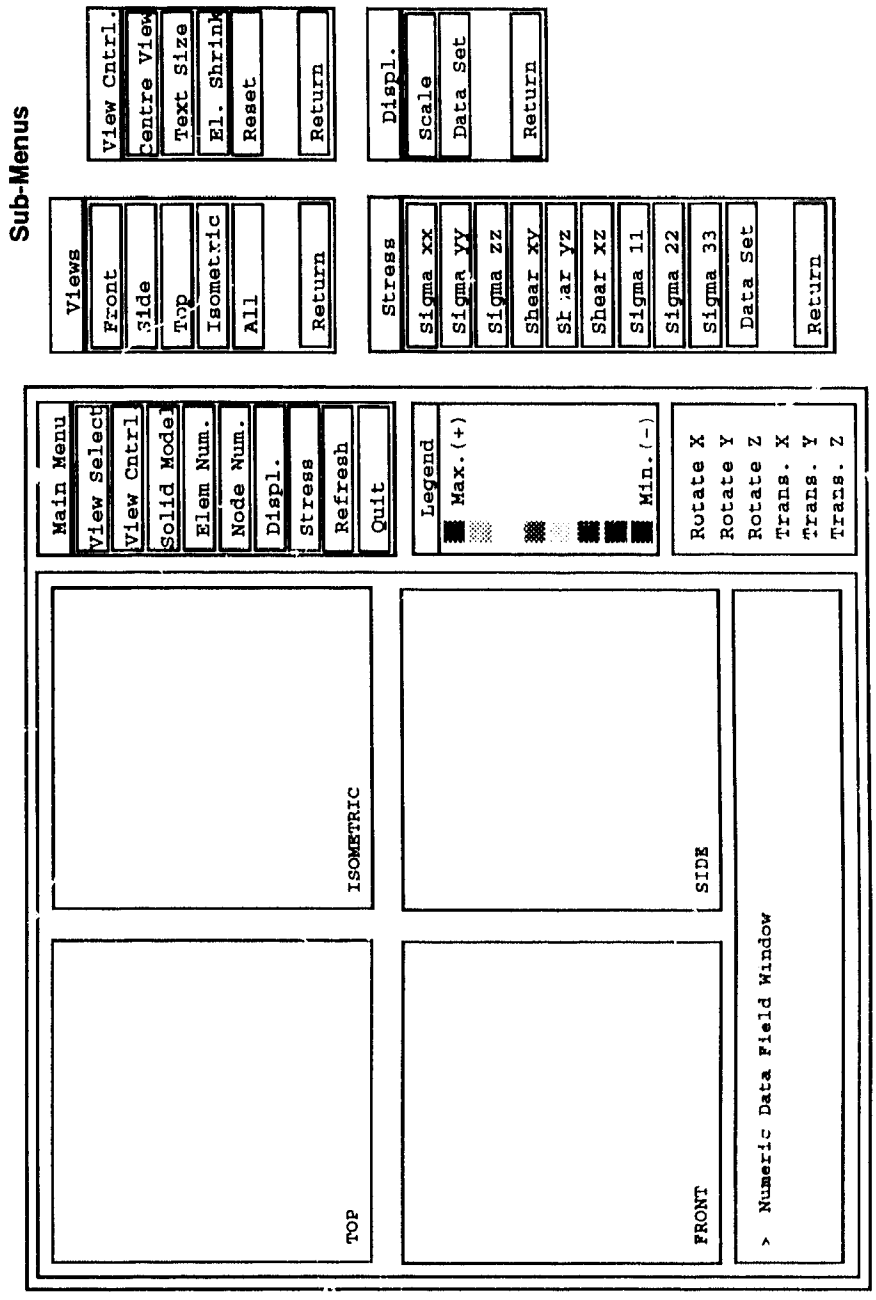

Figure 5.1: Display layout of the FEGPRO: *Finite Element Graphics Processor* showing the screen-driven menu system.

stress areas. Herein, colour contouring is combined with Gourand shading and hidden surface removal for a clear definition of shape and surface stress pattern.

5.2 Computational Verification and Testing

Several numerical simulations are performed to demonstrate the predictive capabilities and convergence characteristics of the non-linear FE software developed. These simulations contain both linear and non-linear geometric (finite displacements / rotations) and material (incompressible) effects. Comparisons of numerically generated results with closed form solutions, and experimental data from other researchers, are included if available. Verification of the finite element program developed is achieved by using a series of test cases involving plate, cylindrical, and spherical shell structures subject to various loadings. In the order of increasing complexity, the software verification consists of test cases involving:

- Inextensional Deformation
  - Convergence characteristics
  - Mesh sensitivity tests
- Non-linear Geometric Behaviour
  - Non-conservative loading
  - Finite rotations with *small* strains
  - Configuration (stress) updating
- Non-linear Material and Geometric Behaviour

Hyperelastic (incompressible) materials,

(ie. Mooney-Rivlin and biological constitutive models)

For problems involving linear-elastic isotropic behaviour, the material response tensor in component form is given by

$$\mathcal{C}_{ijkl} = \mu(\delta_{ik}\delta_{jl} + \delta_{il}\delta_{jk}) + \lambda\delta_{ij}\delta_{kl}, \tag{5.1}$$

where μ and λ are Lamè's constants and δ_{ij} is the Kronecker delta. In terms of Young's modulus, E, and Poisson's ratio, ν, Lamè's constants are

$$\mu = \frac{E}{2(1+\nu)}, \qquad \lambda = \frac{\nu E}{(1+\nu)(1-2\nu)}.$$

A shear correction factor of 5/6 has been applied to the (lamina) in plane shear moduli for the case of the degenerate shell element.

Due to the limited availability of analytical and numerical results for biological materials, additional verification of the algorithm is performed by implementing an incompressible hyperelastic Mooney Rivlin model for rubber and rubber-like solids (ie. elastomers) [58, 78], for which analytical solutions and standardized benchmark tests exist [26, 77]. For these problems, the particular form of the strain-energy density function for incompressible isotropic material is assumed to be

$$W = \frac{\mu}{2}[c(I_1 - 3) + (1-c)(I_2 - 3)], \qquad \text{for } 0 < c < 1, \tag{5.2}$$

where I_1 and I_2 are the strain invariants and c is a material parameter. For the case $c = 1$, the strain energy function for *neo-hookean* materials is obtained. The incremental constitutive relation for the finite element implementation is derived using (5.2) in accordance with the theory presented in section (2.8).

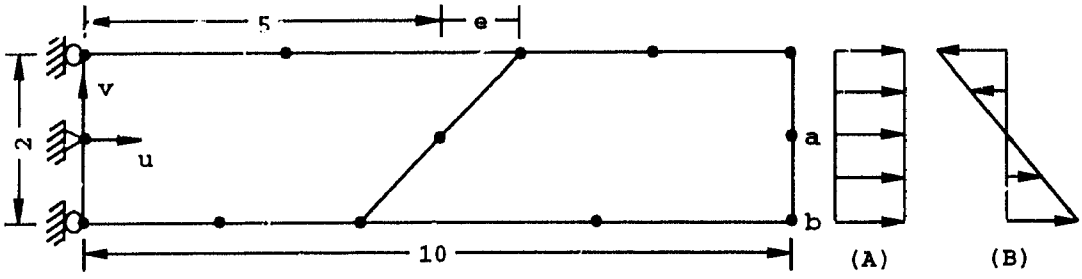

Figure 5.2: An engineering patch test for (A) plane stress and (B) bending.

5.2.1 Linear Examples

An Engineering Patch Test

Consider first an engineering *Patch* test of the plane stress and pure bending problems as shown in Figure 5.2. In practice, the patch test is considered as a *necessary* condition for finite element convergence [16, 92]. Tests are carried out on the quadratic shell and solid elements using Full (FI), Reduced (RI), and Selective (SRI) Gaussian quadrature, see Appendix B. The results for the pure bending case giving horizontal u and vertical v displacements at points a and b are given in Table 5.1. Both elements are found to satisfy the patch test, except when using a reduced ($2 \times 2 \times 2$) quadrature rule to integrate the solid element, a *spurious* zero-energy mode is produced. The results for the plane stress case are found to be in exact agreement with theory.

5.2.2 Non-linear Geometric Examples

Bending of a Cantilever Beam

A slender cantilever beam subjected to a concentrated end moment is analysed. This case demonstrates the ability of the program to handle large

Table 5.1: Normalized *Patch* Test Results for Bending ($E = 1000$, $\nu = 0.3$)

Element	Quadrature	ϵ	u_b	v_t	v_b
Solid	$3 \times 3 \times 3$	0	1.000	1.000	1.000
	$2 \times 2 \times 2$ *		0.997	1.000	0.998
	14 pt.**		1.000	1.000	1.000
Shell	$3 \times 3 \times 2$	0	1.000	1.000	1.000
	$2 \times 2 \times 2$		1.000	1.000	1.000
Solid	$3 \times 3 \times 3$	1	0.969	0.906	0.917
	$2 \times 2 \times 2$ *		1.058	0.987	1.025
	14 pt.		0.967	0.906	0.916
Shell	$3 \times 3 \times 2$	1	0.993	0.993	0.991
	$2 \times 2 \times 2$		1.000	1.000	0.998
Exact***			1.000	1.000	1.000

* Spurious zero energy mode suppressed.
** For 14 pt. rule see [29].
*** Exact values $u_b = 0.150$, $v_t = 0.750$, and $v_b = 0.75225$

displacements and rotations with *small* strains. Material and geometric data used in the calculations are as follows: Young's Modulus $E = 30 \cdot 10^6$ lbs/in.^{2}, length $L = 12$ in., width $b = 1$ in., and thickness $h = 0.1$ in.. The cantilever beam is modelled using six shell type elements with $(2 \times 2 \times 2)$ reduced integration. Converged solution results are obtained using 50 load increments of size $\Delta M/M_0 = 0.0$. $(M_0 = 2\pi EI/L)$. A comparison of the predicted response with the analytical solution [19] is given in Figure 5.3. In addition, a plot of the deformed configurations at several load stages is shown in Figure 5.3. From Figure 5.3, it is evident that the predicted response is in close agreement with the analytical solution up to $\varphi = \pi/2$ radians, with a noticeable but small deviation thereafter.

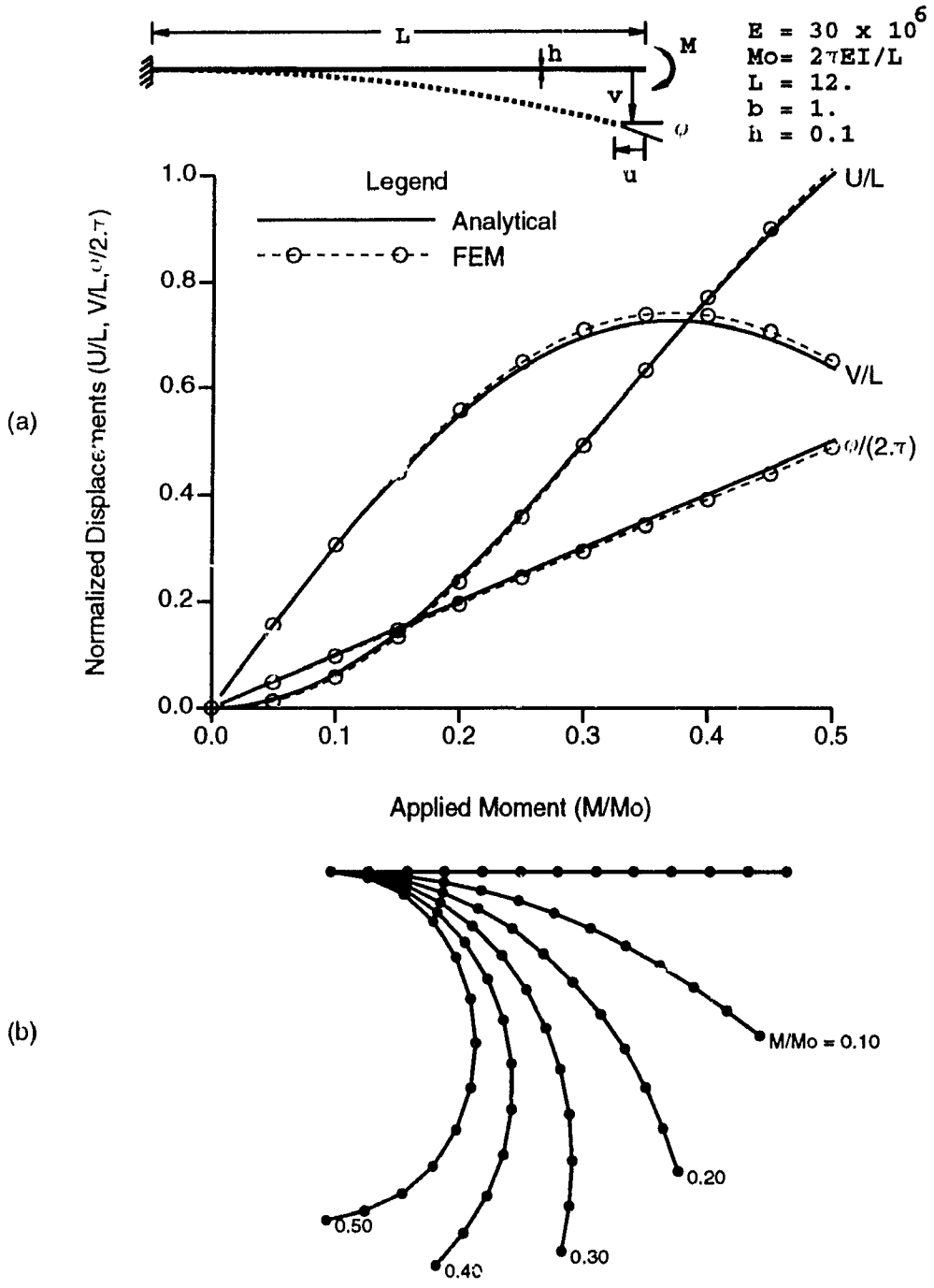

Figure 5.3: A cantilever beam under a pure moment. Plots of (a) normalized displacement versus applied moment with (b) deformed configurations for various applied moments.

Snap–through Buckling of a Circular Arch Structure

A shallow cylindrical shell structure subjected to a concentrated load at the center, is hinged at the longitudinal edges and free along the curved boundaries (Figure 5.4). Under loading the structure eventually reaches a critical point where additional loading can not be sustained. Beyond this *limit* point of bifurcation the load deflection curve exhibits a "softening" effect, which corresponds to a negative definite stiffness matrix. To overcome this numerical difficulty a displacement controlled scheme is adopted. A technique originally proposed by Riks / Wempner [75, 74, 96] using *arc length-control* and subsequently modified by Ramm [73] is implemented in the finite element program for problems exhibiting quasi static structural instability. The displacement control procedure is usually applied near and along the critical path, however, it can be applied over the entire response.

For this example, only one quarter of the shell structure is modelled with 16 shell type elements. The load-deflection response for the center and edge points is obtained using a total of 44 increments (see Figure 5.4). Moreover, the numerically generated response is compared with that of Ramm [73] and is found to agree. It is interesting that the structure exhibits both *snap-through* as well as *snap-back* buckling phenomena.

5.2.3 Non-linear Geometric and Material Examples

An Equi-biaxial Study of Passive Myocardium

To study the myocardium constitutive relation proposed for the heart model, an equi-biaxial simulation of a thin excised myocardial strip is performed. Further, a comparison of experimentally obtained equi biaxial myocardial

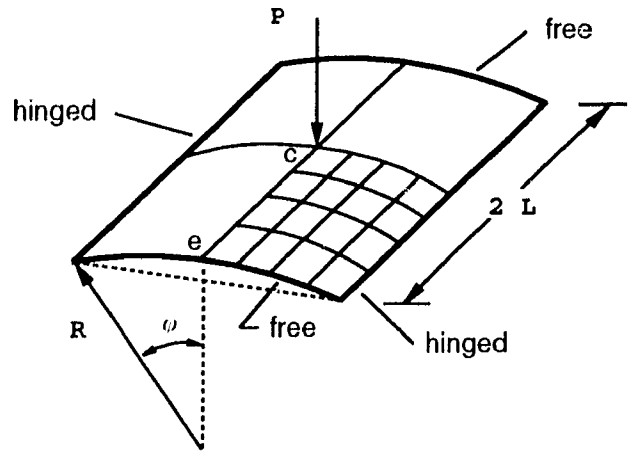

E = 3.103 kN/mm^2
ν = 0.3
R = 10 L mm
L = 2540. mm
h = 6.35 mm
φ = 0.1 rads.

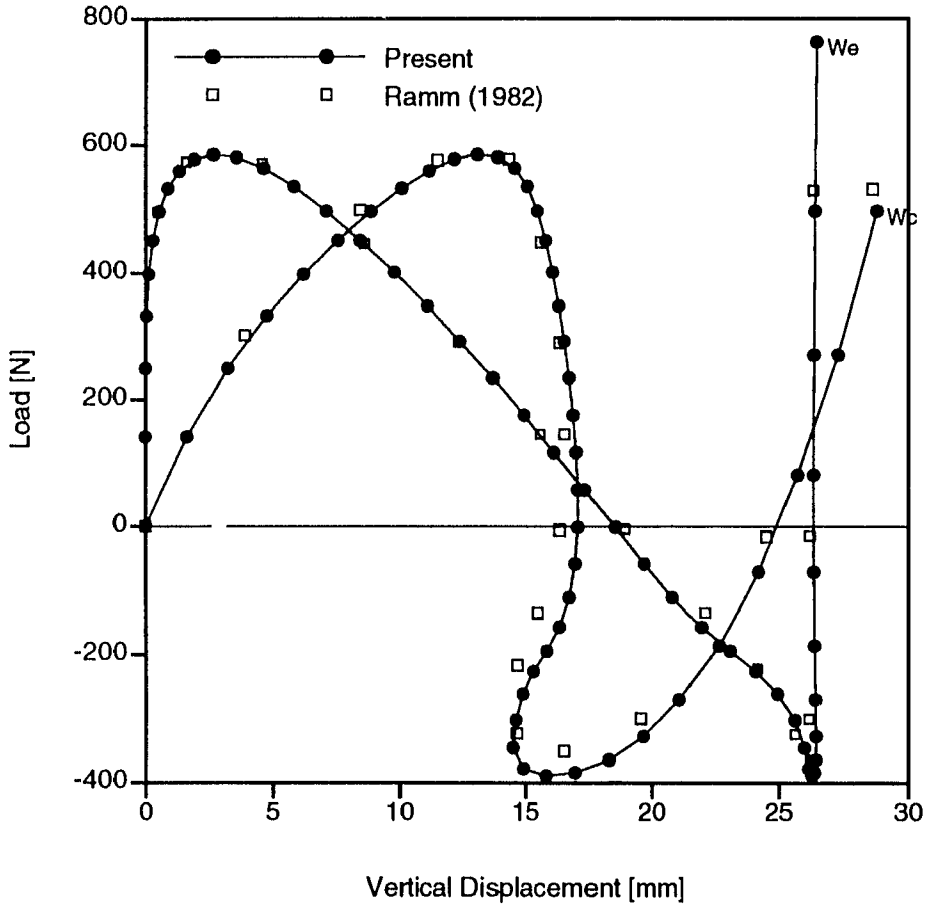

Figure 5.4: Post buckling of a circular arch structure.

data with theoretical and numerical predictions is used to demonstrate the accuracy of the model. The biaxial data is obtained from [99] where a thin slice ($1.2\ mm$) of myocardium ($3 \times 3\ cm$) was subjected to an equi-biaxial tension. For reasons of symmetry, it is only necessary to solve for one quarter of the specimen by applying the appropriate boundary conditions. The FE meshes used consist of (a) a solid type element with a 14 point integration rule, and (b) a shell type element with selected reduced integration.

For the cross-fibre direction, the constants a and b defined in equation (2.64) are chosen from the *best fit* parameters for stress strain data shown in [44], as $a = 191.4\ Pa$ ($1.951\ g/cm^2$) and $b = 14.39$ (for specimen II with $E_{11}/E_{22} \approx 1$).

For the fibre direction the material constants are determined analytically to be $a = 276.6\ Pa$ ($2.82\ g/cm^2$) and $b = 14.86$. Results of the FE predicted and experimental Cauchy stresses are given in Figure 5.5. In addition, the theoretical response is derived for the fibre and cross fibre stresses using equation (2.63) as

$$\sigma_{xx} = \sigma_{yy} = 2abe^{b(I_1-3)}\left[\lambda^2 - \lambda^{-4}\right] \tag{5.3}$$

where λ is defined as the principal stretch ratio. The material constants a and b are selected to predict the behaviour of the fibre and cross fibre experimental data and, as expected, these results are in good agreement with both the experimental data and theoretical curves. However, the anisotropic and viscoelastic behaviour of passive myocardium plays an important role in the interaction of stress and deformation and can significantly effect the constants a and b.

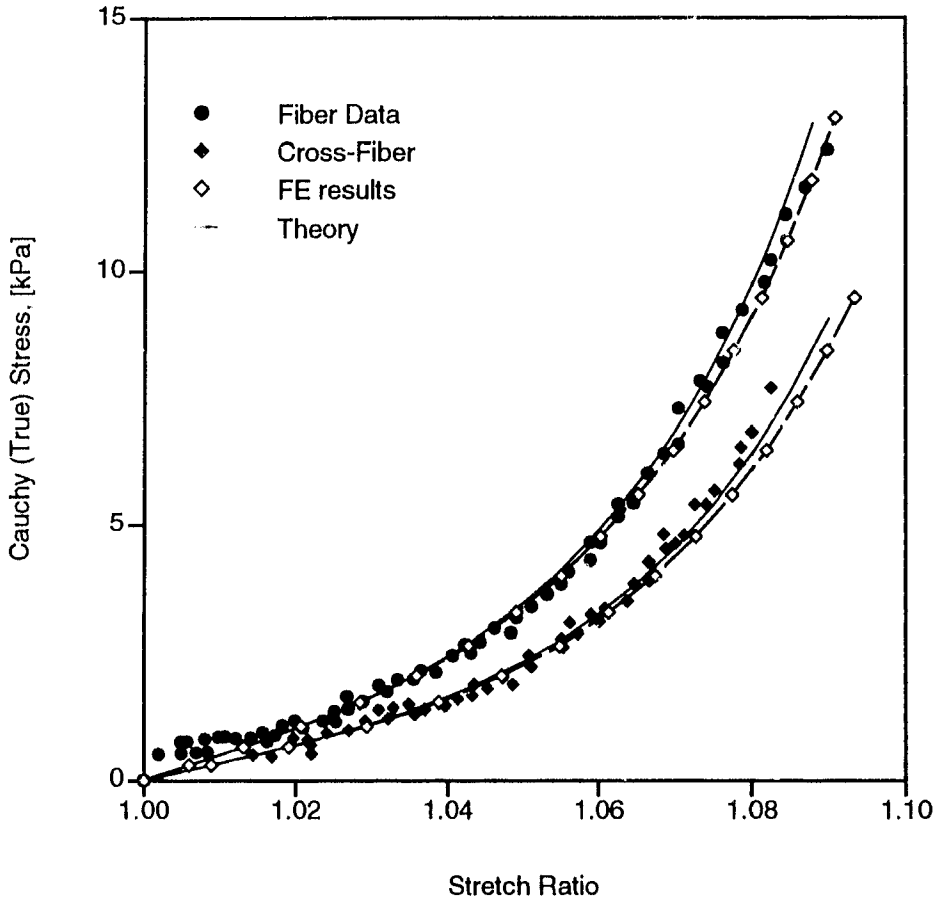

Figure 5.5: Comparison of experimentally obtained equi-biaxial myocardial data with theoretical and computed FE predicted responses. Results obtained using best fit parameters for the fibre direction [$a = 276.6\ Pa$ (2.82 g/cm^2), $b = 14.86$] and cross-fibre direction [$a = 191.4\ Pa$ (1.951 g/cm^2), $b = 14.39$]. Experimental data taken from Yin et al. [99].

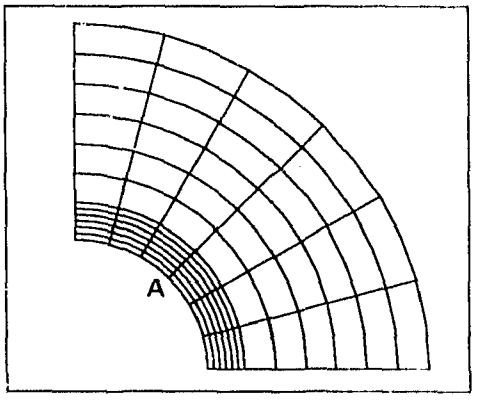

Figure 5.6: FE mesh of a thick walled cylinder with initial inner radius $r_i = 7.0$ in. and outer radius $r_o = 18.625$ in..

A Thick Cylinder Under Internal Pressure

Consider the problem of a thick cylinder subjected to an internal pressure. The cylinder is assumed to be infinite in length (plane strain condition) with an internal radius $r_i = 7.0$ in. and outer radius $r_o = 18.625$ in.. The material is assumed to be rubber and obeys Mooney Rivlin's equation (5.2) with $\mu/2 = 100$ psi and $c = 0.8$. Further, the theoretical solution for an incompressible material given in [77] is used to verify the computational algorithm developed.

One quarter of the cylinder is modelled using a total of 72 solid type elements (6 in the circumferential and 12 in the radial direction of unit thickness) with appropriate boundary conditions applied (see Figure 5.6). Internal pressure increments of 10 psi are applied until a maximum of 150 psi is reached. Both computed and analytical solutions of pressure versus dis

placement response for the inner wall (at node A) are shown in Figure 5.7. Also, the corresponding hoop stress versus inner displacement is included. It is evident from these findings that there is good agreement between the computational and analytical solutions.

Inflation Response of a Thin Sphere

A hollow thin sphere of initial inner radius $r_i = 100\ mm$ and outer radius $r_o = 102\ mm$ is subjected to a (non-dimensionalized) internal pressure, $p_o/\bar{\mu}$. The material is assumed to be neo-hookean, where $c = 1$ in equation (5.2). The theoretical solution for the inflation of a sphere given in [26] is used to verify the computational algorithm.

Due to symmetry, only one eighth of the sphere is modelled using a total of 108 elements with appropriate boundary conditions applied (Figure 5.8). Computed and analytical solutions of pressure versus stretch ratio (r/r_i) for the inner wall (at node A) are shown in Figure 5.9. Also, the corresponding circumferential stress versus stretch ratio is included. It is evident from these findings that there is good agreement between the computational and analytical solutions.

(a)

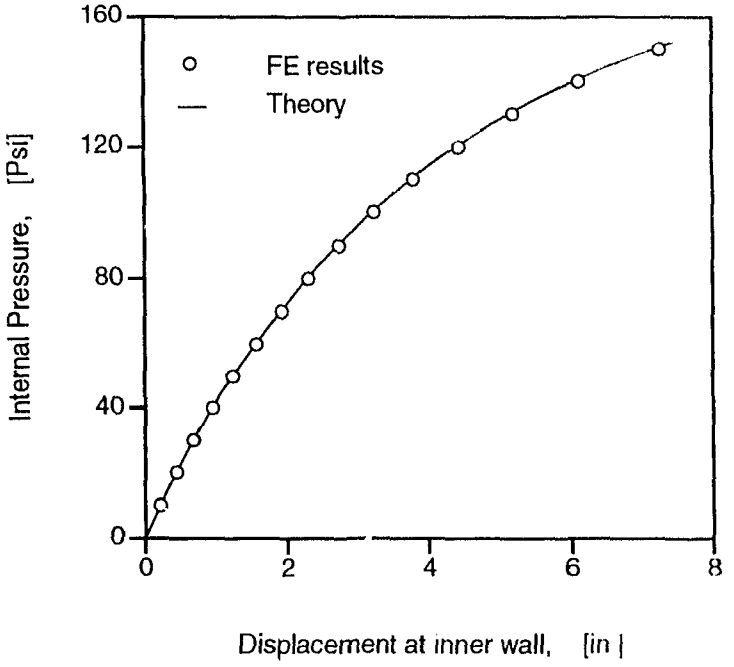

(b)

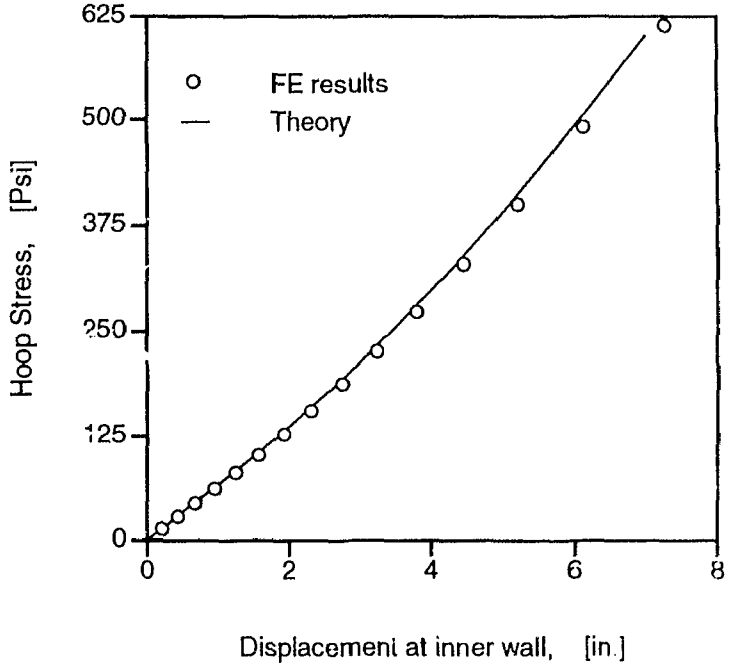

Figure 5.7: Plots of (a) internal pressure versus inner displacement and (b) hoop stress versus inner displacement of a thick wall cylinder comparing the FE predicted and theoretical solutions.

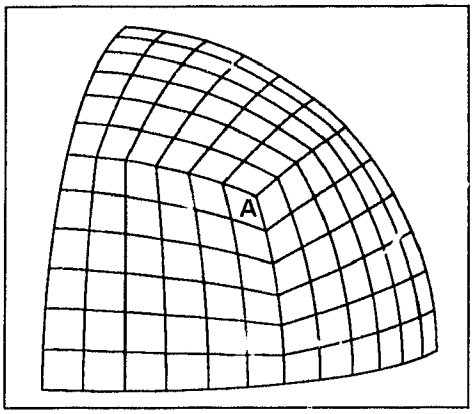

Figure 5.8: FE mesh of a thin sphere with initial inner radius $r_i = 100\ mm$ and outer radius $r_o = 102\ mm$.

(a)

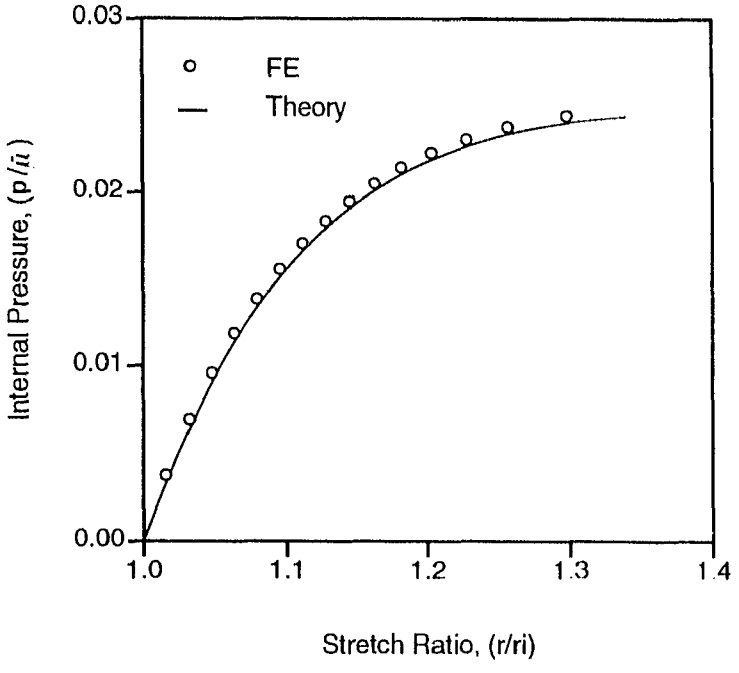

(b)

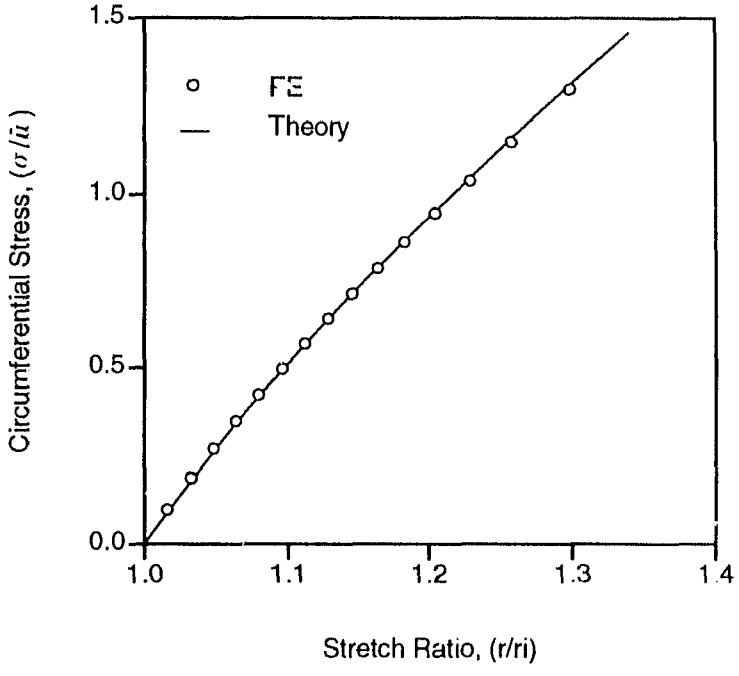

Figure 5.9: Plots of non-dimensionalized (a) inflation pressure versus stretch ratio and (b) circumferential stress versus stretch ratio of a thick wall cylinder comparing the FE predicted and theoretical solutions.

Chapter 6

Human Heart: Analysis and Discussion

In this study, a quasi-static finite element analysis is performed for the (passive) diastolic phase of the cardiac cycle under $+G_z$ loading conditions. This research work is regarded as a preliminary study of the effects of $+G_z$ induced stresses in the human myocardium. The results obtained demonstrate the ability of the non-linear finite element model developed to provide quantitative data of gross distortion and stress in the heart undergoing sustained inertia loading. However, since experimental data for the heart under $+G_z$ acceleration is not presently available, a comparison of numerically generated deformation profiles with that obtained experimentally is not possible.

The finite element model of the heart consists of the left and right ventricles with separating inter-ventricular septum. In addition, the surrounding pericardial membrane is included in the analysis. The ventricles and septum are discretized using 81 solid elements, and accompanying pericardial sac is discretized using 56 shell elements (see Figure 6.1). This leads to a system of equations with approximately 2500 unknown displacements to be solved

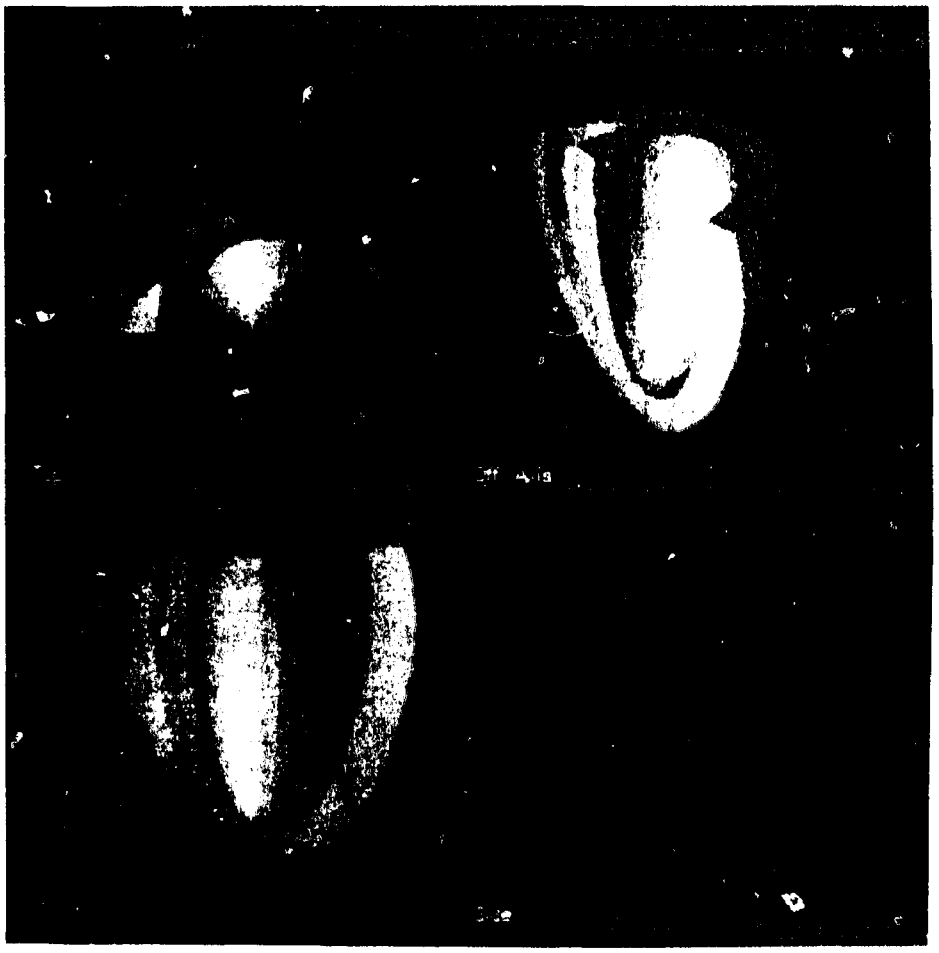

Figure 6.1: Multiple views of the human heart model, displayed using I-DEAS PRO graphics preprocessor package with solid model and shading option selected.

for at each step.

The analysis is performed using an acceleration load increment of $g/4$, where g is the acceleration due to gravity (9.80665 m/s^2 at sea level and 45° latitude), until a maximum acceleration level of $+5\ G_z$ is achieved. The cavity pressure acting on the epicardial surface, due to the total blood volume of 200 ml in the LV and RV, is accounted for in the analysis (where the specific gravity of blood is taken as 1.057 [91]). Unfortunately, experimentally obtained ventricle cavity and external surrounding hydrostatic pressure versus G_z loading is not available for implementation in the finite element model. However, it is possible to use existing data obtained from experiments on miniature swine [17, 87] to deduce the corresponding response patterns to that in man.

Results displaying gross distortion of the coronal mid-plane section of the heart at rest, 2.5 G_z, and 5.0 G_z acceleration levels are shown in Figure 6.2. In addition, principal stress levels, σ_{11}, at various points along the left ventricle endocardium wall versus $+G_z$ acceleration are shown in Figure 6.3. Further, predicted stress levels and gross distortion in the human heart at $+5\ G_z$ loading are displayed in Figure 6.4. It is evident from Figure 6.4 that with increase of G_z load the heart tends to elongate.

The presence of the stout papillary muscles and inelastic tendons called *chordae tendineae* which forms a tree like structure in the ventricles is not accounted for at present. The degree to which they affect the gross distortion and stress distribution near the endocardial surface of the heart wall undergoing $+G_z$ loading is still unknown. However, it is expected that these muscle fibres would become highly stressed under such conditions due to their intricate tree like structure which effectively bridges across the ventri-

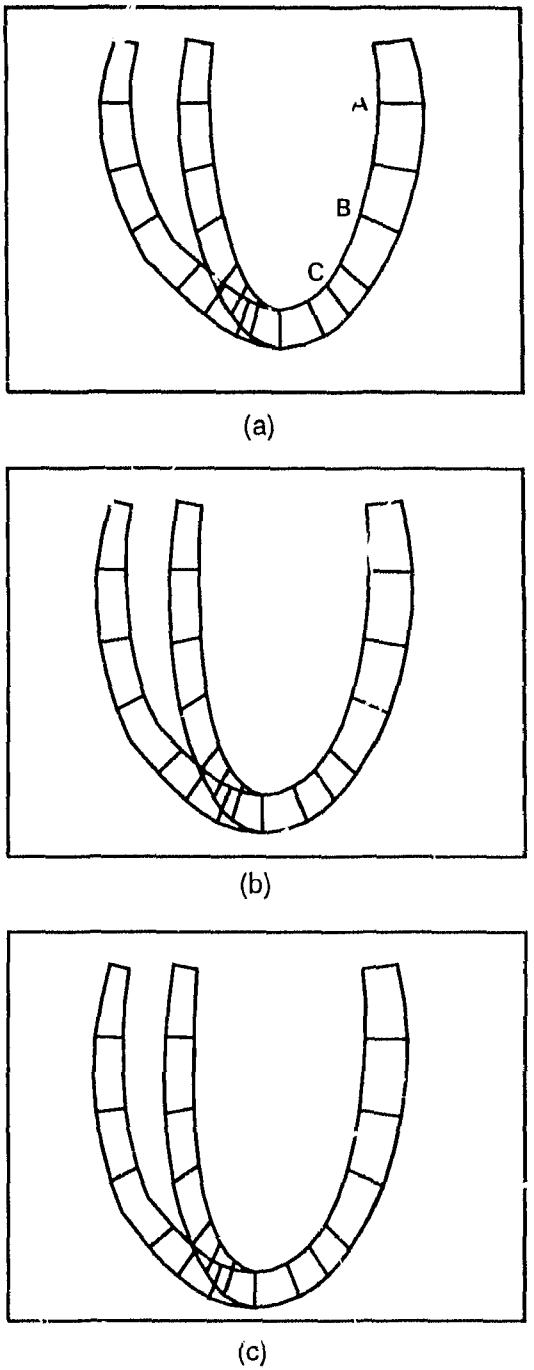

Figure 6.2: Deformation profiles of the coronal mid plane section of the heart showing predicted gross displacements of the heart wall at (a) rest, (b) +2.5 G_z, and (c) +5.0 G_z acceleration levels.

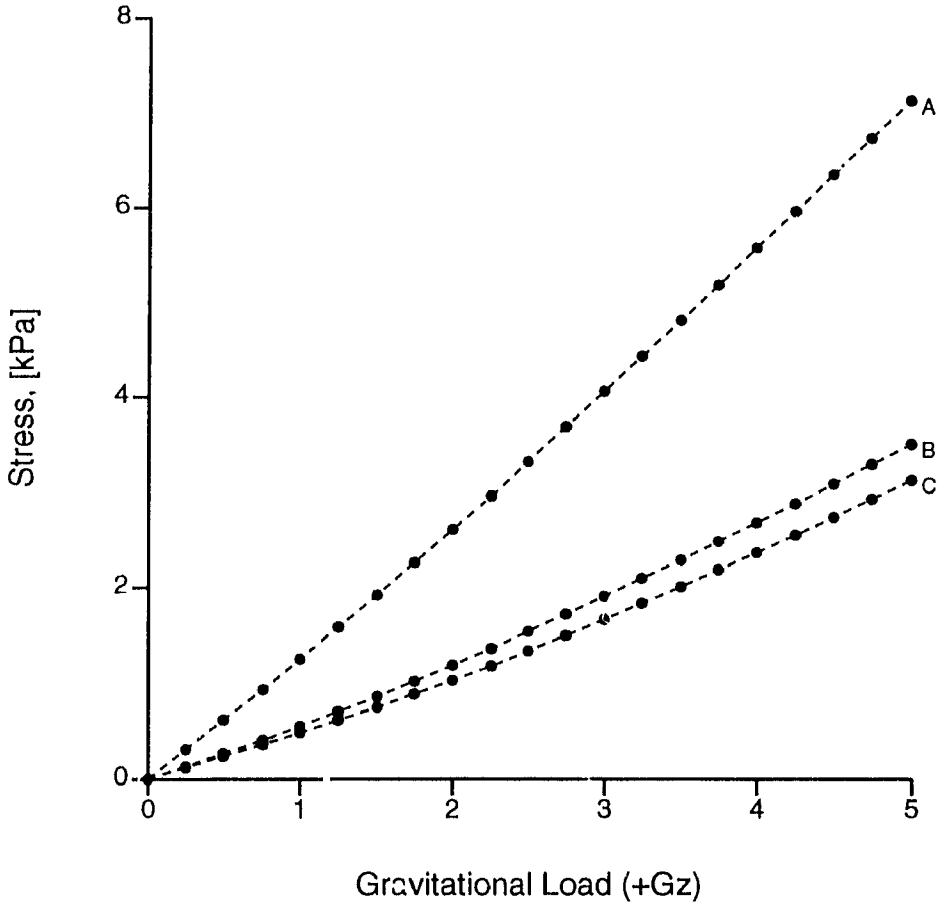

Figure 6.3: Principal stress σ_{11}, variation along the left ventricle endocardium wall versus gravitational load $+G_z$ (at locations [A,B,C] denoted in Figure 6.2).

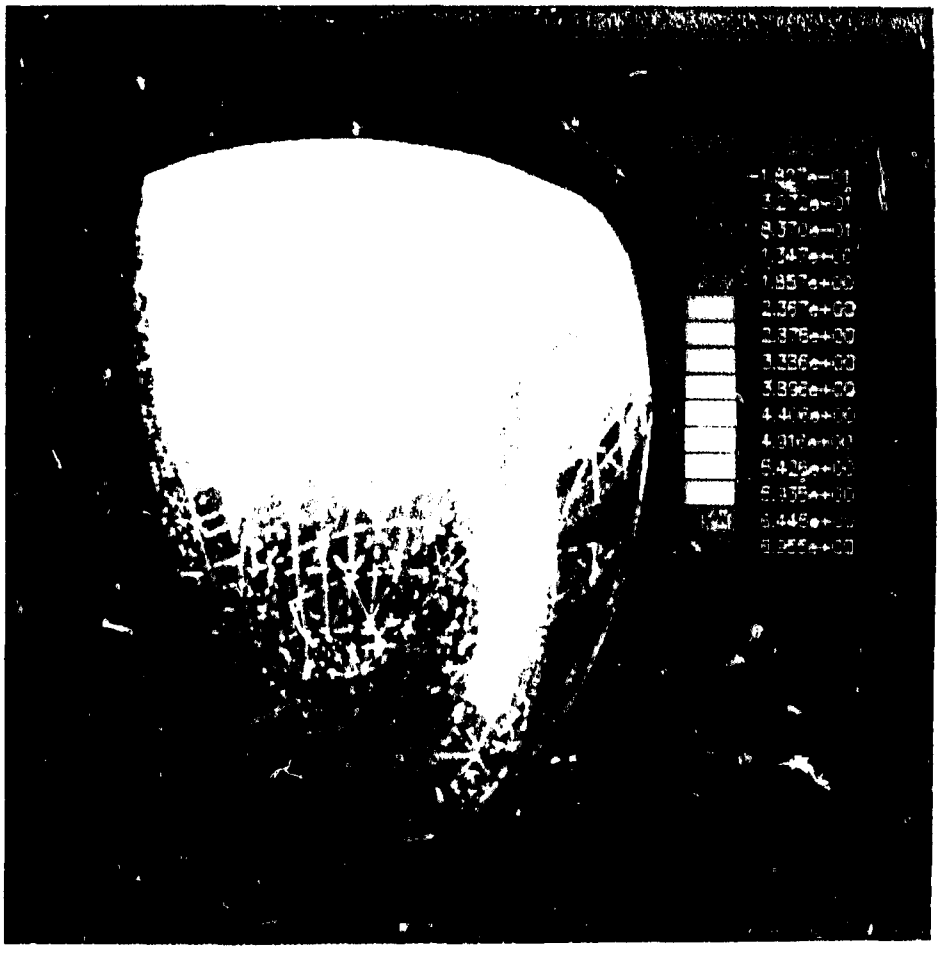

Figure 6.4: Predicted stress distribution σ_{zz}, and gross distortion of the human heart at +5 G_z. Stress levels are colour coded and given in kPa.

cle walls.

It is vital that computational models developed use reliable data for the mechanical properties of heart tissue. Unfortunately, most of the available data is limited to the normal ($+1G_z$) environment. That is, there is little data available on the properties of human myocardial tissue undergoing finite deformation. This evidently builds into the finite element model a measure of uncertainty. Alternatively, a heuristic approach would be to compute the deformed shape of the heart using projected material properties, and then compare these results with ultra-sound images and/or Doppler of the heart under high ($+G_z$) loading [11]. To bring about an optimum agreement between the ultra-sound images and the response of the computational model, the model properties may be readjusted. By using the outlined procedure, the possibility of myocardial damage due to excessive strains in the ventricles, caused by exposure to a combination of high $+G_z$ loading acting directly on the heart fibres and elevated hydrostatic pressures in the vasculative, may eventually be determined.

Chapter 7

Conclusions and Future Work

Conclusions

In this study, a computational model for the analysis of sustained $+G_z$ induced stress in the human left and right ventricle myocardium is presented. The finite element model is developed using the Galerkin weighted residual method with a *penalty* treatment of the incompressible behaviour of heart muscle. The model includes the effects of finite displacements, large strain, and incompressible material behaviour. Further, an exponential law for the strain energy density function is used to derive the incremental constitutive relation for passive myocardium and pericardium materials.

The results obtained demonstrate the ability of the non linear finite element model developed to provide quantitative data on the effects of moderate-to-high $+G_z$ acceleration on the cardiovascular system. Also, this approach offers a new perspective for the mechanical study of $+G_z$ acceleration on the human heart. The analysis provides predicted gross distortion with stress and strain data of the human heart under sustained exposure to $+G_z$ loading conditions. In conjunction with experimental data obtained using ultra sound

imaging techniques a greater understanding of the mechanism of $+G_z$ loads on the cardiovascular system should prove possible.

Suggested Future Work

- Validation of the finite element model by comparing predicted gross distortion profiles of the heart undergoing $+G_z$ loading with results obtained using ultra-sound imaging and/or Doppler measurements. In addition, the lack of any measurements associated with the internal ventricle cavity and surrounding body pressures under $+G_z$ loading conditions needs to be addressed. This would require the further study and measurement of the filling and expulsion of blood fluid from the ventricles under $+G_z$ loading conditions.

- Perform a dynamic simulation of the cardiac cycle (including the passive diastolic and active systolic phases) to study the effects of time dependency of $+G_z$ acceleration on the cardiovascular system. In addition, an alternative approach to the reduced-integration penalty technique when handling the incompressibility constraint would be to consider a *mixed* and/or *hybrid* finite element method [37, 79]. The mixed method has proven successful for problems with incompressible media, without the difficulties associated with a penalty parameter.

- Extend the hyperelastic constitutive relation to accommodate the anisotropic behaviour of the heart muscle. Further, it is evident that the proposed finite element analysis is limited, in part, by the available material data for cardiac tissue. There is, therefore, a need for further biaxial and triaxial testing of isolated human myocardium.

References

[1] Ahmad, S., Irons, B.M., and Zienkiewicz, O.C., *Analysis of thick and thin shell structures by curved finite elements*, Int. J. Numer. Meths. Engrg., (1970), 2:419-451.

[2] Bathe, K.J., *Finite Element Procedures in Engineering Analysis*, Prentice Hall, Inc., New Jersey, 1st ed., (1992).

[3] Bathe, K.J., and Bolourchi, S., *A geometric and material non-linear plate and shell element*, Comput. and Struct., (1980), 11:23-48.

[4] Blackwell, G.G, Cranney, G.B., and Pohost, G.M., *MRI: Cardiovascular System*, (1992), Gower Medical Publishing, New York.

[5] Burton, R.R., Meeker, L.J., and Raddin, J.H., *Centrifuges for studying the effects of sustained acceleration on human physiology*, IEEE, Engrg. Med. and Biol., (1991), March, pp. 56-65.

[6] Burton, R.R., and Whinnery, J.E., *Operational G-induced loss of consciousness: Something old; something new*, Aviation, Space and Environmental Med., (1985), 8:812-817.

[7] Chambost, G., and Turk, P., *G-induced loss of consciousness: Combat aircraft pilots head for trouble*, INTERAVIA, (1986), 5:507-508.

[8] Chen, C.J., Kwak, B.M., Rim, K., and Falsetti, M.L., *A model for an active left ventricle deformation-formulation of a non-linear quasi-steady finite-element analysis for orthotropic, three-dimensional myocardium*, Int. Conf. Finite Elements in Biomechanics, (1980), 2:639-655.

[9] Choi, H.S., and Vito, R.P., *Two-dimensional stress-strain relationship for canine pericardium*, Trans. ASME, J. Biomech. Engrg., (1990), 112:153-159.

[10] Clark, C., *Acceleration and body distortion*, Human Factors in Atypical Environments, Ch. 4, pp. 65-85.

[11] Danaher, C, *Air force evaluates acceleration effects on cardiac function - with HP ultrasound imaging system*, pp. 10-12.

[12] Demer L.L., and Yin, F.C.P., *Passive bi-axial mechanical properties in isolated canine myocardium*, J. Physiology, (1983), 339:615-630.

[13] Demiray, H., *Stresses in ventricular wall*, J. Appl. Mech., (1976), 14:194-197.

[14] Demiray, H., and Vito, R.P., *Large deformation analysis of soft biomaterials*, Int. J. Engrg. Sci., (1976), 14:789-793.

[15] Eiho, S., Matsumoto, N., Kuwahara, M., Matsuda, T., and Kawai, C., *3 D reconstruction and display of moving heart shapes from MRI data*, IEEE, Computers in Cardiology 1988, (1988), pp. 349-352.

[16] Eiho, S., Kuwahara, M., Shimura, K., Wada, M., Ohta, M., and Kozuka, T., *Reconstruction of the left ventricle from X-ray cineangiocardiograms*, Comput. in Cardiology, (1983), pp. 63-67.

[17] Erickson, H.H., Sandler, H., and Stone, H.L., *Cardiovascular function during sustained +G_z stress*, Aviation, Space, and Environmental Med., (1976), 7:750-756.

[18] Eringen, A.C., *Non-Linear Theory of Continuous Media*, McGraw-Hill, New York, (196), 1st ed..

[19] Frisch Fay, R., *Flexible Bars*, Butterworths & Co., London, (1962).

[20] Fung, Y.C., *Biomechanics: Mechanical Properties of Living Tissues*, (1981), Springer-Verlag Inc., New York.

[21] Fung, Y.C., *Biorheology of soft tissue*, (1973), Biorheology, 10:139-155.

[22] Ghista, D.N., and Hamid, M.S., *Finite-element stress analysis of the human left ventricle whose irregular shape is developed from single plane cineangiocardiogram*, Comput. Prog. Biomed. (1980), 7:219-231.

[23] Ghista, D.N., Roy, G., and Sahdler, H., *Cardiac assessment mechanics: Left ventricular mechno myocardiography, a new approach to the direction of diseased myocardial elements and states*, Med. Biol. Engrg. Comput., (1980), 18:271-280.

[24] Glatz, S.A, Misbach, G.A., Moores, W.Y., et al., *The pericardium substantially affects the left ventricle diastolic pressure-volume relationship in the dog*, Circulation. Res., (1978), 42:133-141.

[25] Gould, P., Ghista D., Brombolich, L., and Minsky, J., *In vivo stresses in the human left ventricular wall: analysis accounting for the irregular 3-D dimensional geometry and comparison with idealized geometry analysis*, J. Biomechanics, (1972), 5:521-539.

[26] Green, A.E., and Zerna, W., *Theortical Elasticity*, Oxford Press, London, 2^{nd} ed., (1968).

[27] Green, A.E., and Adkins, J.E., *Large Elastic Deformations and Nonlinear Continuum Mechanics*, Clarendon Press, Oxford, (1960).

[28] Guccione, J.M., and McCulloch, A.D., *Finite element modeling of ventricular mechanics*, eds. Glass, L., Hunter, P., and McCulloch, A., Theory of the Heart, Springer-Verlag, New York, (1990), pp. 121-143.

[29] Hammer, P.C., and Stroud, A.H., *Numerical integration of multiple integrals II*, Math. Tables Aids Comput., (1958), 12:272-280.

[30] Han, G., McPherson D.D., and Chandran K.B., *Finite element analysis of the effect of right ventricular ischemia on the left ventricular function*, ASME, 1989 Advances in Bioengineering, (1989), BED-15:37-138, (presented at the winter annual meeting of the ASME, San Francisco, Calif., Dec. 10-15, 1989).

[31] Heethaar, R.M., Pao, Y.C., and Ritman, E.L., *Computer Aspects of three-dimensional finite element analysis of stresses and strains in the intact heart*, Comput. and Biomed. Res., (1977), 10:271-285.

[32] Hess, O.M., *The role of the pericardium in interactions between cardiac chambers*, (1983), Amer. Heart J., 106:1377-1383.

[33] Hibbitt, H.D., Marcal, P.V., and Rice J.R., *A finite element formulation for problems of large strain and large displacements*, Int. J. Solids Struct., (1970), 6:1069-1086.

[34] Hill, R., *Aspects of Invariance in Solid Mechanics*, Adv. Appl. Mech., (1978), 18:1-75.

[35] Horowitz, A., Lanir, Y., Yin, F.C.P., Perl, M., Sheinman, I., and Strumpf, R.K., *Structural three-dimensional constitutive law for the passive myocardium*, Trans. ASME, J. Biomech. Engrg., (1988), 110:200-207.

[36] Horrigmoe, G., and Bergan, P.G., *Incremental variational principles and finite element models for non-linear problems*, Comput. Meths. Appl. Mech. Engrg., (1976), 7:201-217.

[37] Hughes, T.J.R., *The Finite Element Method*, Prentice Hall Inc., New Jersey, (1987).

[38] Hughes, T.J.R., and Liu, W.K., *Non-linear finite element shell formulation accounting for large membrane strains*, Comput. Meths. Appl. Mech. Engrg., (1983), 39:69-82.

[39] Hughes, T.J.R., and Conroy, E., *Non-linear finite element analysis of shells: Part I. Three-dimensional shells*, Comput. Meths. Appl. Mech. Engrg., (1981), 26:331-362.

[10] Hughes, T.J.R., and Pister, K.S. *Consistent linearization in mechanics of solids and structures*, Comput. and Struct., (1978), 8:391-397.

[11] Hughes, T.J.R., and Widget, J., *Finite rotation effects in numerical integration of rate constitutive equations arising in large-deformation analysis*, Int. J. Numer. Meths. Engrg., (1980), 15:1862-1867.

[12] Humphrey, J.D., Strumpf, R.K., and Yin, F.C.P., *Determination of a constitutive relation for passive myocardium: I A new functional form*, Trans ASME, J. Biomech. Engrg., (1990), 112:333-339.

[13] Humphrey, J.D., Strumpf, R.K., and Yin, F.C.P., *Determination of a constitutive relation for passive myocardium: II Parameter estimation*, Trans. ASME, J. Biomech. Engrg., (1990), 112:340-345.

[44] Humphrey, J.D., and Yin, F.C.P., *On constitutive relations and finite deformations of passive cardiac tissue: I. A pseudo-strain energy function*, Trans. ASME, J. Biomech. Engrg., (1987), 109:298-304.

[45] Hunter, P.J., McCulloch, A.D., Nielson, P.M.F., and Smaill, B.H., *A finite element model of passive ventricular mechanics*, eds. Spilker, R.L., and Simon, B.R., Computational Methods in Bioengineering, (1988), ASME, New York, pp. 387-397.

[46] Irons, B.M., and A. Razzaque, *Experience with the patch test for convergence of finite elements*, ed. Aziz A.K., Mathematical Foundations of the Finite Element Method, Academic Press., (1972), pp. 557-587.

[47] Irons, B.M., *Quadrature rules for brick based elements*, Int. J. Numer. Meths. Engrg., (1971), 3:293-294.

[48] Janz, R.F., Kubert B.R., Moriarty, T.F., and Grimm, A.F., *Deformation of the diastolic left ventricle - II. Nonlinear geometric effects*, J. Biomechanics, (1974), 7:509-516.

[49] Kernighan, B.W., and Ritchie, D.M., *The C programming language*, Prentice-Hall Inc., Englewood Cliffs, New Jersey, (1978).

[50] Kluber, M., *Incremental Finite Element Modelling in Non linear Solid Mechanics*, Ellis Horwood Ltd., 1st ed., (1989).

[51] Lee, M.C., Fung, Y.C., Shabetai, R., and Lewinter, M.M., *Biaxial mechanical properties of human pericardium and canine comparisons*, Amer. J. Physiology, (1987), 253:H75-82.

[52] Lee, M.C., LeWinter, M.M., Freeman, G.L., Shabetai, R., and Fung, Y.C., *Biaxial mechanical properties of the pericardium in normal and volume overload dogs*, Amer. J. Physiology, (1985), 249:222-230.

[53] Lee, J.M., and Bougher, D.R., *Tissue mechanics of canine pericardium in different test environments*, Circulation. Res., (1981), 19:533-541.

[54] Leverett, S.D., Jr., Burton, R.R., Crossley, R.J., Michaelson, E.D., and Shubrouks, S.J., Jr., *Human Physiologic Responses to High, Sustained +G$_z$ Acceleration*, (1973), USAFSAM-TR-73-21.

[55] Mackenzie, W.F. and Burton, R.R., *Ventricular pathology in swine at high sustained $+G_z$*, (1976), AGARD Conf. Proc. No. 189, The Pathophysiology of High Sustained $+G_z$ Acceleration.

[56] Mirsky, I., *Elastic properties of the myocardium: a quantitative approach with physiological and clinical applications*, eds. Berne R.M. et al., Handbook of Physiology The Cardiovascular System I, Amer. Physiological Soc., Maryland, (1979), 1:497-531.

[57] McMeeking R.M. and Rice, J.R., *Finite-element formulations for problems of large elastic-plastic deformations*, Int. J. Solids Struct., (1975), 11:601-615.

[58] Mooney, M., *A theory for large elastic deformation*, J. Applied Physics, (1940), 11:582-597.

[59] O'Bryon, J.F., *Unlocking G-LOC*, (AIAA), Aerospace Amer., Sept. issue, pp. 60-63.

[60] Oden, J.T., *Finite Elements of Nonlinear Continua*, McGraw-Hill, New York, (1972).

[61] Ogden R.W., *Non-linear Elastic Deformations*, Ellis Horwood Ltd., Fagland, (1984).

[62] Pao, Y.C., and Ritman, E.L., *Constitutive equation for excised ventricular wall strips*, (1991), ASME, 1991 Biomechanics Symposium, AMD-Vol 120, pp. 271-274.

[63] Pao Y.C., Natarajan, G.K., Padiyar, R., and Ritman, E.L., *Derivation of myocardial fiber stiffness equation based on theory of laminated composite*, Trans. ASME, J. Biomech. Engrg., (1980), 102:252-257.

[64] Pao, Y.C., Robb, R.A., and Ritman, E.L., *Plain-strain finite element analysis of reconstructed diastolic left ventricular cross section*, Ann. Biomed. Engrg., (1976), 4:232-249.

[65] Pao, Y.C., Ritman, E.L., and Wood, E.M., *Finite-element analysis of left ventricular myocardial stresses*, J. Biomechanics, (1974), 7:469-477.

[66] Parmley, W.W., Talbot, L., *Heart as a pump*, eds. Berne R.M. et al., Handbook of Physiology The Cardiovascular System I, Amer. Physiological Soc., Maryland, (1979), 1:497-531.

[67] Perl, M., and Horowitz, A., *Material and structural limitations in a 3D finite element model of the left ventricle*, ed. Sideman, S., Simulation and Imaging of the Cardiac System, (1985), pp. 117-129.

[68] Pinsky, P.M., Oritz, M., and Pister, K.S., *Numerical integration of rate constitutive equations in finite deformation analysis*, Comput. Meths. Appl. Mech. Engrg., (1983), 40:137-158.

[69] Pinto, J.G., and Fung, Y.C., *Mechanical properties of the heart muscle in the passive state*, J. Biomechanics, (1973), 6:597-616.

[70] Rabkin, S.W, and Hsu, P.H., *Mathematical and mechanical modeling of stress-strain relationship of pericardium*, Amer. J. Physiology, (1975), 299:896-900.

[71] Rankin, J.S., Arentzen, C.E, McHale P.A, Ling, D, and Anderson, R.W. *Viscoelastic properties of the diastolic left ventricle in the conscious dog*, Circulation. Res., (1977), 41:37-45.

[72] Ray, G., and Ghista, D.N., *In vivo properties of normal and ischemic infarcted myocardium*, , (1979), Proc. 7th Canadian Congress of Applied Mechanics, Sherbrooke, pp. 819-820.

[73] Ramm, E., *The Riks/Wempner approach - An extension of the displacement control method in nonlinear analyses*, eds. Hinton, E., Owen, D.R.J., and Taylor, C., Recent Advances in Non Linear Computational Mechanics, (1982), Pineridge Press Ltd., Swansea, U.K., Ch. 3, pp. 63-86

[74] Riks, E., *An incremental approach to the solution of snapping and buckling problems*, Int. J. Solids Struct., (1979), 15:529-551.

[75] Riks, E., *The application of Newton's method to the problem of elastic instability*, J. Appl. Mech., (1972), 39:1060-1066.

[76] Ritman, E.L., Kursey, J.H., Robb, R.A., Gilbert, B.K., Haris, L.D., and Wood, E.H., *Three dimensional imaging of heart, lung, and circulation*, Science, (1980), 210:273-280.

[77] Rivlin, R.S., *Large elastic deformations of isotropic materials: IV: Further results in the theory of torsion, shear and flexure*, Philos. Trans. Roy. Soc. London, Series A, (1949), 242:173-195.

[78] Rivlin, R.S., *Large elastic deformations of isotropic materials: IV: Further developments of the general theory*, Philos. Trans. Roy. Soc. London, Series A, (1948), 241:379-397.

[79] Saleeb, A.F., Chang, T.Y., Graf, W., and Yeunyong, Y., *A hybrid/mixed model for nonlinear shell analysis and its applications to large rotation problems*, Int. J. Numer. Meths. Engrg., (1990), 79:21-70.

[80] Saggawa, K., *The heart as a pump*, eds. Brown, J.H.U., and Gann, D.S., Engineering Principles in Physiology, (1973), 2:101-126.

[81] Simo, J.C., Fox, D.D., and Rifai, M.S., *On a stress resultant geometrically exact shell model. Part III: Computational aspects of the nonlinear theory*, Comput. Meths. Appl. Mech. Engrg., (1990), 79:21-70.

[82] Skorton, D.J., Chandran, K.B., Collins, S.M., Petree, L.P., McPherson, D.D., Olshansky, B., Noel, M.P., and Kerber, R.E., *Three-dimensional ultrasonic cardiac reconstruction: general aspects and application to finite element analysis of the left ventricle*, ed. Sideman, S., Simulation and Imaging of the Cardiac System, (1985), pp. 135-189.

[83] Smaill, B., Hunter, P., *Structure and function of the diastolic heart: Material properties of passive myocardium*, eds. Glass, L., Hunter, P., and McCulloch, A., Theory of the Heart, Springer-Verlag, New York, (1990), pp. 1-30.

[84] Smith, I.M., and Kidger, D.J., *Properties of the 20-node brick*, Int. J. Numer. Analy. Meths. in Geomechanics, (1991), 15:871-891.

[85] Sonnenblick, E.H., Braunwald, E., and Morrow, A.G., *The contractile properties of human heart muscle: Studies on myocardial mechanics of surgically excised papillary muscles*, J. of Clinical Investigations, (1965), 44:966-976.

[86] Stanley, G.M., Park, K.C., and Hughes, T.J.R., *Continuum based resultant shell elements*, eds. Hughes, T.J.R. and Hinton, E., In Finite Elements for Plate and Shell Structures, (1985), 1:1-45.

[87] Stone, H.L., Sordahl, L.A., Dowell, R.T., Lindsey, J.W., and Erickson, M.M., *Coronary Flow and Myocardial Biochemical Responses to High Sustained $+G_z$ Acceleration*, (1976), AGARD Conf. Proc. No. 189, The Pathophysiology of High Sustained $+G_z$ Acceleration.

[88] Streeter, D.D. Jr., *Gross morphology and fibre geometry of the heart*, ed. Berne R.M. et al., Handbook of Physiology – The Cardiovascular System I, Amer. Physiological Soc., Maryland, (1979), 1:61-112.

[89] Sun Microsystems, *SunPHIGS: Programmer's Hierarchical Interactive Graphics System – Programmer's reference manual*, Sun Microsystems, Mountain View, CA, (1989).

[90] Surana, K.S., *Geometrically nonlinear formulations for the curved shell elements*, Int. J. Numer. Meths. Engrg., (1983), 19:581-615.

[91] Taber, C.W., *Taber's Cyclopedic Medical Dictionary*, ed. Clayton, L.T., F.A. Davis Co., Philadelphia, 15^{th} ed., (1985).

[92] Taylor, R.L., Simo, J.C., Zienkiewicz, O.C., and Chan, A.C.H., *The Patch Test - A condition for assessing FEM convergence*, Int. J. Numer. Meths. Engrg., (1986), 22:39-62.

[93] Timoshenko, S.P., and Woinowsky-Krieger, S., *Theory of Plates and Shells*, McGraw-Hill, London, 2^{nd} ed., (1970).

[94] Truesdell, C.A., and Noll, W., *The non-linear field theories of mechanics*, ed. Flügge, S., Handbuch der Physik, III, Springer, Berlin, (1965).

[95] Vito, R.P., *The role of the pericardium in cardiac mechanics*, J. Biomechanics, (1979), 12:587-592.

[96] Wempner, G.A., *Discrete approximations related to nonlinear theories of solids*, Int. J. Solids Struct., (1971), 7:1581-1599.

[97] Wood, E.H., *Prevention of the pathophysiologic effects of acceleration in humans: Fundamentals and Historical perspectives*, IEEE, Engrg. Med. and Biol., (1991), March, pp. 56-65.

[98] Yettram, A.L., Vinson, C.A., and Gibson, D.G., *Effect of myocardial fiber architecture on the behaviour of the human left ventricle in diastole*, Trans. ASME, J. Biomech. Engrg., (1983), 5:321-328.

[99] Yin, F.C.P., Strumpf, R.K., Chew, P.H., and Zeger, S.L., *Quantification of the mechanical properties of noncontracting canine myocardium under simultaneous biaxial loading*, J. Biomechanics, (1987), 20:577-589.

[100] Yin, F.C.P., *Applications of the finite-element method to ventricular mechanics*, Critical Reviews in Biomedical Engrg., (1985), 12:311-342.

[101] Zienkiewicz, O.C., Taylor R.L., and Too, J.M., *Reduced integration techniques in general analysis of plates and shells*, Int. J. Numer. Metlns. Engrg., (1971), 3:275-290.

Appendix A

Linearization Theory

The following is a review of the linearization theory for a scalar function using Taylor's formula in Euclidean space.

Consider the mapping $f : \Re^3 \rightarrow \Re^1$. Assuming f to be differentiable at a point $\hat{\mathbf{x}}$, one may expand f as a Talyor's series

$$f(\hat{\mathbf{x}} + \mathbf{u}) = f(\hat{\mathbf{x}}) + Df(\hat{\mathbf{x}}) \cdot \mathbf{u} + o(\|\mathbf{u}\|_2) \tag{A.1}$$

where $\mathbf{u}$ is an arbitrary vector in $\Re^3$. In Euclidean space, $\mathbf{u}$ denotes a vector emanating from the point $\hat{\mathbf{x}}$ in $\Re^3$, and Df is the gradient vector given by

$$Df(\hat{\mathbf{x}}) \cdot \mathbf{u} = \frac{d}{d\epsilon} f(\hat{\mathbf{x}} + \epsilon \mathbf{u})|_{\epsilon=0} \tag{A.2}$$

where ϵ is a scalar parameter. If $\mathbf{u}$ is a unit vector, then $Df(\hat{\mathbf{x}}) \cdot \mathbf{u}$ is sometimes called the *directional derivative* of f. Alternatively, $Df \cdot \mathbf{u}$ can be expressed in terms of the *scalar* differential operator, denoted by $\mathrm{G}_{\mathbf{u}} = \mathbf{u} \cdot \nabla_x$, as $\mathrm{G}_{\mathbf{u}} f(\hat{\mathbf{x}})$.

In the context of linearization, the first order linear approximation of f in the neighborhood of $\hat{\mathbf{x}}$ can be written as

$$L[f, \mathbf{u}]_{\hat{\mathbf{x}}} = f(\hat{\mathbf{x}}) + Df(\hat{\mathbf{x}}) \cdot \mathbf{u} \tag{A.3}$$

provided $\|\mathbf{u}\|_2^2 = \mathbf{u} \cdot \mathbf{u}$ is sufficiently small.

Appendix B

Element Matrices

B.1 Introduction

This section details the development of the elemental stiffness, geometric matrices and load vector used in the construction of the finite element system of equations. In the finite element analysis of $+G_z$ induced stresses in the human heart, two different three dimensional continuum based elements are employed. One is a twenty node isoparametric solid element, used to describe the non-linear geometric and material behaviour of the left and right ventricle myocardium. The other, a degenerate isoparametric shell element capable of finite membrane strains, is used to model the surrounding protective pericardial sac.

Numerical integration for the element is performed using $(r \times s \times t)$ Gaussian – Legendre quadrature, as follows

$$\int_{-1}^{1}\int_{-1}^{1}\int_{-1}^{1} f(\xi,\eta,\zeta)d\xi d\eta d\zeta \quad \cong \quad \sum_{i=1}^{r}\sum_{j=1}^{s}\sum_{k=1}^{t} w_i w_j w_k f(\xi_i,\eta_j,\zeta_k), \quad \text{(B.1)}$$

where (w_i, w_j, w_k) is the integration weight for the corresponding Gauss point location (ξ_i, η_j, ζ_k). (The adopted integration technique is *exact* for polynomials, $p(x)$, of order $\leq (2n-1)$, where n is the number of Gauss points [47].)

In particular integration is carried out using either reduced (2x2x2) or selective (3x3x2) Gaussian quadrature (RI). However, for *exact* or full integration (FI), (3x3x3) is required for a straight sided parallelepiped and (4x4x4) for a general curved sided isoparametric (quadratic) type solid element. Although RI is less accurate than FI, the error incurred is considered relatively small. In general, the drawbacks associated with RI are usually outweighed by the computational savings and improved element performance [101].

B.2 A 3–D Isoparametric Solid Element

B.2.1 Introduction

In this study, the left and right human ventricles are discretized using 20–node isoparametric solid elements [2, 37]. The ability of the element to model curved boundaries, non-linear material and geometric behaviour is ideal for the problem considered (see Figure B.1). The idiosyncrasies of this element are discussed in detail in [84]. When a numerical integration is performed over the element to obtain the finite element stiffness and geometric matrices, both reduced and full integration techniques can be used. However, for cases involving incompressible materials, such as rubber and biological tissue, integration of the matrices is performed with a reduced Gaussian quadrature rule.

B.2.2 Geometry / Kinematic Description

Let the parent domain be denoted by the bi-unit cube $\square$, defined by

$$\square : \{(\xi, \eta, \zeta) \in [-1, 1] \times [-1, 1] \times [-1, 1]\}. \tag{B.2}$$

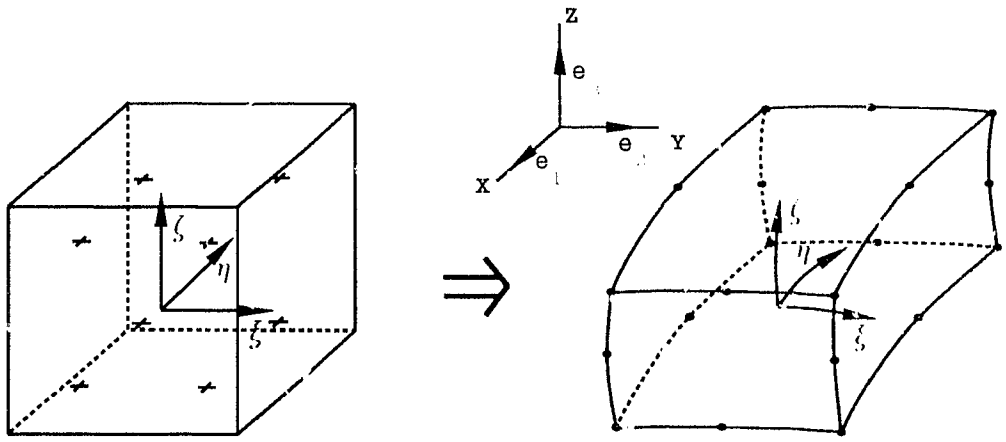

Figure B.1: A three-dimensional solid element showing the bi unit cube (ξ, η, ζ) mapping into the physical (x, y, z) domain.

For an isoparametric transformation, one can define

$$\mathbf{x}^e : \square \rightarrow \Re^3 \qquad \mathbf{u}^e : \square \rightarrow \Re^3, \tag{B.3}$$

where $\mathbf{x} = \{x, y, z\}$ and $\mathbf{u} = \{u, v, w\}$. Introducing the basis function approximation, then

$$\mathbf{x}^e = \sum_{I=1}^{n_{en}} N_I(\xi, \eta, \zeta)\hat{\mathbf{x}}_I^e(t), \qquad \text{and} \qquad \mathbf{u}^e = \sum_{I=1}^{n_{en}} N_I(\xi, \eta, \zeta)\hat{\mathbf{u}}_I^e(t), \tag{B.4}$$

where $\hat{\mathbf{x}}_I^e \in \Re^3$ and $\hat{\mathbf{u}}_I^e \in \Re^3$ for $n_{en} = 20$. The standard quadratic isoparametric basis functions, $N_I(\xi, \eta, \zeta)$, at the corner nodes are

$$N_I(\xi, \eta, \zeta) = 1/8(1 + \xi_I\xi)(1 + \eta_I\eta)(1 + \zeta_I\zeta)(\xi_I\xi + \eta_I\eta + \zeta_I\zeta - 2) \qquad \text{for} \quad I = 1, 2, \ldots, 8,$$

and at the midside nodes

$$\begin{aligned} N_I(\xi, \eta, \zeta) &= 1/4(1 - \xi^2)(1 + \eta_I\eta)(1 + \zeta_I\zeta) \qquad \text{for} \quad I = 9, 11, 13, 15, \\ N_I(\xi, \eta, \zeta) &= 1/4(1 + \xi_I\xi)(1 - \eta^2)(1 + \zeta_I\zeta) \qquad \text{for} \quad I = 10, 12, 14, 16, \\ N_I(\xi, \eta, \zeta) &= 1/4(1 + \xi_I\xi)(1 + \eta_I\eta)(1 - \zeta^2) \qquad \text{for} \quad I = 17, 18, 19, 20, \end{aligned}$$

where $(\xi_I, \eta_I, \zeta_I = \pm 1)$.

B.2.3 Finite Element Matrices

Strain-Displacement Matrices: $\underset{\sim}{\mathbf{B}}_L$ and $\underset{\sim}{\mathbf{B}}_{NL}$

The matrix representation of the linear strain tensor is given by

$$\Delta \underset{\sim}{\boldsymbol{\varepsilon}} = \begin{Bmatrix} \Delta\varepsilon_{11} \\ \Delta\varepsilon_{22} \\ \Delta\varepsilon_{33} \\ 2\,\Delta\varepsilon_{12} \\ 2\,\Delta\varepsilon_{23} \\ 2\,\Delta\varepsilon_{31} \end{Bmatrix} = \begin{Bmatrix} u_{,x} \\ v_{,y} \\ w_{,z} \\ u_{,y} + v_{,x} \\ v_{,z} + w_{,y} \\ u_{,w} + w_{,x} \end{Bmatrix}.$$

Further, the derivatives of the displacement field with respect to the coordinates in matrix form is given by

$$\begin{bmatrix} u_{,x} & v_{,x} & w_{,x} \\ u_{,y} & v_{,y} & w_{,y} \\ u_{,z} & v_{,z} & w_{,z} \end{bmatrix} = \underset{\sim}{\mathbf{J}}^{-1} \begin{bmatrix} u_{,\xi} & v_{,\xi} & w_{,\xi} \\ u_{,\eta} & v_{,\eta} & w_{,\eta} \\ u_{,\zeta} & v_{,\zeta} & w_{,\zeta} \end{bmatrix}, \tag{B.5}$$

where the Jacobian of transformation matrix is defined by

$$\underset{\sim}{\mathbf{J}} = \begin{bmatrix} x_{,\xi} & y_{,\xi} & z_{,\xi} \\ x_{,\eta} & y_{,\eta} & z_{,\eta} \\ x_{,\zeta} & y_{,\zeta} & z_{,\zeta} \end{bmatrix},$$

and the determinant of $\underset{\sim}{\mathbf{J}}$ is denoted by J. Adopting the elemental basis functions to approximate the linear strain increment in terms of the nodal displacements yields

$$\Delta \underset{\sim}{\boldsymbol{\varepsilon}} = \sum_{I=1}^{n_{en}} \underset{\sim}{\mathbf{B}}_I \, \underset{\sim}{\hat{\mathbf{u}}}^e_I, \tag{B.6}$$

where $\underset{\sim}{\hat{\mathbf{u}}}^e \in \Re^{n\times 1}$ with $n = n_{en} \cdot n_{dof}$, is of the form

$$\underset{\sim}{\hat{\mathbf{u}}}^e = \{\hat{\mathbf{u}}^e_k\} = \{(\hat{u}, \hat{v}, \hat{w})_1 | (\hat{u}, \hat{v}, \hat{w})_2 | \ldots | (\hat{u}, \hat{v}, \hat{w})_{n_{en}}\}^T, \tag{B.7}$$

with $(\hat{u}, \hat{v}, \hat{w})_I$ denoting the incremental nodal displacement in the corresponding (x, y, z) direction at node I. For the solid element, the number of nodes per element, $n_{en} = 20$, and degrees of freedom per node, $n_{dof} = 3$, gives $n = 60$. The linear strain-displacement transformation matrix, $\underset{\sim}{\mathbf{B}}_L \in \Re^{6\times n}$, is defined by

$$\underset{\sim}{\mathbf{B}}_L = \left[\begin{array}{c|ccc|c} & b^I_{u,x} & 0 & 0 & \\ & 0 & b^I_{u,y} & 0 & \\ & 0 & 0 & b^I_{u,z} & \\ \cdots & b^I_{u,y} & b^I_{u,x} & 0 & \cdots \\ & 0 & b^I_{u,z} & b^I_{u,y} & \\ & b^I_{u,w} & 0 & b^I_{u,x} & \end{array}\right]_I,$$

where

$$b^I_{u,x_i} = J^{-1}_{i1} N_{I,\xi} + J^{-1}_{i2} N_{I,\eta} + J^{-1}_{i3} N_{I,\zeta} \quad \text{with} \quad x_i \in \{x, y, z\},$$

for $I = 1, 2, \ldots, n_{en}$.

Next, consider the non-linear strain-displacement transformation matrix for the solid element. Then, rewriting the derivatives of the displacement field given in (B.5) in vector form as

$$\left[\begin{array}{c} u_{,x} \\ v_{,x} \\ w_{,x} \\ \hline u_{,y} \\ v_{,y} \\ w_{,y} \\ \hline u_{,z} \\ v_{,z} \\ w_{,z} \end{array}\right] = \left[\begin{array}{c|c|c} & b^I_{u,x}\,\underset{\sim}{\mathbf{I}} & \\ \hline & & \\ \cdots & b^I_{u,y}\,\underset{\sim}{\mathbf{I}} & \cdots \\ \hline & & \\ & b^I_{u,z}\,\underset{\sim}{\mathbf{I}} & \end{array}\right]_I \left\{\begin{array}{c} \vdots \\ \hline \hat{u}_I \\ \hat{v}_I \\ \hat{w}_I \\ \hline \vdots \end{array}\right\} = \underset{\sim}{\mathbf{B}}_{NL}\,\hat{\mathbf{u}}^e,$$

where $\underset{\sim}{\mathbf{B}}_{NL} \in \Re^{9\times n}$, b^I_{u,x_i} as previously defined, and $\underset{\sim}{\mathbf{I}}$ is the (3x3) identity matrix.

Material Stiffness Matrix: $\underset{\sim}{\mathbf{K}}^e_l$

With $\underset{\sim}{\mathbf{B}}_L$ defined in section (B.2.3) the element material stiffness matrix of equation (3.10) becomes

$$\underset{\sim}{\mathbf{K}}^e_l = \underbrace{[\mathbf{K}^e_{ab}]}_{60\times 60} = \int_{\square} \underset{\sim}{\mathbf{B}}^T_L \, [\underset{\sim}{\mathcal{L}}] \, \underset{\sim}{\mathbf{B}}_L \, Jd[\square]. \tag{B.8}$$

Geometric Stiffness Matrix: $\underset{\sim}{\mathbf{K}}^e_{nl}$

The elemental geometric stiffness matrix of (3.10) expressed in terms of $\underset{\sim}{\mathbf{B}}_{NL}$ is given as follows

$$\underset{\sim}{\mathbf{K}}^e_{nl} = \underbrace{[\mathbf{K}^e_{ab}]}_{60\times 60} = \int_{\square} \underset{\sim}{\mathbf{B}}_{NL}{}^T [\underset{\sim}{\boldsymbol{\sigma}}] \underset{\sim}{\mathbf{B}}_{NL} \, Jd[\square]. \tag{B.9}$$

Then, the stress matrix, $[\boldsymbol{\sigma}]$, in (3.10) has the form of a (9x9) matrix as

$$[\underset{\sim}{\boldsymbol{\sigma}}] = \begin{bmatrix} \sigma_{11}\,\underset{\sim}{\mathbf{I}} & \sigma_{12}\,\underset{\sim}{\mathbf{I}} & \sigma_{13}\,\underset{\sim}{\mathbf{I}} \\ & \sigma_{22}\,\underset{\sim}{\mathbf{I}} & \sigma_{23}\,\underset{\sim}{\mathbf{I}} \\ \textit{Sym.} & & \sigma_{33}\,\underset{\sim}{\mathbf{I}} \end{bmatrix}.$$

B.2.4 External Force Vector

Consider the external force vector to consist of the net contributions of the body and surface forces, then

$$\underset{\sim}{\mathbf{F}}^{e(ext)} = \underset{\sim}{\mathbf{f}}^e_{body} + \underset{\sim}{\mathbf{f}}^e_{surf}. \tag{B.10}$$

Body force

The element body force vector for the three-dimensional continuum based element is given by

$$\underset{\sim}{\mathbf{f}}^{e}_{body} = \underbrace{\{\mathbf{f}^{e}_{a}\}^{body}}_{60\times 1} = \int_{\square} \rho \, \underset{\sim}{\mathbf{N}}^{T} \underset{\sim}{\mathbf{b}} \, J d\square, \tag{B.11}$$

where $\underset{\sim}{\mathbf{b}} = \{b_x, b_y, b_z\}^T$ are the components of the acceleration vector. In addition, $\underset{\sim}{\mathbf{N}}$ is a matrix of basis functions of the form

$$\underset{\sim}{\mathbf{N}} = \left[\cdots \left| \, N_I \, \underset{\sim}{\mathbf{I}} \, \right|_I \cdots \right], \tag{B.12}$$

for $I = 1, 2, \ldots, n_{en}$.

Surface Force

The element surface force vector for the three-dimensional continuum based element is given by

$$\underset{\sim}{\mathbf{f}}^{e}_{surf} = \underbrace{\{\mathbf{f}^{e}_{a}\}^{surf}}_{30\times 1} = \int_{\square} \underset{\sim}{\mathbf{N}}^{T} \underset{\sim}{\mathbf{h}}_{s} \, J_s \, d\square, \tag{B.13}$$

where J_s is the determinant of the surface Jacobian matrix and $\underset{\sim}{\mathbf{h}}_{s}$ is the surface load vector (per unit area in the current reference configuration). Also, $\underset{\sim}{\mathbf{N}}$ is the matrix of basis functions as defined above. The subscript s refers to the bi-unit cube face for which the applied load corresponds (ie., $\xi = \pm 1$, $\eta = \pm 1$, or $\zeta = \pm 1$). The determinant of the surface Jacobian matrix, J_s, is defined as

$$J_s = \begin{cases} \|\mathbf{x}_{,\eta} \times \mathbf{x}_{,\zeta}\|_2 & \text{if} \quad \xi = \pm 1 \\ \|\mathbf{x}_{,\zeta} \times \mathbf{x}_{,\xi}\|_2 & \text{if} \quad \eta = \pm 1 \\ \|\mathbf{x}_{,\xi} \times \mathbf{x}_{,\eta}\|_2 & \text{if} \quad \zeta = \pm 1 \end{cases},$$

where $\| \cdot \|_2$ denotes the Euclidean norm.

Surface Pressure

For the case when a surface is subjected to a pressure load, the surface load vector, $\mathbf{h}_s$, becomes

$$\underset{\sim}{\mathbf{h}}_s = -p\,\underset{\sim}{\mathbf{n}},$$

where p is the external pressure exerted on a face in the current reference configuration. Further, the corresponding outward unit normal, $\underset{\sim}{\mathbf{n}}$, is given by

$$\underset{\sim}{\mathbf{n}} = \begin{cases} \pm(\boldsymbol{e}_\eta \times \boldsymbol{e}_\zeta) \,/\, \|\boldsymbol{e}_\eta \times \boldsymbol{e}_\zeta\|_2 & \text{if} \quad \xi = \pm 1 \\ \pm(\boldsymbol{e}_\zeta \times \boldsymbol{e}_\xi) \,/\, \|\boldsymbol{e}_\zeta \times \boldsymbol{e}_\xi\|_2 & \text{if} \quad \eta = \pm 1 \\ \pm(\boldsymbol{e}_\xi \times \boldsymbol{e}_\eta) \,/\, \|\boldsymbol{e}_\xi \times \boldsymbol{e}_\eta\|_2 & \text{if} \quad \zeta = \pm 1 \end{cases},$$

where (ξ, η, ζ) denote the orthogonal unit bases of the curvilinear system.

B.3 A 3–D Continuum Based Shell Element

B.3.1 Introduction

Original development of a linear 3D degenerate solid element to model doubly curved shells is credited to Ahmad et al. [1]. Extension to the non linear regime, where both geometric and material nonlinearities are accounted for, has generated considerable interest and attention ever since (for example, [3, 38, 79, 81, 86, 90]).

The 3D degenerate solid element used in the analysis is a non linear C^0 type shell model which accounts for large membrane strains. These nonlinearities include both material (eg. hyperelastic) and geometric (finite displacements / rotations) effects. The element displacement field is expressed

in terms of three global displacements (u, v, w) and two local rotations (θ_1, θ_2) (see Figure B.2). However, the inclusion of finite rotations introduces additional complexity since, unlike displacements, rotations can not simply be added vectorially. In fact, rotational increments are non-commutative and therefore require special attention.

B.3.2 Geometry / Kinematic Description

Shell Assumptions

The underlying assumptions associated with the statement of geometric and kinematic descriptions of the (degenerate) shell element are:

(i). The *fibres* in the thickness direction are straight and inextensible.

(ii). Stresses associated with the thickness direction are zero.

(iii). The transverse shear strains are assumed *small* (ie. no drilling degrees of freedom are present).

The assumptions given in (i) and (ii) are consistent with the classical Mindlin / Reissner shear flexibility theory for plates [93]. Further, assumption (i) seems to imply that any change in the shell thickness is not permitted, however, a computationally incremental update procedure enables large membrane strains to be accounted for [39]. Also, assumption (iii) does not exclude the modelling of large membrane behaviour in the element formulation.

Before proceeding, it is useful to define some common terminology associated with the degenerate shell type formulation. Consider the parent element

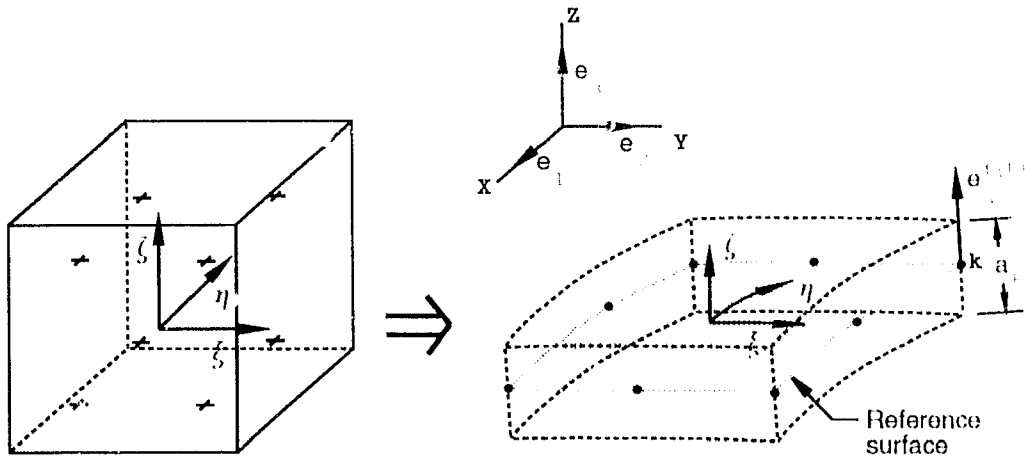

(a)

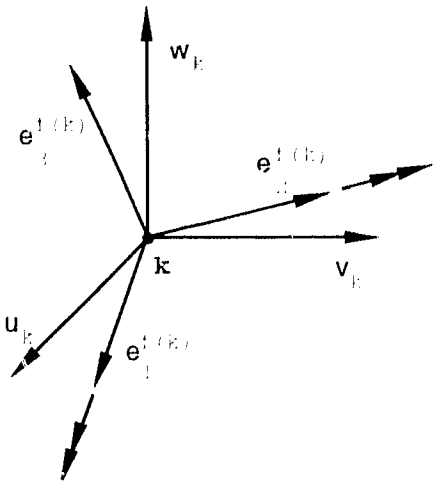

(b)

Figure B.2: (a) A three-dimensional degenerate shell element showing the bi-unit cube (ξ, η, ζ) mapping into the physical (x, y, z) domain. (b) Relationship between shell orientation and global coordinate system (at node k).

domain given by the bi-unit cube

$$\square : \{(\xi, \eta, \zeta) \in [-1, 1] \times [-1, 1] \times [-1, 1]\},$$

which is mapped into the physical shell domain, see Figure B2. The surface (ξ, η) for a fixed ζ is called the *lamina*. For the special case when $\zeta = 0$, the element *mid-surface* is given. Further, the shell element thickness is given by constructing a position vector emanating from the mid-surface. This vector is called the *fibre* direction (or sometimes is referred to as the *pseudo-normal* vector), and is not in general perpendicular to the lamina. The above definition of a pseudo-normal vector ensures that the intersection of shell elements contains no gaps or overlaps.

Shell Coordinate Systems

There are three distinct Cartesian coordinate systems adopted for the shell element, namely,

(i). Global system – is the fixed Cartesian reference system common to all elements defined at $t = 0$, with orthonormal basis $(\boldsymbol{e}_1, \boldsymbol{e}_2, \boldsymbol{e}_3)$.

(ii). Nodal fibre system – is a coordinate system constructed using the fibre direction base vector, $\boldsymbol{e}_3^{f(I)}$, given at each node I. The orthonormal bases for the I^{th} node are defined by $(\boldsymbol{e}_1^{f(I)}, \boldsymbol{e}_2^{f(I)}, \boldsymbol{e}_3^{f(I)})$, see Figure B2. The transformation between the global and nodal fibre coordinate system is given by

$$\mathbf{T}^{fg} : \boldsymbol{e}^f \rightarrow \boldsymbol{e}^g.$$

(iii). Lamina system – is a *local* coordinate system constructed at each integration point with orthonormal basis $(\boldsymbol{e}_1^l, \boldsymbol{e}_2^l, \boldsymbol{e}_3^l)$, where $\boldsymbol{e}_1^l$ and $\boldsymbol{e}_2^l$ are

taken locally tangent to the curvilinear lamina surface of the physical shell (which corresponds to the (ξ, η) plane in the global coordinate system). Further, $\boldsymbol{e}_3^l$ is taken normal to the lamina surface, such that

$$\boldsymbol{e}_3^l = (\boldsymbol{e}_\xi \times \boldsymbol{e}_\eta) \,/\, \|\boldsymbol{e}_\xi \times \boldsymbol{e}_\eta\|_2,$$

where $\boldsymbol{e}_\xi = \mathbf{x}_{,\xi} \,/\, \|\mathbf{x}_{,\xi}\|_2$, and $\boldsymbol{e}_\eta = \mathbf{x}_{,\eta} \,/\, \|\mathbf{x}_{,\eta}\|_2$. Also, the definition of $\boldsymbol{e}_3^l$ is used later to invoke the plane stress condition given in assumption (ii). It is evident that $(\boldsymbol{e}_\xi, \boldsymbol{e}_\eta)$ are not necessarily orthogonal, therefore, in order to construct a unique orthonormal lamina basis, $(\boldsymbol{e}_1^l, \boldsymbol{e}_2^l)$ are chosen to be as *close* as possible to $(\boldsymbol{e}_\xi, \boldsymbol{e}_\eta)$ respectively, as follows [39]

$$\begin{aligned} \boldsymbol{e}_1^l &= (\boldsymbol{e}_\alpha - \boldsymbol{e}_\beta) \,/\, \|\boldsymbol{e}_\alpha - \boldsymbol{e}_\beta\|_2 , \\ \boldsymbol{e}_2^l &= (\boldsymbol{e}_\alpha + \boldsymbol{e}_\beta) \,/\, \|\boldsymbol{e}_\alpha + \boldsymbol{e}_\beta\|_2 . \end{aligned}$$

where $\boldsymbol{e}_\alpha$ and $\boldsymbol{e}_\beta$ are defined as

$$\begin{aligned} \boldsymbol{e}_\alpha &= (\boldsymbol{e}_\xi + \boldsymbol{e}_\eta) \,/\, \|\boldsymbol{e}_\xi + \boldsymbol{e}_\eta\|_2 , \\ \boldsymbol{e}_\beta &= (\boldsymbol{e}_3^l \times \boldsymbol{e}_\alpha) \,/\, \|\boldsymbol{e}_3^l \times \boldsymbol{e}_\alpha\|_2 . \end{aligned}$$

Transformation of vector/tensor quantities from the global, g, to local, l, coordinate system is performed using the orthogonal preserving transformation,

$$\mathbf{T}^{gl} : \boldsymbol{e}^g \rightarrow \boldsymbol{e}^l. \tag{B.14}$$

Geometry

Consider the quadratic shell element with the reference surface taken at mid surface (ie. $\zeta = 0$). Then, mapping the bi-unit square into the mid surface

of the physical domain as follows

$$\mathcal{S} = \left\{ \phi : \square_s \rightarrow \Re^3 \;\middle|\; \phi\big|_{\Omega^e} = \sum_{I=1}^{n_{en}} N_I(\xi,\eta)\hat{\beta}_I \right\},$$

where the bi-unit square is given by

$$\square_s : \{(\xi,\eta) \in [-1,1] \times [-1,1]\}.$$

The standard quadratic isoparametric basis functions, $N_I(\xi,\eta)$, are defined at the corner nodes as

$$N_I(\xi,\eta) = 1/4(1+\xi_I\xi)(1+\eta_I\eta)(\xi_I\xi+\eta_I\eta-1) \qquad \text{for} \quad I = 1,2,\ldots,4,$$

and at the midside nodes as

$$N_I(\xi,\eta) = 1/2(1-\xi^2)(1+\eta_I\eta) \qquad \text{for} \quad I = 5,6,$$
$$N_I(\xi,\eta) = 1/2(1+\xi_I\xi)(1-\eta^2) \qquad \text{for} \quad I = 7,8,$$

where $(\xi_I, \eta_I = \pm 1)$. By referring to the three-dimensional solid element given in section (B.2), the nodal coordinates corresponding to the top ($\zeta = 1$) and bottom ($\zeta = -1$) surfaces may be denoted by $\mathbf{x}_I^{top}$ and $\mathbf{x}_I^{bot}$, respectively. Then, one may write the geometric representation for the shell element in terms of the mid-surface and coordinates $(\mathbf{x}_I^{top}, \mathbf{x}_I^{bot})$ as

$$\mathbf{x}(\xi,\eta,\zeta) = \sum_{I=1}^{n_{en}} \left\{ N_I(\xi,\eta)\frac{(1+\zeta)}{2}(\hat{\mathbf{x}})_I^{top} + N_I(\xi,\eta)\frac{(1-\zeta)}{2}(\hat{\mathbf{x}})_I^{bot} \right\}.$$

Alternatively, the above equation can be expressed in terms of the pseudo-normal base vector emanating from the I^{th} node which defines the fibre direction, $\boldsymbol{e}_3^{f(I)}$, as

$$\mathbf{x}(\xi,\eta,\zeta) = \sum_{I=1}^{n_{en}} \left\{ N_I(\xi,\eta) \left[(\hat{\mathbf{x}})_I^{mid} + \frac{\zeta}{2} a_I \boldsymbol{e}_3^{f(I)} \right] \right\}, \qquad \text{(B.15)}$$

where a_I is the shell thickness in the fibre direction. For the kinematic description of the shell, it is useful to introduce a nodal (fibre) coordinate system with an orthonormal basis defined with respect to the global coordinate system as

$$\boldsymbol{e}_3^{f(I)} = (\hat{\mathbf{x}}_I^{top} - \hat{\mathbf{x}}_I^{bot}) \,/\, \|\hat{\mathbf{x}}_I^{top} - \hat{\mathbf{x}}_I^{bot}\|_2 , \tag{B.16}$$

$$\boldsymbol{e}_1^{f(I)} = (\boldsymbol{e}_2 \times \boldsymbol{e}_3^{f(I)}), \qquad \text{and} \qquad \boldsymbol{e}_2^{f(I)} = (\boldsymbol{e}_3^{f(I)} \times \boldsymbol{e}_1^{f(I)}).$$

For the case when $\boldsymbol{e}_3^{f(I)}$ is parallel to $\boldsymbol{e}_2$ (ie. $\boldsymbol{e}_3^{f(I)} = \boldsymbol{e}_2$), the global base vector $\boldsymbol{e}_2$ is replaced with $\boldsymbol{e}_1$.

Kinematics

For each nodal coordinate, there are five degrees of freedom (DOF): three (global) translations (u, v, w) at the mid-surface and two (local) rotations (θ_1, θ_2) about the fibre base vectors $\boldsymbol{e}_1^{f(I)}$ and $\boldsymbol{e}_2^{f(I)}$, respectively. Therefore, the incremental displacement vector for this element can be written as

$$\underset{\sim}{\hat{\mathbf{u}}}^e = \{\hat{\mathbf{u}}_b^e\} = \left\{(\hat{u}, \hat{v}, \hat{w}, \hat{\theta}_1, \hat{\theta}_2)_1 | (\hat{u}, \hat{v}, \hat{w}, \hat{\theta}_1, \hat{\theta}_2)_2 | \ldots | (\hat{u}, \hat{v}, \hat{w}, \hat{\theta}_1, \hat{\theta}_2)_{n_{en}}\right\}^T , \tag{B.17}$$

where $n_{en} = 8$ is the number of nodes per element.

In addition, the total and incremental displacement field can be represented as the difference between (i) the original and current configurations $(t_o \rightarrow t)$, and (ii) the current and updated configurations $(t \rightarrow t + \Delta t)$, respectively, that is

$$\mathbf{u}_o = {}^t\mathbf{x} - {}^{t_o}\mathbf{X}, \qquad \text{and} \qquad \mathbf{u} = {}^{t+\Delta t}\mathbf{x} - {}^t\mathbf{x}.$$

Then, the respective displacement field for the element using equation (B.15) becomes

$$\mathbf{u}_o^t = \sum_{I=1}^{n_{en}} \left\{ N_I(\xi,\eta) \left[\hat{\mathbf{u}}_{o\,I} + \frac{\zeta}{2} \left({}^{t}a_I\, {}^{t}\mathbf{e}_3^{f(I)} - {}^{t_o}a_I\, {}^{t_o}\mathbf{e}_3^{f(I)} \right) \right] \right\}, \quad \text{(B.18)}$$

$$\mathbf{u}^t = \sum_{I=1}^{n_{en}} \left\{ N_I(\xi,\eta) \left[\hat{\mathbf{u}}_I + \frac{\zeta}{2} {}^{t}a_I \left({}^{t+\Delta t}\mathbf{e}_3^{f(I)} - {}^{t}\mathbf{e}_3^{f(I)} \right) \right] \right\}. \quad \text{(B.19)}$$

In equation (B.19) the thickness parameter, ${}^{t}a$, is held constant for the duration of the load step to avoid introducing any numerical instabilities. Hence, the corresponding nodal thickness updating is performed at the end of each load step [38] and is consistent with assumption (i) mentioned previously. Whereas, for equation (B.18) the *thinning* effect due to finite membrane strains is accounted for by considering the net change in shell thickness at each node.

For numerical implementation purposes, the terms in parenthesis in equations (B.15) and (B.19) involving the pseudo-normal vectors will eventually need to be expressed in terms of nodal rotations. Therefore, an appropriate director (rotation) vector updating scheme for finite rotations is examined.

B.3.3 Finite–rotations

As mentioned, finite rotational increments cannot simply be added vectorially. Hence, to account for finite rotations due to bending, it is convenient to consider the motion of the director (rotation) field as a vector $\mathbf{t}$ with one end point at the origin and the other point moving along the unit sphere S^2, such that

$$S^2 = \left\{ \mathbf{t} \in \Re^3 \mid \|\mathbf{t}\|_2 = 1 \right\}.$$

It is also useful to define the corresponding tangent space as

$$TS^2 = \left\{ \Delta \mathbf{t} \in \Re^3 \mid \mathbf{t} \cdot \Delta \mathbf{t} = 0 \right\} .$$

For a geometric description of the motion of the director field see Figure B.3. In general, the finite rigid body rotation of a first order tensor, t, about an axis is given by

$$\mathbf{t}' = \mathbf{Q}\mathbf{t},$$

where $\mathbf{Q}$ is a proper orthogonal (PO) second order tensor, such that

$$\mathrm{PO} = \left\{ \mathbf{Q} : \Re^3 \to \Re^3 \mid \mathbf{Q}^T = \mathbf{Q}^{-1} \text{ and } \det \mathbf{Q} = 1 \right\} .$$

The orthogonal transformation, $\mathbf{Q}$, may be represented as the exponential mapping [81], given by

$$\mathbf{Q} = exp[\hat{\boldsymbol{\Theta}}] = \sum_{n=0}^{\infty} (\hat{\boldsymbol{\Theta}})^n / n! ,$$

where the tangent space to PO, denoted by TPO, contains the set of skew symmetric tensors defined by

$$\mathrm{TPO} = \left\{ \hat{\boldsymbol{\Theta}} : \Re^3 \to \Re^3 \mid \hat{\boldsymbol{\Theta}} + \hat{\boldsymbol{\Theta}}^T = 0 \right\} ,$$

where $exp[\hat{\boldsymbol{\Theta}}]$: TPO $\to$ PO. Alternatively, the exponential map may be expressed as [81]

$$exp[\hat{\boldsymbol{\Theta}}] = \mathbf{I} + \frac{\sin \|\Delta \boldsymbol{\Theta}\|_2}{\|\Delta \boldsymbol{\Theta}\|_2} \hat{\boldsymbol{\Theta}} + \frac{1 - \cos \|\Delta \boldsymbol{\Theta}\|_2}{\|\Delta \boldsymbol{\Theta}\|_2^2} \hat{\boldsymbol{\Theta}}^2 , \tag{B.20}$$

and $\| \Delta \boldsymbol{\Theta} \|_2 = \sqrt{\theta_1^2 + \theta_2^2 + \theta_3^2}$ is the angle between $(\mathbf{t}, \mathbf{t}')$ with an axis of rotation parallel to $(\mathbf{t} \times \Delta \mathbf{t})$. In addition, the infinitesimal skew rotation

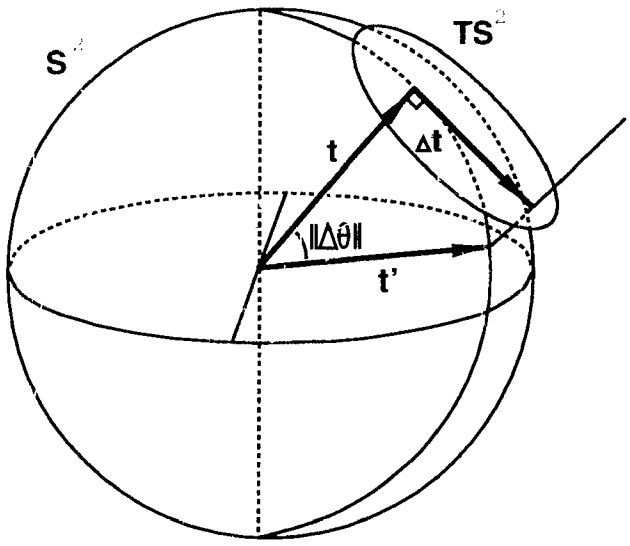

Figure B.3: A geometric description of the orthogonal transformation for finite rotations in 3-D space about an arbitrary axis parallel to $(\mathbf{t} \times \triangle\mathbf{t})$.

matrix has the form

$$\hat{\underset{\sim}{\Theta}} = \begin{bmatrix} 0 & -\theta_3 & \theta_2 \\ \theta_3 & 0 & -\theta_1 \\ -\theta_2 & \theta_1 & 0 \end{bmatrix}. \tag{B.21}$$

The importance of the above exponential map is that it enables the mapping of tangent vectors $\Delta\mathbf{t} \in TS^2$ onto points in S^2.

For the case when $\mathbf{t}$ corresponds to the pseudo-normal vector $\boldsymbol{e}_3^f$ of the nodal fibre triad, the (local) incremental rotational degrees of freedom are given by

$$\Delta \underset{\sim}{\theta} = [\theta_1, \theta_2, 0]^T.$$

Therefore, using the exponential mapping formula to update the nodal fibre triad $\boldsymbol{e}_i^{f(I)}$, $i \in \{1,2,3\}$ for the local DOF's of configuration n at the I^{th} node yields

$$\underbrace{\left\{\boldsymbol{e}_i^{f(I)}\right\}}_{3\times 1}^{n+1} = \begin{bmatrix} 1 - g_2\theta_2{}^2 & g_2\theta_1\theta_2 & g_1\theta_2 \\ g_2\theta_1\theta_2 & 1 - g_2\theta_1{}^2 & -g_1\theta_1 \\ -g_1\theta_2 & g_1\theta_1 & 1 - g_2(\theta_1{}^2 + \theta_2{}^2) \end{bmatrix} \left\{\boldsymbol{e}_i^{f(I)}\right\}^n, \tag{B.22}$$

where

$$g_1 = \frac{\sin\|\Delta\boldsymbol{\Theta}\|_2}{\|\Delta\boldsymbol{\Theta}\|_2}, \qquad g_2 = \frac{1 - \cos\|\Delta\boldsymbol{\Theta}\|_2}{\|\Delta\boldsymbol{\Theta}\|_2^2},$$

$$\|\Delta\boldsymbol{\Theta}\|_2 = \sqrt{\theta_1{}^2 + \theta_2{}^2}.$$

As $\|\Delta\boldsymbol{\Theta}\|_2$ tends to zero, the infinitesimal relationship yields $g_1 \to 1$ and $g_2 = 1/2$. Therefore, for *small* incremental angles (ie. $\|\Delta\boldsymbol{\Theta}\|_2 < 0.01$) the first and second order approximations for the orthogonal rotation matrix

become

$$\begin{aligned} \mathbf{Q} &= \mathbf{I} + \hat{\Theta} && 1^{st}\text{order}, \\ \mathbf{Q} &= \mathbf{I} + \hat{\Theta} + \frac{1}{2}\hat{\Theta}^2 && 2^{nd}\text{order}. \end{aligned}$$

B.3.4 Lamina Stress and Strain

Referring to the shell assumption (ii), which states that the normal stress is zero, $\sigma_3^l = 0$, it is convenient to express the stress/strain components in terms of the local lamina coordinate system as

$$\Delta \underset{\sim}{\sigma}^l = \underset{\sim}{\mathcal{L}}^l \Delta \underset{\sim}{\varepsilon}^l, \tag{B.23}$$

where the linear part of the lamina stress and strain vector are given as

$$\Delta \underset{\sim}{\sigma}^l = \begin{Bmatrix} \Delta\sigma_{11}^l \\ \Delta\sigma_{22}^l \\ \Delta\sigma_{12}^l \\ \Delta\sigma_{23}^l \\ \Delta\sigma_{31}^l \end{Bmatrix}, \quad \text{and} \quad \Delta \underset{\sim}{\varepsilon}^l = \begin{Bmatrix} \Delta\varepsilon_{11}^l \\ \Delta\varepsilon_{22}^l \\ 2\,\Delta\,\varepsilon_{12}^l \\ 2\,\Delta\,\varepsilon_{23}^l \\ 2\,\Delta\,\varepsilon_{31}^l \end{Bmatrix} = \begin{Bmatrix} u_{,x}^l \\ v_{,y}^l \\ u_{,y}^l + v_{,x}^l \\ v_{,w}^l + w_{,y}^l \\ u_{,w}^l + w_{,x}^l \end{Bmatrix}, \tag{B.24}$$

where (u^l, v^l, w^l) are the displacements in the local (x^l, y^l, z^l) directions, respectively. The above definition of the incremental strain neglects the calculation of the normal strain component $\Delta\varepsilon_{33}$. However, it can be recovered by utilizing the condition that $\sigma_3^l = 0$ as follows

$$\Delta\varepsilon_{33}^l = -\left(\sum_{i\neq j} \mathcal{L}_{33ij}^l \Delta\,\varepsilon_{ij}^l\right) \Big/ \mathcal{L}_{3333}^l. \tag{B.25}$$

The constitutive equation employed is expressed in terms of the local (lamina) coordinate system to enforce the zero normal stress hypothesis.

The local derivatives are obtained from the global derivatives of displacements (u, v, w) using

$$\begin{bmatrix} u^l_{,x} & v^l_{,x} & w^l_{,x} \\ u^l_{,y} & v^l_{,y} & w^l_{,y} \\ u^l_{,z} & v^l_{,z} & w^l_{,z} \end{bmatrix} = \underset{\sim}{\mathbf{T}}^{gl} \begin{bmatrix} u_{,x} & v_{,x} & w_{,x} \\ u_{,y} & v_{,y} & w_{,y} \\ u_{,z} & v_{,z} & w_{,z} \end{bmatrix} \underset{\sim}{\mathbf{T}}^{gl\,T}, \tag{B.26}$$

where $\underset{\sim}{\mathbf{T}}^{gl}$ is the transformation matrix defined in equation (B.11). The derivatives of the displacements with respect to the global coordinate system, are obtained in the same manner as the solid element using equation (B.5). To obtain the lamina quantities, the global to lamina orthogonal transformation, $\underset{\sim}{\mathbf{T}}^{gl}$, is utilized as follows

$$\sigma^l_{ij} = T^{gl}_{ik} T^{gl}_{jl} \sigma_{kl}, \tag{B.27}$$

$$\mathcal{L}^l_{ijkl} = T^{gl}_{im} T^{gl}_{jn} T^{gl}_{ko} T^{gl}_{lp} \mathcal{L}_{mnop}. \tag{B.28}$$

B.3.5 Finite Element Matrices

Strain-Displacement Matrices: $\underset{\sim}{\mathbf{B}}_L$ and $\underset{\sim}{\mathbf{B}}_{NL}$

A linearized displacement field used to calculate the stiffness matrices is given by

$$\mathbf{u}^e = \sum_{I=1}^{n_{en}} \left\{ N_I(\xi,\eta) \left[\hat{\mathbf{u}}_I + \frac{\zeta}{2} a_I \left(\hat{\theta}_2{}^I \mathbf{e}_1^{f(I)} - \hat{\theta}_1{}^I \mathbf{e}_2^{f(I)} \right) \right] \right\}, \tag{B.29}$$

where the pseudo-normal vector is approximated by

$${}^{t+\Delta t}\mathbf{e}_3^{f(I)} - {}^{t}\mathbf{e}_3^{f(I)} = \hat{\theta}_2{}^I \mathbf{e}_1^{f(I)} - \hat{\theta}_1{}^I \mathbf{e}_2^{f(I)}.$$

Proceeding with (B.29), the derivatives of the displacement field with respect to the local curvilinear coordinate system $(\xi\ \eta, \zeta)$ are

$$\begin{Bmatrix} u_{i,\xi} \\ u_{i,\eta} \\ u_{i,\zeta} \end{Bmatrix} = \sum_{I=1}^{n_{en}} \begin{bmatrix} N_{I,\xi} & -\frac{a_I}{2}\zeta N_{I,\xi} e_{2i}^{f(I)} & \frac{a_I}{2}\zeta N_{I,\xi} e_{1i}^{f(I)} \\ N_{I,\eta} & -\frac{a_I}{2}\zeta N_{I,\eta} e_{2i}^{f(I)} & \frac{a_I}{2}\zeta N_{I,\eta} e_{1i}^{f(I)} \\ 0 & -\frac{a_I}{2} N_I e_{2i}^{f(I)} & \frac{a_I}{2} N_I e_{1i}^{f(I)} \end{bmatrix} \begin{Bmatrix} \hat{u}_i^I \\ \hat{\theta}_1^I \\ \hat{\theta}_2^I \end{Bmatrix}, \tag{B.30}$$

where $e_{mi}^{f(I)}$ refers to the i^{th} component of fibre base vector m at node I, and $u_i \in \{u, v, w\}$. Ultimately, the derivatives of the displacement field are expressed in terms of the global coordinate system (x, y, z), and are obtained by pre-multiplying (B.30) by the inverse of the Jacobian matrix.

Adopting the elemental basis functions to approximate the (global) linear strain increment in terms of the nodal displacements yields

$$\begin{aligned} \Delta \underset{\sim}{\varepsilon} &= \sum_{I=1}^{n_{en}} \underset{\sim}{\mathbf{B}}_{L}^{I} \, \hat{\underset{\sim}{\mathbf{u}}}_{I}^{\iota} \\ &= \sum_{I=1}^{n_{en}} \left[\mathbf{b}_{T}^{I} \mid \mathbf{b}_{\Theta}^{I} \right]_{L} \begin{Bmatrix} \hat{\mathbf{u}}^{I} \\ \hat{\theta}_{1}^{I} \\ \hat{\vartheta}_{2}^{I} \end{Bmatrix} . \end{aligned} \tag{B.31}$$

The linear strain-displacement transformation matrix, $\underset{\sim}{\mathbf{B}}_{L} \in \Re^{6 \times n}$ with $n = n_{en} \cdot n_{dof}$, is partitioned into its translational and rotational contributions as follows:

Translational component

$$[\mathbf{b}_{T}^{I}]_{L} = \begin{bmatrix} b_{u,x}^{I} & 0 & 0 \\ 0 & b_{u,y}^{I} & 0 \\ 0 & 0 & b_{u,z}^{I} \\ b_{u,y}^{I} & b_{u,x}^{I} & 0 \\ 0 & b_{u,z}^{I} & b_{u,y}^{I} \\ b_{u,z}^{I} & 0 & b_{u,x}^{I} \end{bmatrix}_{I} ,$$

where

$$b_{u,x_i}^{I} = J_{i1}^{-1} N_{I,\xi} + J_{i2}^{-1} N_{I,\eta} \qquad \text{for} \quad x_i \in \{x, y, z\}.$$

Rotational component

$$[\mathbf{b}_{\Theta}^{I}]_L = \begin{bmatrix} -b_{\theta,x}^{I}e_{2x}^{f(I)} & b_{\theta,x}^{I}e_{1x}^{f(I)} \\ -b_{\theta,y}^{I}e_{2y}^{f(I)} & b_{\theta,y}^{I}e_{1y}^{f(I)} \\ -b_{\theta,z}^{I}e_{2z}^{f(I)} & b_{\theta,z}^{I}e_{1z}^{f(I)} \\ -(b_{\theta,x}^{I}e_{2y}^{f(I)} + b_{\theta,y}^{I}e_{2x}^{f(I)}) & (b_{\theta,x}^{I}e_{1y}^{f(I)} + b_{\theta,y}^{I}e_{1x}^{f(I)}) \\ -(b_{\theta,y}^{I}e_{2z}^{f(I)} + b_{\theta,z}^{I}e_{2y}^{f(I)}) & (b_{\theta,y}^{I}e_{1z}^{f(I)} + b_{\theta,z}^{I}e_{1y}^{f(I)}) \\ -(b_{\theta,z}^{I}e_{2x}^{f(I)} + b_{\theta,x}^{I}e_{2z}^{f(I)}) & (b_{\theta,z}^{I}e_{1x}^{f(I)} + b_{\theta,x}^{I}e_{1z}^{f(I)}) \end{bmatrix}_I$$

where

$$\mathbf{b}_{\theta,x_i}^{I} = \frac{{}^{t}a_I}{2}\left[\zeta(J_{i1}^{-1}N_{I,\xi} + J_{i2}^{-1}N_{I,\eta}) + J_{i3}^{-1}N_I\right] \qquad \text{for} \quad x_i \in \{x, y, z\}$$

For the shell element, the number of nodes per element, $n_{en} = 8$, and degrees of freedom per node, $n_{dof} = 5$, gives $n = 40$.

Next, consider non-linear strain-displacement transformation matrix for the shell element. Then, rewriting the derivatives of the displacement field given in (B.30) in terms of global coordinates yields

$$\begin{bmatrix} u_{,x} \\ v_{,x} \\ w_{,x} \\ \hline u_{,y} \\ v_{,y} \\ w_{,y} \\ \hline u_{,z} \\ v_{,z} \\ w_{,z} \end{bmatrix} = \sum_{I=1}^{n_{en}} \underbrace{\left[\begin{array}{ccc|cc} b_{u,x}^{I} & 0 & 0 & -b_{\theta,x}^{I}e_{2x}^{f(i)} & b_{\theta,x}^{I}e_{1x}^{f(i)} \\ 0 & b_{u,x}^{I} & 0 & -b_{\theta,x}^{I}e_{2y}^{f(i)} & b_{\theta,x}^{I}e_{1y}^{f(i)} \\ 0 & 0 & b_{u,x}^{I} & -b_{\theta,x}^{I}e_{2z}^{f(i)} & b_{\theta,x}^{I}e_{1z}^{f(i)} \\ b_{u,y}^{I} & 0 & 0 & -b_{\theta,y}^{I}e_{2x}^{f(i)} & b_{\theta,y}^{I}e_{1x}^{f(i)} \\ 0 & b_{u,y}^{I} & 0 & -b_{\theta,y}^{I}e_{2y}^{f(i)} & b_{\theta,y}^{I}e_{1y}^{f(i)} \\ 0 & 0 & b_{u,y}^{I} & -b_{\theta,y}^{I}e_{2z}^{f(i)} & b_{\theta,y}^{I}e_{1z}^{f(i)} \\ b_{u,z}^{I} & 0 & 0 & -b_{\theta,z}^{I}e_{2x}^{f(i)} & b_{\theta,z}^{I}e_{1x}^{f(i)} \\ 0 & b_{u,z}^{I} & 0 & -b_{\theta,z}^{I}e_{2y}^{f(i)} & b_{\theta,z}^{I}e_{1y}^{f(i)} \\ 0 & 0 & b_{u,z}^{I} & -b_{\theta,z}^{I}e_{2z}^{f(i)} & b_{\theta,z}^{I}e_{1z}^{f(i)} \end{array}\right]_I}_{\left[\mathbf{b}_T^I | \mathbf{b}_\Theta\right]_{NL}} \underbrace{\begin{Bmatrix} u_I \\ v_I \\ w_I \\ \theta_1^I \\ \theta_2^I \end{Bmatrix}}_{\{\hat{\mathbf{u}}_I'\}},$$

where $\underset{\sim}{\mathbf{B}}_{NL} \in \Re^{n\times n}$. Also, b_{u,x_i}^{I} and b_{θ,x_i}^{I} are as previously defined.

Material Stiffness Matrix: $\underset{\sim}{\mathbf{K}}'_l$

With $\underset{\sim}{\mathbf{B}}_L$ defined in section (B.3.5), the element material stiffness matrix of equation (3.10) becomes

$$\underset{\sim}{\mathbf{K}}'_l = \underbrace{[\mathbf{K}'_{ab}]}_{40\times 40} = \int_{\square_s}\int_{-1}^{1} \underset{\sim}{\mathbf{B}}_L^T [\underset{\sim}{\mathcal{L}}] \underset{\sim}{\mathbf{B}}_L \, J d\zeta d\square_s. \tag{B.32}$$

Geometric Stiffness Matrix: $\underset{\sim}{\mathbf{K}}'_{nl}$

The elemental geometric stiffness matrix of (3.10) expressed in terms of $\underset{\sim}{\mathbf{B}}_{NL}$ is given as follows

$$\underset{\sim}{\mathbf{K}}'_{nl} = \underbrace{[\mathbf{K}'_{ab}]}_{40\times 40} = \int_{\square_s}\int_{-1}^{1} \underset{\sim}{\mathbf{B}}_{NL}{}^T [\underset{\sim}{\boldsymbol{\sigma}}] \underset{\sim}{\mathbf{B}}_{NL} \, J d\zeta d\square_s. \tag{B.33}$$

Then, the stress matrix, $[\underset{\sim}{\boldsymbol{\sigma}}]$, in (3.10) has the form of a (9x9) matrix as

$$[\underset{\sim}{\boldsymbol{\sigma}}] = \begin{bmatrix} \sigma_{11}\underset{\sim}{\mathbf{I}} & \sigma_{12}\underset{\sim}{\mathbf{I}} & \sigma_{13}\underset{\sim}{\mathbf{I}} \\ & \sigma_{22}\underset{\sim}{\mathbf{I}} & \sigma_{23}\underset{\sim}{\mathbf{I}} \\ Sym. & & \sigma_{33}\underset{\sim}{\mathbf{I}} \end{bmatrix},$$

where $\underset{\sim}{\mathbf{I}}$ is the (3x3) identity matrix.

B.3.6 External Force Vector

Consider the external force vector to consist of the net contributions of the body and surface forces, then

$$\underset{\sim}{\mathbf{F}}'^{(ext)} = \underset{\sim}{\mathbf{f}}'_{body} + \underset{\sim}{\mathbf{f}}'_{surf} + \underset{\sim}{\mathbf{f}}'_{edge}. \tag{B.34}$$

Body force

The element body force vector for the continuum based shell element is given by

$$\underset{\sim}{\mathbf{f}}^{e}_{body} = \underbrace{\{\mathbf{f}^{e}_{a}\}^{body}}_{40\times 1} = \int_{\square_s}\int_{-1}^{1} \rho\, \underset{\sim}{\mathbf{N}}^{T}\underset{\sim}{\mathbf{b}}\, J d\zeta d\square_s , \tag{B.35}$$

where $\underset{\sim}{\mathbf{b}} = \{b_x, b_y, b_z\}^T$ are the components of the acceleration vector. In addition, $\underset{\sim}{\mathbf{N}}$ is a matrix of basis functions, in the form

$$\underset{\sim}{\mathbf{N}} = \left[\begin{array}{c|ccc|cc|c} & N_I & 0 & 0 & -\frac{a_I}{2}\zeta N_I \mathbf{e}_{2i}^{f(I)} & \frac{a_I}{2}\zeta N_I \mathbf{e}_{1i}^{f(I)} & \\ \cdots & 0 & N_I & 0 & -\frac{a_I}{2}\zeta N_I \mathbf{e}_{2i}^{f(I)} & \frac{a_I}{2}\zeta N_I \mathbf{e}_{1i}^{f(I)} & \cdots \\ & 0 & 0 & N_I & -\frac{a_I}{2}\zeta N_I \mathbf{e}_{2i}^{f(I)} & \frac{a_I}{2}\zeta N_I \mathbf{e}_{1i}^{f(I)} & \end{array}\right]_I . \tag{B.36}$$

for $I = 1, 2, \ldots, n_{en}$, and b_{θ,x_i} as defined in section (B.3.5).

Surface Force

The element surface force vector for the continuum based shell element is given by

$$\underset{\sim}{\mathbf{f}}^{e}_{surf} = \underbrace{\{\mathbf{f}^{e}_{a}\}^{surf}}_{40\times 1} = \int_{\square_s} \underset{\sim}{\mathbf{N}}^{T}\underset{\sim}{\mathbf{h}}_s\, J_s\, d\square_s , \tag{B.37}$$

where J_s is the determinant of the surface Jacobian matrix and $\underset{\sim}{\mathbf{h}}_s$ is the surface load vector (per unit area in the current reference configuration). Also, $\underset{\sim}{\mathbf{N}}$ is the matrix of basis functions as defined above. The subscript s refers to the face for which the applied load corresponds (ie., $\zeta = \{-1, +1\}$). The determinant of the surface Jacobian matrix, J_s, is given by

$$J_s = \|\mathbf{x}_{,\xi} \times \mathbf{x}_{,\eta}\|_2 \qquad \text{for} \qquad \zeta = \pm 1 ,$$

where $\|\cdot\|_2$ denotes the Euclidean norm.

Surface Pressure

For the case when a surface is subjected to a pressure load, the surface load vector, $\underset{\sim}{\mathbf{h}}_s$, becomes

$$\underset{\sim}{\mathbf{h}}_s \;=\; -\,p\,\underset{\sim}{\mathbf{n}},$$

where p is the external pressure exerted on the face $\zeta = \pm 1$. Further, the corresponding outward unit normal, $\underset{\sim}{\mathbf{n}}$, is given by

$$\mathbf{n} \;=\; \pm(\boldsymbol{e}_\xi \times \boldsymbol{e}_\eta) \;/\; \|\boldsymbol{e}_\xi \times \boldsymbol{e}_\eta\|_2 \qquad \text{for} \quad \zeta = \pm 1,$$

where (ξ, η, ζ) denotes the orthogonal unit bases of the curvilinear system.

Edge Force

The element edge force vector for the shell element is given by

$$\underset{\sim}{\mathbf{f}}^e_{edge} \;=\; \underbrace{\{\mathbf{f}^e_a\}^{edge}}_{40\times 1} \;=\; \int_{\square_e} \underset{\sim}{\mathbf{N}}^T \underset{\sim}{\mathbf{h}}_e \; J_e \; d\square_e, \tag{B.38}$$

where J_e is the determinant of the edge Jacobian matrix and $\underset{\sim}{\mathbf{h}}_e$ is the edge load vector (per unit area in the current reference configuration). Also, $\underset{\sim}{\mathbf{N}}$ is the matrix of basis functions as defined previously. The subscript e refers to the edge of the bi-unit square for which the applied load corresponds (ie., $\xi = \{-1, +1\}$ or $\eta = \{-1, +1\}$). The determinant of the edge Jacobian matrix, J_e, is given by

$$J_e \;=\; \begin{cases} \|\mathbf{x}_{,\eta} \times \mathbf{x}_{,\zeta}\|_2 & \text{if} \quad \xi = \pm 1 \\ \|\mathbf{x}_{,\xi} \times \mathbf{x}_{,\zeta}\|_2 & \text{if} \quad \eta = \pm 1 \end{cases},$$

where $\|\cdot\|_2$ denotes the Euclidean norm.